

Design and Application of a Fluidic Actuator System for High-lift Flow Control

vorgelegt von
Dipl.-Ing.
Matthias Bauer
geb. in Mühldorf am Inn

von der Fakultät V - Verkehrs- und Maschinensysteme
der Technischen Universität Berlin
zur Erlangung des akademischen Grades
- Dr. Ing.-

genehmigte Dissertation

Promotionsausschuss:

Vorsitzender: Prof. Dr.-Ing. D. Peitsch

Gutachter: Prof. Dr.-Ing. W. Nitsche

Gutachter: Dr.-Ing. H. Bieler

Tag der wissenschaftlichen Aussprache: 5. Juni 2015

Berlin 2015

Table of Contents

1	Introduction	1
1.1	Identifying the Research Gap	1
1.2	State of the Art: Flow Control for Separation Control	3
1.3	State of the Art: Flow Control Actuators	11
1.4	Physics of Fluidic Actuators	18
1.5	Contribution to the State of the Art	21
2	Published and Submitted Papers	25
2.1	Bauer2014a	26
2.2	Bauer2014b	34
2.3	Bauer2015a	45
3	Methodology and discussion of results	59
3.1	Summary of methodology	59
3.2	Summary of results	67
3.3	Discussion of results	68
	List of Figures	79
	List of Tables	80
	Bibliography	81

1 Introduction

Within the introductory chapter of this dissertation the journal papers, published or submitted for publication, are embedded in the broader context of concurrent research. Along the lines of recent developments in aircraft design, the need for research on the topic at hand is illustrated in sec. 1.1. This is followed by a detailed review of the state of the art of two fields of studies, flow control for separation control in sec. 1.2 and actuators for flow control in sec. 1.3, as this contribution is located at the intersection of those fields. The underlying flow-physical principles of the employed flow control actuator concept are delineated in sec. 1.4, before the contribution of the individual papers presented in chapter 2 to closing the research gap is laid out in sec. 1.5.

1.1 Identifying the Research Gap

Wings of modern civil airliners are designed for two distinct and very different flight phases. One of them is *cruise*, during which the aircraft travels at high altitude and high subsonic speed. As an aircraft spends the majority of each mission in this phase, this is what its aerodynamics are optimized for. This implies the attempt to minimize cruise drag and to maximize fuel efficiency by employing, among many other design features, supercritical airfoils, high-bypass ratio engines, and elaborate wing tip devices. Engineering solutions are necessary to ensure sufficient performance during the second relevant mission phase, namely low speed flight during *take-off* and *landing*. One solution commonly implemented on aircrafts is the use of mechanical high-lift devices (e.g. slats and flaps), which extend the flight envelope to the low-speed portion of the mission. During cruise, those devices are retracted to the main wing and the elements combined form a low-drag airfoil. In low-speed flight phases they are deployed to different take-off and landing setting, modifying the wing's geometry and consequently its aerodynamic performance. They allow higher angles of attack, and thereby higher lift coefficients, before the onset of separation. The underlying

physics of high-lift devices is thoroughly understood [1] and although undesirable weight and complexity is added to the overall system, they are to date without alternative. While, for decades, mechanical devices resolved the dilemma of having to cover efficiently for high- and low-speed flight, recent developments in aircraft design have turned up new problems that might require a different solution. Those developments, driven by spiking energy prices and fierce competition, aim at increasing the aircraft's fuel efficiency to reduce direct operating costs. In particular, two novel design features conflict with the local integration of mechanical high-lift devices at the wing's leading edge: ultra-high-bypass ratio fans (UHBR) and blended winglets. The large nacelles of UHBR engines need to be installed close to the wing to provide sufficient ground clearance without increasing the size of the aircraft's landing gear. In consequence, a slat would collide with the nacelle when deployed, resulting in the need of a *slat cut-out*, the fraction of the wing's span above the engine where no slat is installed. On the outer wing section, it's the wing tip device's slender shape and high local curvature that inhibits the installation of a mechanical leading edge device. This leaves regions of the wing unprotected by a slat and prone to separation (see fig. 1.1) at incidence angles much lower than for the remaining sections of the wing. It is in those regions where Active Flow Control (AFC) might be introduced to

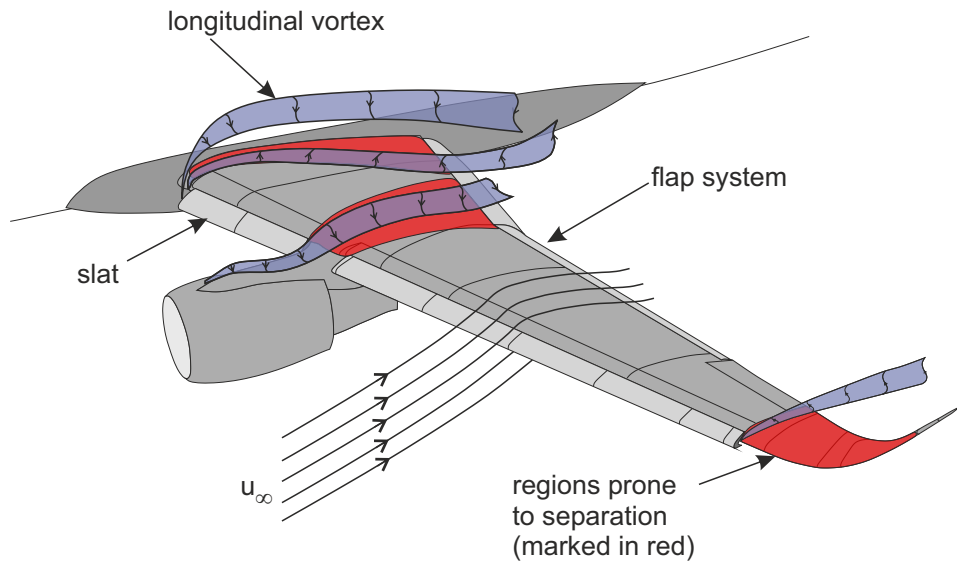


Figure 1.1: Regions prone to separation due to the lack of a leading edge device on the suction side surface of a wing according to [2, 3].

delay local separation to higher angles of attack and therefore to augment the overall high-lift system. To date, no civil airliner is equipped with an active flow control system. To mature this technology to a point where it is seriously considered in civil aviation, two aspects must be addressed beforehand. One is the development of capable and robust flow control actuators, which provide sufficient control authority to be effective and which are sufficiently reliable to be certified for the use in aircrafts. The other aspect is the furthering of understanding of the physical mechanisms of flow control and its transfer to relevant

scales, geometries, and flow conditions.

The present dissertation attempts to contribute to both of these aspects: By introducing a robust novel two-stage fluidic actuator system, which functions without incorporating any moving and electrical components and by applying this technology to a relevant wing geometry at realistic take-off Mach number.

1.2 State of the Art: Flow Control for Separation Control

Any viscous fluid that faces an adverse pressure gradient is prone to separation [4] and for any given flow condition, there is a theoretical limit to re-compression over a specific distance [5]. Separation of flow is usually undesirable. In particular for an aircraft wing the onset of large scale separation (stall) marks the limits of its functionality. The topology of the flow around an aerodynamic body, including the occurrence of separation, is generally prescribed by boundary conditions such as geometry, MACH number, and REYNOLDS number. The aim of flow control is, generally speaking, to modify this original state of flow in such a manner that beneficial effects are achieved [6]. While there are many different specific aims of flow control this contribution focuses on the delay of flow separation from a wing. The understanding of the possibility to modify flow by influencing the boundary layer dates back to the early work of Prandtl [7]. Since then, flow control technology was systematically researched, leading to a deeper understanding of the parameters determining its effectiveness and efficiency. In the following section a classification of flow control approaches is given and the underlying physical mechanisms are described. In addition, the influence of relevant parameters governing the effect of active flow control is reviewed and a summary of results for active flow control applied to the leading edge of model wings is given.

Classification and Mechanisms of Flow Control

The most fundamental differentiation of flow control technologies is between *active* and *passive* methods [8]. The later, e.g. vortex generators, function without addition of external energy to the flow. Their effectiveness depends solely on their capability to redistribute the energy and momentum content associated with the flow in a favorable manner. In contrast, active methods require energy from an external source to either introduce high-momentum fluid into the flow field or to remove low-momentum fluid from it. Active methods are subdivided further based on whether net mass flux is associated with the influx of energy and momentum, and whether this addition occurs continuously or periodically. Dependent on the type of control, different physical mechanisms are addressed to produce the desired effect. However, for separation control, all methods aim at consequently increasing the momentum content of the boundary layer flow, as this allows it to propagate against stronger adverse pressure gradients than possible naturally. Removing low-momentum fluid by boundary-layer-suction creates

a sink on the aerodynamic body, which accelerates the flow up to the location of suction and results in the start of a fresh and consequently more stable boundary layer downstream of it [9]. Both effects are favorable to delay separation. Continuous blowing, most commonly directed tangential to the local surface curvature, directly injects high-momentum fluid into the boundary layer. In addition, the fast air jet entrains high-momentum fluid from outside the boundary layer and increases the mixing rate of wall-near and wall-distant fluid, resulting in the re-energizing of the boundary layer [10]. If continuous, tangential blowing is combined with a Coanda surface, e.g. a suitably designed circular trailing edge, the virtual chord length and chamber of an airfoil are increased and significant lift gain can be achieved [11, 12]. In contrast to steady blowing, where the momentum content and the entrainment rate of the air jets are the driving factors for flow control effectiveness, unsteady (usually periodic) forcing produces vortical structures associated with the head vortex of the starting jet. Those vortices increase the mixing rate across the flow field and therefore enhance the momentum transfer between regions of low- and high-momentum fluid. Periodic forcing methods require a more complex actuator system than their continuous counterpart, as some mechanism must be included to provide unsteady flow. However, these unsteady methods are the means of choice in a multitude of experiments, as they promise a more efficient use of the actuation energy invested as shown e.g. in [13]. This paper reports the results of a study conducted by NASA and Tel Aviv University on the comparison of steady and unsteady actuation, which show that for reaching the identical aerodynamic benefit unsteady forcing is more efficient by two orders of magnitude. Dependent on the time scale and the amplitude of forcing different effects in the flow are found. Low amplitude actuation with a frequency higher than the natural frequencies of the flow increases primarily the turbulent kinetic energy content of the boundary layer by introducing small scale vortical structures [14]. In the presence of an already separated flow it is possible to tune the forcing frequency to the instabilities occurring naturally in the shear layer. In this case, the perturbations of medium amplitude introduced by the AFC system are amplified and the control attempt profits from a leverage effect, which significantly increases the mixing rate across the shear layer [15, 16]. In cases of high forcing amplitudes large scale vortices are induced reaching well beyond the outer limit of the boundary layer. During their downstream propagation, those vortices continuously transport high-momentum fluid from outside the boundary layer to the near-wall region. With this mechanism, the specific time-scale of the forcing is only of minor relevance for control effectiveness, but the repetition frequency must be sufficiently high to avoid separation from the body between two consecutive pulses [17]. This last mentioned mechanism is also the one on which the work presented here is based upon.

Some Parameters of Active Flow Control

Along the lines of the publications cited below relevant parameters for aircraft related active separation control attempts will be discussed. It is, however, difficult to compare results across experiments, as the effectiveness and efficiency of the

respective flow control attempt depends largely on the specific boundary conditions of the individual experiment. The model geometries range from generic 2D single element airfoils to swept and tapered multi-element 3D wings with different conventional high-lift devices installed. Flow conditions are commonly varied in terms of the similarity parameters MACH number and REYNOLDS number. The flow control system itself introduces an additional set of parameters, comprising geometrical (e.g. outlet shape, dimensions, and orientation) and physical (e.g. amplitude and frequency of forcing) aspects of the actuators. The most common locations of application are either the leading edge (see table 1.1 for references) or the trailing edge flap, reported e.g. in [18, 19, 20]. The aims are increase of maximum angle of attack, increase of lift, and reduction of drag. The three most prominent parameters of active flow control, actuation amplitude, air jet velocity, and actuation frequency, are generally presented in normalized form: Amplitude of forcing is given as momentum coefficient c_μ . The definition of this quantity is given in generalized form in equation 1.1.

$$c_\mu = \frac{J}{q_\infty \cdot A_{ref}} \quad (1.1)$$

The momentum coefficient c_μ relates the momentum flux introduced by the flow control system (J) to the momentum flux of the oncoming flow expressed by the product of the free stream dynamic pressure (q_∞) and a reference area, e.g. the projected area of the model A_{ref} . Velocity magnitude of the air jets emitted from the AFC system is presented as velocity ratio VR as defined e.g. in [21] and is given in equation 1.2

$$VR = \frac{u_{jet}}{u_{ref}} \quad (1.2)$$

This value denotes the ratio of the velocity of the air jet u_{jet} expelled through the AFC system and a reference velocity u_{ref} , which is either the local u_x or the incidence velocity u_∞ of the flow to be controlled. Finally, frequency of forcing is presented as a normalized frequency F^+ , which is defined analogous to a STROUHAL number as given by equation 1.3.

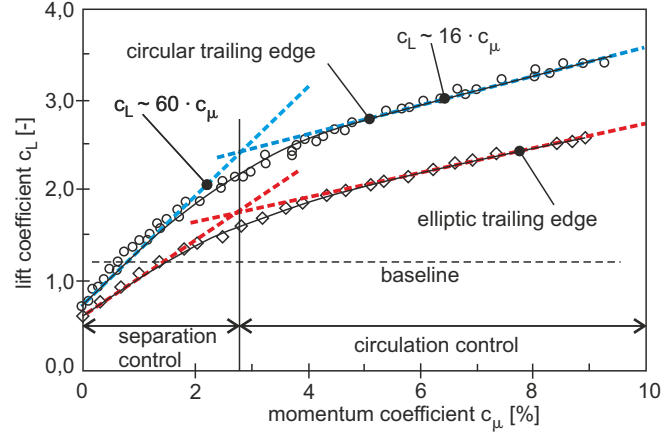
$$F^+ = St = \frac{f_{AFC} \cdot l_{ref}}{u_{ref}} \quad (1.3)$$

This dimensionless frequency modifies the physical time-scale of forcing, i.e. forcing frequency f_{AFC} , with a characteristic velocity u_{ref} (e.g. incidence velocity) and length scale l_{ref} (e.g. reference chord length).

Momentum Coefficient c_μ

Across studies the momentum coefficient c_μ was identified as the most significant parameter determining the effectiveness of active flow control, where increasing forcing amplitude yields increasing benefit. Actuation with low momentum coefficients is commonly labeled *boundary layer control*, while control with high momentum coefficients is referred to as *circulation control* [22]. While from a phenomenological point of view the threshold momentum coefficient separating

Figure 1.2: Influence of momentum coefficient on lift coefficient and transition from boundary layer control to circulation control according to Jones et al. [24]



those regimes is identified distinctly as the one that just suffices to suppress separation completely [23], the values reported from experiments range between $3\% < c_\mu < 5\%$ [22, 24, 25]. Transition between both regimes is gradual and goes in hand with decreasing actuation efficiency in terms of the ratio dC_L/dc_μ , as illustrated in fig. 1.2. It should be noted that although the momentum coefficient is commonly used to quantify the amplitude of forcing, it is not well suited to scale the benefit of flow control across different parameter settings let alone configurations [26].

Jet Velocity Ratio VR

The momentum coefficient c_μ contains the product of the mass flow rate and the velocity of mass propagation, constituting the jet's momentum flux J , in the numerator. This definition of c_μ implies that an infinite number of mass flow and jet velocity combinations can produce the identical momentum coefficient value. To account for the important differentiation between those two quantities the relevant parameter *jet velocity ratio* (VR) is used [21]. Results of flow control experiments on a 2D airfoil with a plain flap showed the superiority of using a high jet velocity ratio, compared to forcing the flow with the identical momentum coefficient, but higher mass-flow rate and lower jet velocity ratio [23]. To produce a positive effect on the flow the velocity ratio of the forcing must be larger than unity [22]. Otherwise, the momentum content of the boundary layer is reduced, which makes the flow more prone to separation, which yields a deteriorating effect on the aerodynamic performance [27, 28].

Dimensionless Frequency F^+

Depending on the physical flow control mechanism involved, different normalized frequency bands were identified as being optimal for maximal control effect. In studies employing acoustic excitation, implying low actuation amplitudes, dimensionless frequencies between $F^+ \approx 1$ [29] and $F^+ \approx 90$ [30] yielded aerodynamic benefit, however, a clear tendency towards higher F^+ -values is apparent (also cf. summary table in [22]). The reported frequency band is narrowed significantly to $F^+ = O(10^0)$ for cases where the control mechanism depends on resonance

of the perturbations introduced with instabilities inherent to the flow. Here, the bandwidth of most effective dimensionless frequency is identified between $F^+ \approx 1$ [31] and $F^+ \approx 1.3$ [32] as for those frequencies the perturbations have undergone maximum amplification by the time they arrive at the trailing edge of the model, therefore providing the highest mixing rate. The authors note that once the flow has reattached to the surface the most effective frequency range is shifted to higher values of $3 < F^+ < 4$ to prevent renewed separation. [32]. In experiments which omit a resonance effect on the flow a lower boundary for suitable frequencies is identified only. In those cases, where large scale perturbations directly transport high momentum fluid across the boundary layer, a lower bound of $F^+ \approx 0.5$ is reported to prevent the onset of separation between individual control pulses [33].

Model Geometry and Flow Parameters

The majority of flow control experiments were conducted for REYNOLDS number between $1 - 2 \cdot 10^6$ or lower. However, a small number of studies exist that extend the research to civil aviation relevant REYNOLDS number ranges. The beneficial effect of active flow control by means of periodic excitation was demonstrated successfully on a 2D airfoil with a plain flap for up to $Ma = 0,55$ and $Re = 40 \cdot 10^6$. The authors prove that for constant normalized frequency and momentum coefficient the effectiveness of flow control did not deteriorate when increasing the REYNOLDS number from $0.9 \cdot 10^6$ to $40 \cdot 10^6$ [34]. The invariance of aerodynamic benefit for a constant momentum coefficient was also shown in experiments on active flow control applied to the trailing edge flap of a two-element model in high-lift configuration for a REYNOLDS number range of $2 \cdot 10^6 < Re < 7 \cdot 10^6$ [20]. In a study on the identical configuration, the potential of AFC at high REYNOLDS numbers was confirmed for leading edge actuation [35], as the authors report even an increase in stall angle offset when increasing the REYNOLDS number from $Re = 4.2 \cdot 10^6$ to $Re = 9.2 \cdot 10^6$. Research on this two-element airfoil was extended from 2D to 2.5D in experiments comparing results for the unswept model with results for a 30° sweep angle. Those results indicate that although the lift coefficients are generally shifted to lower values for the swept configuration, the gain in lift coefficient is independent of model sweep [36]. The effect of model sweep is also subject of investigation in low REYNOLDS number experiments conducted on a single element airfoil at 0° and 30° sweep angle, in which the scaling factor for aerodynamic coefficients from 2D to 2.5D of $(1/\cos^2(\phi))$ is identified [37]. This scaling factor is confirmed at significantly higher MACH and REYNOLDS numbers ($Ma \approx 0.2$ and $Re \approx 20 \cdot 10^6$) in a study, in which the authors show that scaling (pressure) drag coefficient and momentum coefficient with that factor collapses the results of 2D and 2.5D measurements. The authors therefore conclude that the common scaling rules apply to active flow control applications also [38].

Additional geometric parameters influencing the effect of AFC are the location of actuation, the jet exit angle relative to the local surface tangent, and the flow cross section of outlet structure. Throughout different studies the flow control system is integrated upstream of the expected location of separation at a geo-

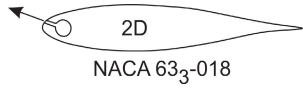
metrically prescribed exit angle between 0° (tangential) and 90° (surface normal) relative to the local surface curvature. It is noteworthy, that although those two parameters are deemed extremely important for the success of the control approach, no reasoning is usually given for the choice of AFC location and angle. The flow cross section of the outlets (characterized by e.g. hole diameter or slot width) is relevant, as for given ambient flow conditions and (AFC source) driving pressure, it prescribes the allocation of mass flow rate and jet velocity in the momentum coefficient. The choice of this geometric parameter therefore directly determines the jet velocity ratio for one respective momentum coefficient. Again, as for the other geometric AFC system parameters, this value is rather stated than substantiated throughout literature.

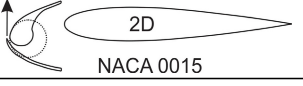
Results of Flow Control applied at the Leading Edge

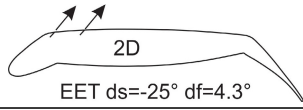
An summary of selected experiments dealing with active flow control applied to a model's leading edge is presented in table 1.1. The table summarizes the boundary conditions and results of experimental studies on separation control by means of steady or periodic actuation with or without mass injection. For each publication quoted, either the parameter combination producing the most significant gain or the one highlighted by the author was chosen to be included. Values marked '*' were not explicitly stated in the original source, but were calculated based on the provided context for the sake of completeness.

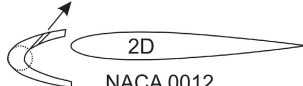
This overview table illustrates the wide range of boundary conditions found in experiments on the topic. The REYNOLDS numbers reach from $Re = 0.3 \cdot 10^6$ [39, 40] up to $Re = 9.2 \cdot 10^6$ [35], the MACH number range covers values from $Ma = 0.05$ [39] to $Ma = 0.2$ [41]. All authors report beneficial effects of the respective control approach, but the magnitude of gain varies significantly across the studies. Stall was offset between $\Delta\alpha_{max} = 1^\circ$ [42, 41] and $\Delta\alpha_{max} = 8^\circ$ [40], while gain in maximum lift between $\Delta C_{L,max} = 0.03$ [22] and $\Delta C_{L,max} = 0.92$ [40] was reported. The large variance in aerodynamic benefit is in parts attributed to the spread of momentum coefficients used, which ranges over three orders of magnitude from $c_\mu = 0.013\%$ [39] to $c_\mu = 3.2\% + < 2.7\% >$ [40], the latter using combined steady and oscillatory blowing. (Note, that the method of calculating the momentum coefficient is not consistent throughout the sources quoted.) With the exception of experiments on the DLR-F15 model, where the AFC system was integrated on the pressure side [43, 35], all authors report the location of AFC system between $0\% < x/c < 30\%$ on the suction side surface.

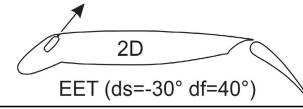
1.2 State of the Art: Flow Control for Separation Control

author (year)	model		type	location x/c [%]	angle [deg]	width [mm]	topology	
Chang [39] (1992)			ZNMF	1.25 (SS)	90	0.6	single slot	
Re [x 10 ⁶]	Ma [-]	u_∞ [m/s]	c_μ [%]	F⁺ [-]	DC [%]	Δc_{L,max} [-]	$\frac{\Delta c_{L,max}}{c_{L,max,base}}$ [%]	Δα_{max} [deg]
0.3	0.052*	15.5	0.013	4	n/a	0.16	17	5

author (year)	model		type	location x/c [%]	angle [deg]	width [mm]	topology	
Seifert [40] (1996)			PB + CB	0	0	1	single slot	
Re [x 10 ⁶]	Ma [-]	u_∞ [m/s]	c_μ [%]	F⁺ [-]	DC [%]	Δc_{L,max} [-]	$\frac{\Delta c_{L,max}}{c_{L,max,base}}$ [%]	Δα_{max} [deg]
0.3	0.064*	22*	0.8 + <0.8>	2	n/a	0.24	17	2
0.3	0.064*	22*	3.2 + <2.7>	2	n/a	0.92	64	8

author (year)	model		type	location x/c [%]	angle [deg]	width [mm]	topology	
Pack [42] (2002)			ZNMF	14 (SS) & 30 (SS)	30	0.88 & 0.5	2x single slots	
Re [x 10 ⁶]	Ma [-]	u_∞ [m/s]	c_μ [%]	F⁺ [-]	DC [%]	Δc_{L,max} [-]	$\frac{\Delta c_{L,max}}{c_{L,max,base}}$ [%]	Δα_{max} [deg]
0.75	0.08*	28*	2 x 0.03	10.5	Sinus	0.18	10	1

author (year)	model		type	location x/c [%]	angle [deg]	width [mm]	topology	
Greenblatt [44] (2003)			ZNMF	5 (SS)	45	0.6	single slot	
Re [x 10 ⁶]	Ma [-]	u_∞ [m/s]	c_μ [%]	F⁺ [-]	DC [%]	Δc_{L,max} [-]	$\frac{\Delta c_{L,max}}{c_{L,max,base}}$ [%]	Δα_{max} [deg]
0.24	0.052*	18*	0.09	1.5	n/a	0.03	3	2
0.24	0.052*	18*	1.8	1.5	n/a	0.25	25	5

author (year)	model		type	location x/c [%]	angle [deg]	width [mm]	topology	
Khodadoust [45] (2007)			ZNMF	14 (SS)	30	0.76	multiple slots	
Re [x 10 ⁶]	Ma [-]	u_∞ [m/s]	c_μ [%]	F⁺ [-]	DC [%]	Δc_{L,max} [-]	$\frac{\Delta c_{L,max}}{c_{L,max,base}}$ [%]	Δα_{max} [deg]
9	0.1	35*	0.4	3.4	n/a	0.13	4	3

1 Introduction

author (year)	model	type	location x/c [%]	angle [deg]	width [mm]	topology		
Scholz [43, 46] (2009)	 2D DLR-F15	PB	1 (PS)	$\alpha = 30^\circ$ & $\beta = 90^\circ$	1	multiple holes		
Re [$\times 10^6$]	Ma [-]	u_∞ [m/s]	c_μ [%]	F^+ [-]	DC [%]	$\Delta c_{L,max}$ [-]	$\frac{\Delta c_{L,max}}{c_{L,max,base}}$ [%]	$\Delta\alpha_{max}$ [deg]
2	0.14	46*	1.08	1.2	85	0.13	5	5
2.8	0.19*	65	0.48	0.8	50	0.18	7	3.5

author (year)	model	type	location x/c [%]	angle [deg]	width [mm]	topology		
Casper [35] (2011)	 2D DLR-F15	PB	1 (PS)	$\alpha = 30^\circ$ & $\beta = 90^\circ$	0.9	multiple holes		
Re [$\times 10^6$]	Ma [-]	u_∞ [m/s]	c_μ [%]	F^+ [-]	DC [%]	$\Delta c_{L,max}$ [-]	$\frac{\Delta c_{L,max}}{c_{L,max,base}}$ [%]	$\Delta\alpha_{max}$ [deg]
4.2	0.15	36.9*	0.53	1.62*	50	0.12	4	1.2
9.2	0.15	30*	0.53	2*	50	0.09	3	1.8

author (year)	model	type	location x/c [%]	angle [deg]	width [mm]	topology		
Brunet [41] (2013)	 2D GATEUR	CB, PB	8 (SS)	70	n/a	multiple slots		
Re [$\times 10^6$]	Ma [-]	u_∞ [m/s]	c_μ [%]	F^+ [-]	DC [%]	$\Delta c_{L,max}$ [-]	$\frac{\Delta c_{L,max}}{c_{L,max,base}}$ [%]	$\Delta\alpha_{max}$ [deg]
2	0.2	68*	3.5	-	100	0.26*	n/a	1
2	0.2	68*	1.8	1.1	50	0.31*	n/a	3

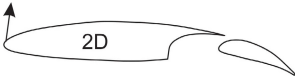
author (year)	model	type	location x/c [%]	angle [deg]	width [mm]	topology		
Brunet [41] (2013)	 2D	CB, PB	1 (SS)	60	0.25	multiple slots		
Re [$\times 10^6$]	Ma [-]	u_∞ [m/s]	c_μ [%]	F^+ [-]	DC [%]	$\Delta c_{L,max}$ [-]	$\frac{\Delta c_{L,max}}{c_{L,max,base}}$ [%]	$\Delta\alpha_{max}$ [deg]
2.5	0.175	60*	2.5	-	100	n/a	24	n/a
2.5	0.175	60*	1.2	0.7	50	n/a	13	n/a

Table 1.1: Overview of experimental results on active flow control applied to the leading edge. Abbreviations: ZNMF - zero net mass flux; PB - pulsed blowing; CB - continuous blowing; SS - suction side; PS - pressure side; DC - duty cycle; location - location of actuation; angle - geometric jet exit angle; width - slot width in chord-wise direction or hole diameter; subscript 'base' refers to the uncontrolled baseflow

1.3 State of the Art: Flow Control Actuators

The advantage of active flow control over passive approaches is that active methods can be adapted to the current flow state. Together with sensor systems, which provide real time information on the flow field, or at least the surface flow, AFC systems can be used in closed loop flow control and therefore allow a more specific modification of the respective aerodynamics. More basically, in contrast to passive methods such as e.g. vortex generators, which produce drag during the entire mission, active actuators can be turned off when they are not needed.¹ Active flow control, however, requires an actuator system that is capable of providing energy, momentum, and mass flow rates in the desired form and magnitude. This poses requirements on amplitude and frequency of the AFC system, parameters that directly influence the effectiveness of the control attempt. In addition, integration of those actuators must be feasible, imposing requirements on size and weight. Finally, when being considered for commercial applications, the actuators must be designed with robustness, energy conversion efficiency, costs, maintainability, and certifiability in mind.

Available Active Flow Control Actuators

A recent review of different actuator concepts for active flow control is given in [48]. As the results presented in this dissertation were obtained using an active actuator producing periodic air jets the overview of available actuator concepts is limited to types generating such perturbations. Those are namely:

- synthetic jet actuators
- plasma actuators
- mechanical valves employed as actuators
- pulsed combustion actuators
- fluidic actuators

In addition to the delineation of their functional principles a summary of advantages and disadvantages of each actuator type is given based on the literature referenced in this section and on personal experience with the various actuator concepts. This summary is provided here to later compare the newly developed two-stage fluidic actuator to the available concepts, which is done in table 3.5 in section 3.3.

Figure 1.3 shows illustrations of the different actuator types discussed in the following section, naming their major components.

¹Attempts were made to overcome this disadvantage by designing retractable vortex generators [47]. However, those devices did not find their way into industry practice so far.

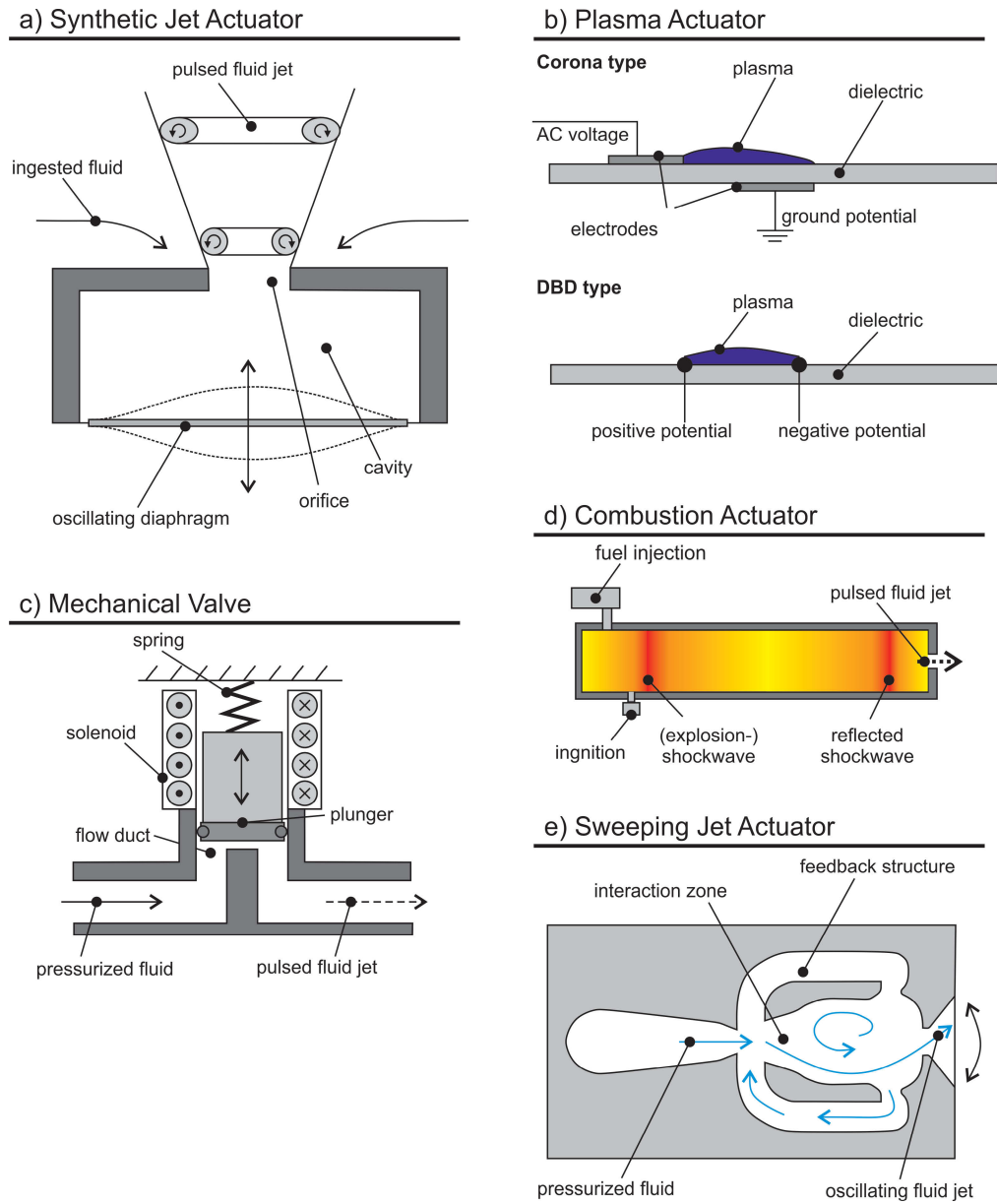


Figure 1.3: Schematics of a) Synthetic Jet Actuator [48], b) Plasma Actuator [48], c) Mechanical Valve, d) Pulsed Combustion Actuator [49], e) Sweeping Jet Actuator [50]

Synthetic Jet Actuators

Synthetic jet actuators (SJAs) are devices that inject momentum into the flow by alternately ingesting low momentum fluid from the boundary layer and expelling that fluid back into the flow as a fast jets. As they operate entirely on ambient fluid, the time-averaged net mass flux across the actuator is zero. SJAs consist of a cavity connected to the surrounding fluid via an orifice, with at least one of the encasing walls being an oscillating diaphragm. Most commonly, oscillation is induced by an electrically driven piston or a piezoelectric bender. Therefore, this type of actuator converts electric power into fluid power [51]. A wide range of studies are available, which aim at achieving optimal design, e.g. [52, 53]. SJAs rely on resonance effects, either of the cavity (HELMHOLTZ resonance) or of the oscillating diaphragm (mechanical resonance) to produce high jet amplitudes. This, however, limits the effective operation of SJA to a small frequency band. Various attempts were made to overcome this limitation. Exemplary solutions are to operate the device well below the resonance frequency and to increase the deflection of the diaphragm via a cantilever system [54], or to superimpose amplitude modulation on a device that is operated at the diaphragm's resonance frequency [55]. An extensive survey study on SJAs and their application for flow control is presented in [56].

Advantages

- distribution of electrical power necessary only facilitating low system weight and easy integration
- short response time facilitating closed-loop control

Disadvantages

- rather low momentum output with jet velocities commonly limited to low and moderate sub-sonic speeds
- high output amplitudes coupled to resonance frequencies
- incorporated moving parts diminish robustness
- low energy conversion efficiency $\eta_{SJA} \approx 10\%$ [51]
- significant heat is developed

Plasma Actuators

Another class of net mass flux neutral control devices are plasma actuators. Their basic design comprises a pair of electrodes, usually flush mounted on the aerodynamic body, where at least one electrode is in contact with the surrounding fluid. The electrodes are separated from each other either by an insulating (dielectric) material (*DBD plasma actuators*) or by the insulating fluid (*corona plasma actuator*) [48]. When a high voltage (several kV) is applied to the pair of electrodes, the fluid between them is ionized. The electric field exhibits a force on the cloud of ions, accelerating them, and inducing a mass flow tangential to the wall, which is referred to as *ionic wind*. By collision of ionized and neutral molecules, the electrical force is relayed to the electrically neutral fluid [57]. In a study aimed at increasing the performance of plasma actuators the authors identified the voltage applied to the electrode pair, the thickness of the dielectric material between the electrodes, the slope of the electrical driving signal, and the frequency of operation as the most important parameters determining the actuator performance [58]. A straight forward approach to increase the control authority of plasma actuators is the staggering of multiple devices [59].

Advantages

- distribution of electrical power necessary only facilitating low system weight and easy integration
- short response time facilitating closed-loop control
- incorporate no moving parts

Disadvantages

- very low momentum output
- resulting jet velocity is limited by slew rate of the power amplifier [58]
- high voltage at high frequencies are required, which might cause electromagnetic interference, thus hindering system integration
- scalability limited to staggering multiple actuators
- very low energy conversion efficiency $\eta_{SJA} < 1\%$ [60]

Mechanical Valves as Actuators

One of the more obvious solutions to producing pulsed fluid flows is the use of mechanical valves. Those devices operate by opening and closing a flow channel with a plunger, therefore either allowing or prohibiting flow through them. To function as flow control actuators, they require a reservoir of pressurized fluid at their inlet and a distribution structure connected to orifices in the aerodynamic body at their outlet [61]. The flow direction is unidirectional from the reservoir to the outlets, therefore the net mass flux through those actuators is positive. This makes them members of the class of mass injection type actuators. From the variety of different available valve types, fast acting solenoid valves and rotary valves are most commonly considered for flow control applications, as they provide the possibility to generate periodic jets with a frequency of up to 1kHz. As mechanical valves are off-the-shelf components, there are only few publications reporting explicitly on their design. Exceptions are cases where high frequencies (800Hz .. 2400Hz) are realized using rotary valves [62, 63], and valves with very small outlets ($O(100\mu m)$) producing *pulsed microjets*, high-momentum jets with low mass flow rates [64, 65].

Advantages

- high jet velocities possible
- short response time facilitating closed-loop control
- amplitude and frequency are decoupled
- additional parameters, e.g. *duty cycle*, can be controlled

Disadvantages

- supply of pressurized fluid *and* electrical power necessary
- required piping increases system weight
- unsteady valve operation reduces energy conversion efficiency
- large mass flow rates require many large solenoids, thus increasing system weight
- incorporated moving parts diminish robustness

Pulsed Combustion Actuators

Another class of mass injection actuators are based on pulsed combustion. In those devices, a fuel/oxidant mixture (e.g. hydrogen and air [49]) is ignited inside a cavity with an orifice connecting it to the surrounding fluid. On ignition, a detonation causes a rapid pressure rise in the cavity and the combustion products together with the unburned air is ejected through the orifice as a high momentum jet. Through repetition, a pulsed jet is generated that can be used in a flow control applications. In early versions of this actuator the pulse frequency was limited to approximately 100Hz due to the time required for refueling the device and the reaction time of the fuel/oxidant mixture [66]. Improved designs, that exploit cavity resonance effects and which rely on auto-ignition by reflected pressure waves, allowed to increase the pulse repetition rate was subsequently increased to values of up to 1kHz [67, 68].

Advantages

- very high jet velocities
- compact design possible
- very high energy density

Disadvantages

- limited frequency range due to required refueling time
- combustible material required for operation
- addition of combustion process outside the engine
- expelled gas is extremely hot
- incorporated (for now) moving parts diminish robustness

Fluidic Actuators

Similar to mechanical valves, actuators based on fluidic technology are a type of mass injection devices which require a reservoir of pressurized supply fluid to operate. Their working principle relies on the concept of fluid amplification, which was first patented in 1964 [69] as a component of a fluid system performing functions analogous to electronic systems and components of that time. The technology resurfaced in the form of flow control actuators in recent years, as they can be designed to function without incorporating any moving or electrical components, thus impressing with simplicity and robustness. Within the device a primary jet (*power jet*) is switched between two stable states (e.g. two outlets in the aerodynamic body) by application of a much weaker (in terms of lower momentum and mass flow rate) *control jet*. Fluidic actuators are subcategorized based on whether switching occurs auto-induced or whether it is externally triggered. Externally forced switching allows direct control of the frequency of the resulting pulsed jets, which is desirable in some flow control applications. The driving signal can be supplied by mechanical valves [70, 71], plasma actuators mounted in the control ports [72], piezoelectric benders inside the actuator body [73], or variable geometry HELMHOLTZ resonators attached to the control ports [74]. The two most prominent designs for self-induced switching fluidic actuators are based on the *sonic oscillator* [75] and on the *resistance induced oscillator* [76]. In both designs the switching frequency is determined by the geometry of the feedback structure and the attachment walls [77]. A fluidic actuator that does not produce discrete pulsed jets but rather a continuous wobbling fluid flow is the *sweeping jet actuator* [78], which was applied in numerous recent flow control experiments [79, 80, 81]. Addition of an ejector nozzle to the fluidic actuators power jet inlet, a device was designed that is capable of providing continuous suction and pulsed blowing simultaneously [82].

Advantages

- high amplitudes possible (up to aircraft scale [83, 84])
- large frequency range
- incorporate no moving parts
- good scalability

Disadvantages

- supply of pressurized fluid necessary
- required piping increases system weight
- not well suited for closed loop control due to slow response time
- large feedback structure required for low frequencies
- amplitude and frequency coupled directly for practical designs

1.4 Physics of Fluidic Actuators

The publications constituting the main part of this dissertation presented in chapter 2 describe results obtained using fluidic actuators. Thus, concluding the report on the state of the art on flow control actuator technology, some light is shed on the underlying physics of fluidic actuators based on the research of Warren [85] and Kirshner et al. [86].

Within a fluid amplifier (or more specifically: the *bistable switch*), the core element of any fluidic actuator, a fast fluid jet enters through a nozzle into a flow chamber that is enclosed by boundary walls to both sides of the jet as illustrated in fig. 1.4. At its borders, the jet entrains surrounding fluid due to molecular viscosity and turbulent mixing. This entrainment results in a decrease of static pressure between jet and boundary walls. As the flow chamber is open in main flow direction, the fluid entrained by the jet is replenished from ambient fluid. In a symmetric design the pressure to all sides of the jet is equal and the jet is in an equilibrium state, moving along the center axis of the device.

However, if the jet is just marginally closer to one wall than to the other, either by design, by manufacturing imperfections, or just by turbulent fluctuations, a pressure difference forms across the jet that will cause it to attach to the nearer boundary wall. This self-reinforced action stems from the fact that the smaller area between jet and the nearer wall reduces the counterflow on that side, which leads to a further decrease of static pressure between stream and wall. On the opposite side, the increased area between wall and jet facilitates the replacement of entrained material from the ambient fluid so that the static pressure on that side of the stream approaches ambient pressure. Thus, the resulting pressure difference increases in strength with the jet moving closer to one wall until attachment is complete. Once the jet is attached, an equilibrium of pressure forces is reached and the jet will stay attached to that wall. A recirculation bubble is

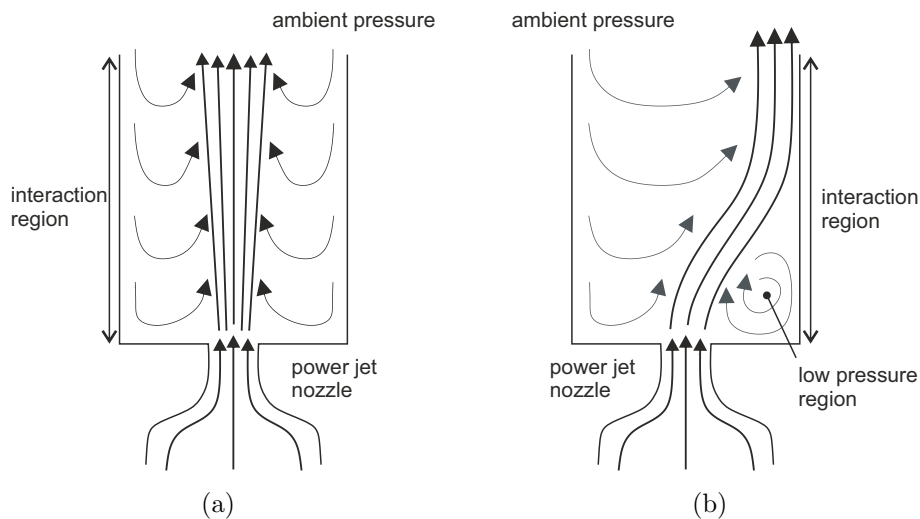


Figure 1.4: Jet between two parallel walls according to [85]: a) initial state; b) attached state

formed, which is sealed off from the ambient fluid by the attachment wall and the jet. At the location where the jet attaches, the static pressure on the wall increases because of the dynamic head of the stream. In its equilibrium state, the mass flow entrained by the jet is balanced by the recirculating mass flow from the reattachment region, while the opposite side of the jet is in direct communication with the ambient fluid. A design in which two inlets oriented perpendicular to the main flow direction are added downstream of the power jet nozzle constitutes the most basic fluid amplifier element. The flow topology inside such an element is illustrated in 1.5

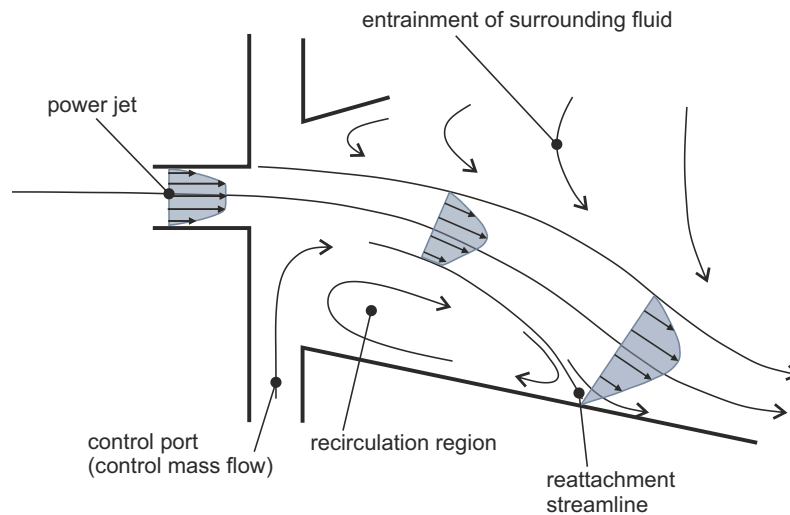


Figure 1.5: Flow topology inside a generic fluid amplifier element based on a sketch from [87]. (Asymmetric depiction to increase the readability)

To switch the jet to the other wall in this fluid amplifier a mass flow is supplied through the control port into the recirculation region. If this control mass flow rate supplied externally is larger than the rate of fluid that is entrained by the power jet, then the separation bubble expands and the reattachment line is shifted further downstream along the wall. Once the separation bubble has expanded beyond the limits of the attachment wall ambient fluid can enter into the recirculation region. This facilitates the pressure increasing effect of the control mass flow to the point of equalization of static pressure at both sides of the jet. In consequence, the jet experiences no force in lateral direction and streams (again) along the center axis of the device. Continuing addition of control fluid results in a pressure difference of opposite sign than before and the jet attaches to the other bounding wall due to the self-enforced mechanism described above. The mass flow rate required to induce switching must be larger only than the mass flow *entrained* by the power jet, which is much less than the total mass flow associated with it. This is the most fundamental (and eponymous) characteristic of fluid amplifiers. The ratio of the power jet mass flow rate and the control mass flow rate minimally required to induce switching is referred to as *gain*, which is one of the figure of merits of a fluid amplifier. Another figure of merit is the *pressure recovery*, which is defined as the ratio of total pressure

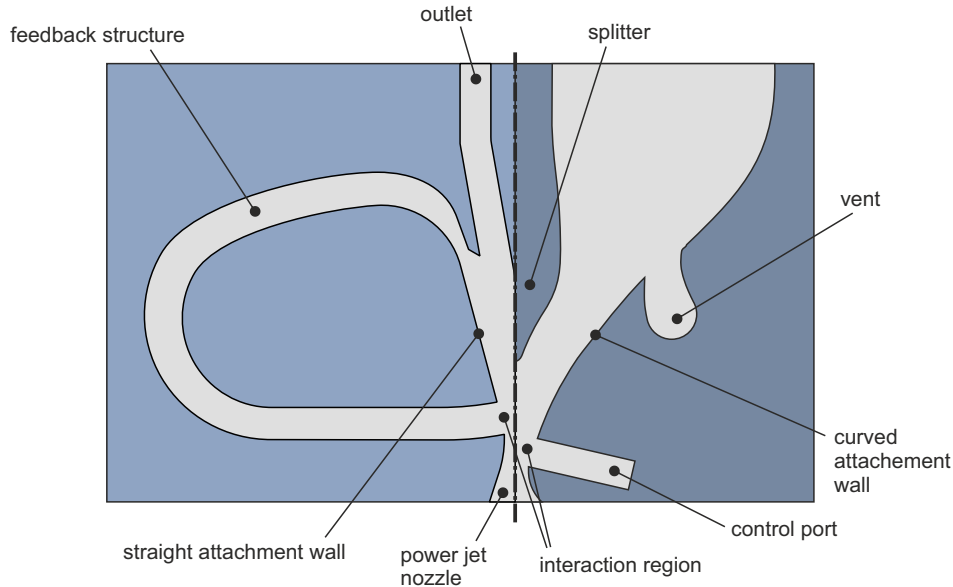


Figure 1.6: Nomenclature of fluid amplifiers: fluidic oscillator (left) and bistable switch (right); devices are cut at their symmetry planes

recovered at one outlet and the total pressure of the power jet. This figure essentially quantifies losses inside the device. An additional important characteristic parameter of fluid amplifiers is *stability*. This quantity describes the amount of loading that can be applied to the active outlet (i.e. how much the flow cross section can be contracted) before this loading would force the jet to switch to the other (unloaded) outlet without addition of control flow. Stability is foremost dependent on fluid amplifier geometry. It is high if the attachment walls are long, the splitter is rather far away from the power jet nozzle, and the opening angle of the attachment walls is small. Stability also increases if the pointed-wedge type splitter (as e.g. shown in fig. 1.6) is replaced by a flat or cusp-shaped splitter, because flow that impinges on such a splitter is forced to recirculate back upstream rather than directed to the other outlet. However, all measures that increase stability decrease gain, as a more stable amplifier requires higher control flow rates to switch the jet. Hence, for practical designs, a compromise must be found which satisfies requirements regarding gain and stability. Design features often found in fluid amplifiers are vents at various locations, e.g. at the splitter or at the attachment walls, which allow to dump superfluous material or which supply additional fluid if needed. Vents therefore increase stability and gain simultaneously. This is, however, impractical for fluidic actuators, as this would imply an air bleed inside the model or aircraft geometry. It is interesting to note, that most of the early fluid amplifier designs use straight attachment walls, although the authors of that time were aware of the advantages offered by curved walls. Curved walls allow a more compact design of the switching body, as the splitter can be moved closer to the power jet nozzle due to the fact that the size of the separation bubble can be reduced to the width of the control ports. However, different analytical descriptions for the characteristics of fluid amplifiers

were available for the straight-wall type only and the ease of theory based design was deemed of higher importance than compactness. This is understandable as the foremost use of fluid amplifier was in fluidic logic circuits, where a large number of those devices had to be designed and matched to each other.

Among the various sub-types of fluid amplifiers, the *fluidic oscillator* is of particular importance for their application as fluidic actuators, as it is this sub-type that allows to generate unsteady airflow without the need of moving parts. The switching mechanism and its dependency on geometry follows the flow-physical principles delineated above. Its special feature is, however, that fluidic oscillators synthesize the control flow required for switching from their own power jet. Different types of fluidic oscillators are reported in literature, the two most common ones in the context of application as flow control actuators [88] are the *sonic oscillator* [75] and the *resistance induced oscillator* [76] (the latter type is presented in fig. 1.6 on the left hand side). In the sonic oscillator the control ports are connected to each other. Switching is induced by pressure waves (caused by the different pressure levels in the control ports when the jet is attached to one side) that travel through the connecting flow channel [89]. The resistance induced oscillator bifurcates the power jet flow (usually) downstream of the splitter and feeds back a portion of the working fluid to the control port of the side where the jet is momentarily attached. This constitutes provision of a control flow (as described for the plain fluid amplifier above) and causes the jet to flip to the other attachment wall to repeat the process, thus causing self-induced oscillation.

1.5 Contribution to the State of the Art

The individual publications presented within this dissertation ([Bauer2014a], [Bauer2014b], [Bauer2015a], see chapter 2) delineate the path of research on the design and validation of a novel actuator system and its application to a highly three-dimensional outer wing model at realistic take-off MACH number. First, two streams of research are addressed individually, which are flow control actuator development and its validation on a generic geometry in [Bauer2014a] and the extension of separation control to an industry relevant geometry in [Bauer2014b]. Consecutively, those two streams are brought together in [Bauer2015a], which reports on flow control experiments conducted on an outer wing geometry representative for civil airliners at take-off MACH number using the devised actuator system.

In [Bauer2014a] the focus lies on the in-situ testing of a novel two-stage fluidic actuator system. The development of this flow control device contributes to the state of art by broadening the available range of AFC actuators presented in sec. 1.3. The actuator developed is a member of the family of fluidic actuators. It contributes to overcoming some limitations that are usually encountered with these types of actuators. State of the art fluidic actuators are single stage designs. This implies that frequency and amplitude of actuation are coupled when relying on self-induced oscillation or that mechanical components (e.g. driving valves) must be added to the system if independence of frequency and amplitude is desired.

The two-stage actuator reported allows to decouple these two fundamental AFC parameters within system inherent limits without requiring moving or electrical components. In addition, the publication constitutes the validation of the flow control concept, which is to suppress separation by means of pulsed air jet blowing from finite slots, on a generic configuration. To show feasibility, the actuator system was integrated at the leading edge of a 2D-two-element model in high-lift configuration. A model with identical geometry was already used as test bed for leading edge separation control experiments (DLR-F15 model in table 1.1, [35, 43, 46]). The control strategy here, however, is different than in previous studies. In [Bauer2014a] the flow control approach bases on pulsed blowing from slots integrated on the suction side surface of the main element, while previous studies employed vortex generator jets emanating from the pressure side of the main element. The results in [Bauer2014a] confirm the capability of flow control to effectively shift stall onset on this model to higher angles of attack with the two-stage fluidic actuators. Therefore, the contribution extends the available results on leading edge flow control experiments as reviewed in sec. 1.2. In addition, the experiments on this simplistic 2D configuration substantiated the assumption formulated in [27], proving that phase shift between neighboring actuator outlets, which is an immanent feature of the fluidic control system, does not render the AFC approach ineffective. The flow control concept is subsequently transferred to the realistic wing geometry researched in [Bauer2014b] and [Bauer2015a]. The focus of [Bauer2014b] is on advancing flow control for separation control to a more complex geometry rather than on actuator system development or testing. The experiments were conducted using a flow control system that incorporates fluidic components, but uses several mechanical valves as drivers. This approach lends more flexibility to the experimental setup and reduces design efforts. In [Bauer2014b] leading edge separation control (by means of pulsed blowing) was applied to the outer wing section of a model geometry representative for a modern civil airliner wing. Due to the highly complex geometry investigated, this contribution reaches beyond the current state of the art, which commonly reports on flow control applied to generic configurations (e.g. all studies summarized in table 1.1). It is in line with the few publications aiming at transferring flow control technology to aircraft relevant geometries. Exemplary studies for such research are the attempt to control separation on the trailing edge flap of a 3D-three-element wing in high-lift configuration [27], on a realistic vertical tail plane [79, 90, 80], and on the rudder of a V-22 *Osprey* model [81]. Within the scope of [Bauer2014b] it was shown, that the flow control strategy demonstrated in [Bauer2014a] can be transferred successfully to complex flows. Significant aerodynamic performance increase is demonstrated, resulting from the combined benefits of offsetted stall angle, increased maximum lift, and simultaneously decreased drag.

In the remaining publication [Bauer2015a], the findings of [Bauer2014a] and [Bauer2014b] are synthesized and applied in separation control experiments conducted at take-off Mach number of $Ma = 0.2$. Here, the model geometry is similar to the one already presented in [Bauer2014b], but the fidelity level is increased further, e.g. by addition of a deflected aileron. The experiments are

conducted in a large wind tunnel facility, guaranteeing the minimization of wind tunnel influences on the results and good transferability of the findings to civil aviation research. The two-stage actuator system discussed in [Bauer2014a] is employed in the experiments, further substantiating the relevance of this contribution for real life applications, as this AFC actuator system is a candidate technology for industry use [91]. Therefore, the publication is in line with recent attempts to prove the feasibility of flow control under conditions encountered in civil aviation, such as research in which separation control using fluidic actuators is applied successfully to a full-scale vertical tail plane to improve its the rudder effectiveness [83, 84]. The results in [Bauer2015a] demonstrate a significant offset in performance degradation to higher incidence angles on the model investigated at an energy and mass flow rate requirement readily available on modern civil airliners.

The individual publications and this dissertation as a whole therefore contribute to closing the gap between research aimed at enhancing the understanding of flow control aerodynamics and its application to industry relevant geometries and flow conditions.

2 Published and Submitted Papers

In this chapter the required papers are printed.

2.1 Bauer2014a

Bauer, M., Lohse, J., Haucke, F., and Nitsche, W.,
**High-Lift Performance Investigation of a Two-Element Configuration
with a Two-Stage Actuator System,**
AIAA Journal, Vol. 52, No. 6, 2014, pp. 1307-1313.

Technical Notes

High-Lift Performance Investigation of a Two-Element Configuration with a Two-Stage Actuator System

Matthias Bauer,* Jakob Lohse,† Frank Haucke,‡ and Wolfgang Nitsche§

Technical University of Berlin, 10623 Berlin, Germany

DOI: 10.2514/1.J052639

Nomenclature

A_{ref}	=	total projected area of wing and flap, m ²
c_L	=	lift coefficient
c_p	=	pressure coefficient
c_{ref}	=	reference chord length, m
c_μ	=	momentum coefficient, $(\dot{m} \cdot \bar{u}_{\text{jet,theo}})/(q_\infty \cdot A_{\text{ref}})$
F^+ , Sr	=	normalized frequency, Strouhal number, $(f \cdot c_{\text{char}})/u_{\text{char}}$
f	=	frequency, Hz
\dot{m}	=	total mass flow rate, kg/s
\dot{m}_d	=	driving stage mass flow rate, kg/s
\dot{m}_o	=	outlet stage mass flow rate, kg/s
p_{stat}	=	static pressure, bar
p_0	=	total pressure, bar
$R(d/o)$	=	ratio of mass flow rate through driving and outlet stage, \dot{m}_d/\dot{m}_o
u, v, w	=	velocity in $x, y,$ and z directions, m/s
$u_{\text{jet,theo}}$	=	velocity of air jet calculated from mass flow rate, m/s
u_∞	=	freestream velocity, m/s
$ V $	=	absolute velocity from $u, v,$ and w components, m/s
x	=	streamwise direction, mm
y	=	direction normal to tunnel floor, mm
z	=	(spanwise) direction normal to tunnel side wall, mm
α	=	angle of attack, deg
δ_f	=	incidence angle of flap, deg

I. Introduction

MECHANICAL high-lift devices such as slats and flaps are highly optimized aerodynamic design elements capable of increasing an aircraft's flight envelope. Their physics is well understood [1], and although they add weight and complexity to the overall system they are to date without alternative for providing high lift at low speed for commercial airliners. However, their integration

conflicts with developments in modern aircraft design. The diameter of jet engines has increased significantly over the past decades, as manufacturers realize higher bypass ratios in order to limit fuel consumption. To avoid the need for larger and heavier landing gear those engines are moved closer to the wing. This makes it necessary to increase the *slat cutout*, the section of the wing's leading edge where slats cannot be integrated, as they would collide with the nacelle when deployed. Slat integration also becomes problematic on the outer wing section, because its slender shape offers insufficient installation space. Active flow control (AFC) technology might amend the overall high-lift system to prevent pressure-induced flow separation where mechanical devices reach the limit of integrability.

The work presented here comprises wind-tunnel experiments on a two-element airfoil to which active separation control is applied near the leading edge. It therefore follows the path of the work of, e.g., [2–5], which research unsteady forcing as a tool to improve the performance of slatless high-lift configurations.

Different active flow control strategies have proven to be effective. In most current experiments unsteady forcing is employed, as this allows more efficient use of the invested energy compared with, e.g., steady blowing [6]. This finding leaves the question of how to generate unsteady perturbations in the flow unanswered. Different actuator types are considered. Among them are zero net mass flux actuators of different types [7,8], mechanical valves [9,10], and actuators based on the fluidic principle [11]. An overview of various actuator concepts is given, e.g., in [12].

To date, no civil aircraft uses AFC technology, although it has been flight tested in several instances [13–15]. That is supposedly because most flow control actuators are assumed to be not yet suitable for practical industrial application, as they lack efficiency, robustness, or control authority. For our experiments we employ a highly compact staged fluidic actuator system to generate the required pulsed air jets. Fluidic components have come to the focus of flow control research [16–18], as they are able to provide high-control authority without incorporating moving or electrical components. Our novel staged approach adds a degree of freedom to setting the actuation frequency while still allowing a compact design. In our work presented here, we use this staged fluidic actuator to generate pulsed air jets that emanate from slots on the wing's suction side to defer the onset of pressure-induced separation. The flow control system and experimental setup are described, and the effect of flow control on pressure distribution and velocity field is evaluated. We show that by applying AFC the maximum angle of attack before separation occurs is increased by up to 4 deg, which results in an increase of $c_{L,\text{max}}$ by $dc_L = 0.27$ at a momentum coefficient of $c_\mu = 3.27\%$.

II. Experimental Setup

This section describes the wind-tunnel model, including the fluidic actuator system, and specifies the experimental uncertainty.

A. Wind-Tunnel Model and Instrumentation

The experiments were carried out on a wind-tunnel model of the DLR-F15 high-lift airfoil in a two-element setup. This airfoil is a section of a three-element civil aircraft wing. For the results presented here the slat was retracted into the main element. Further investigation on this airfoil is presented, e.g., in [19]. The flap was deployed at $\delta_f = 45$ deg (with gap = 15.9 mm and overlap = 3.3 mm), which is an AFC reference configuration with separated flow from 20% of the flap's chord. The chord of the model in clean configuration is $c_{\text{ref}} = 600$ mm, and its span is 1660 mm. The airfoil is mounted between two circular end plates to prevent pressure equalization between the upper and lower surface. The model's angle

Received 22 March 2013; revision received 16 October 2013; accepted for publication 17 October 2013; published online 16 April 2014. Copyright © 2013 by the American Institute of Aeronautics and Astronautics, Inc. All rights reserved. Copies of this paper may be made for personal or internal use, on condition that the copier pay the \$10.00 per-copy fee to the Copyright Clearance Center, Inc., 222 Rosewood Drive, Danvers, MA 01923; include the code 1533-385X/14 and \$10.00 in correspondence with the CCC.

*Ph.D. Student, Department of Aeronautics and Astronautics; matthias.bauer@ilr.tu-berlin.de.

†Ph.D. Student, Department of Aeronautics and Astronautics; jakob.lohse@ilr.tu-berlin.de.

‡Ph.D. Student, Department of Aeronautics and Astronautics; frank.haucke@ilr.tu-berlin.de.

§Professor, Department of Aeronautics and Astronautics; wolfgang.nitsche@ilr.tu-berlin.de.

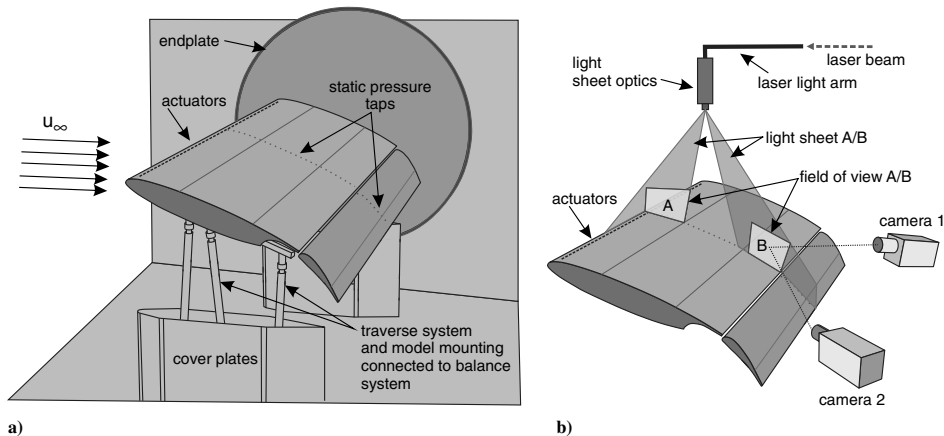


Fig. 1 Experimental setup: a) sketch of wing model in wind tunnel showing traverse system, actuator outlets, and static pressure taps and b) PIV setup with fields of view at leading (A) and trailing (B) edge of the main element.

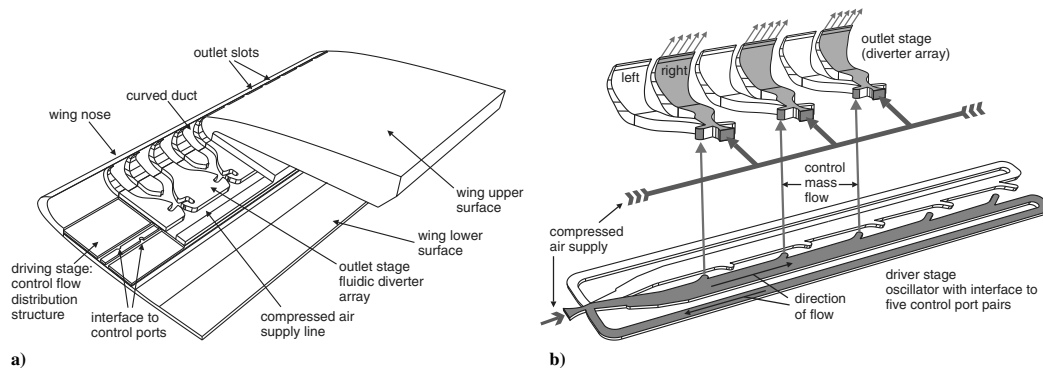


Fig. 2 Actuator system employed: a) integration in the model's leading edge and b) sketch of the two stages and their interconnection: the grayed area illustrates the internal flow for a given point in time when the "right" outlets of the diverter elements are active.

of attack is adjustable using a traverse system that is connected to the balance beneath the wind-tunnel floor. All experiments were conducted at a Reynolds number of $Re \approx 1 \times 10^6$. Tripping was applied to ensure a turbulent state of the boundary layer. Therefore, a 40- μm -high and 1-mm-wide tape was applied to the main element at $x/c = 0$ and 2% on the pressure side and $x/c = 1\%$ on the suction side. A schematic of the model setup is shown in Fig. 1a. Further experiments on this setup are presented in [10].

A six-component strain gauge balance allows for measuring the forces and moments acting on the model. Surface pressure is measured at the midspan of the model at 32 stations on the main element and at 16 stations on the flap. Stereoscopic time-resolved (TR) particle image velocimetry (PIV) measurements are performed at midspan for individual angles of attack and actuation parameter combinations at the main element's leading and trailing edges. A sketch of the PIV setup showing the two different fields of view is presented in Fig. 1b. A total of 1024 image pairs is recorded at a sampling rate of 1.5 kHz for each point of interest. The actuator system is designed so that the center of one jet outlet is located in the section where pressure and PIV data are measured. Here, the nature of the flow is considered to be two-dimensional. Three-dimensional effects resulting from the interaction of wing and end plates are not investigated within the scope of the results presented.

All experiments were conducted at the GroWiKa wind-tunnel facility at the Technical University of Berlin, which is a closed-circuit wind tunnel with a 1400×2000 mm test section.

B. Active Flow Control System

The actuator system integrated in the leading edge of the main element is of the fluidic type. Figure 2a shows its integration in the model wing.

Pulsed air jets exit through a total of 76 rectangular orifices (measuring 16 mm in the spanwise and 1 mm in the streamwise direction), which are located at 2.5% of the chord position on the suction side surface. Their spacing is fixed at 20 mm, leaving a gap of 4 mm between two adjacent outlets. The ejection angle of the jets is 30 deg relative to the model's surface. The active area therefore covers approximately 73% of the span from end plate to end plate. Unsteady perturbations of the flow are generated by an array of fluidic diverters, which are based on the principle of fluid amplification.¹ An alternating pressure source (driving signal) is applied to the diverters' control ports to push the fluid entering to either side and therefore to switch the outflow periodically between the respective outlets of one diverter. This generates a pulsed jet flow with a 180 deg phase shift between two neighboring orifices.

Two different drivers to induce the switching were employed in the course of the experiments. The first approach comprises the generation of a periodic pneumatic signal using fast-switching solenoid valves. Here, the frequency imposed on the fluidic diverters can be manipulated easily with an electrical signal generator. The

¹The first research on that concept is attributed to B. M. Horton, R. E. Bowles, and R. W. Warren, Harry Diamond Laboratories, March 1960.

main disadvantage of using valves is their lack of robustness as they incorporate moving components. This might be a hindrance with respect to future application in commercial aircrafts. Therefore, the second approach to generating the required pneumatic driving signal comprises the use of modified fluidic oscillators. Those fluidic elements are designed so that self-induced switching occurs between their two branches. This is done by feeding back a portion of the working fluid of one branch to flip the entering jet to the other branch. Each branch has several outlets providing the diverters with the required driving signal. In the experiments presented, one oscillator controls up to five outlet stage diverter elements. In this configuration the actuator system incorporates no moving or electrical components and requires only a pressure supply. A sketch of this system is provided in Fig. 2b. The challenge when designing a staged system is that the two stages have to be matched to each other. However, there are numerous reasons for employing the staged concept rather than only one stage of oscillators. The efficiency in terms of total pressure to dynamic pressure conversion increases, as several diverters are driven by only one oscillator that produces higher pressure losses due to its internal complexity. If low frequencies are desired, driving multiple diverters with one oscillator reduces the required installation space, as only the driving oscillator requires feedback lines (the length and volume of which strongly influence the resulting switching frequency). The use of a two-stage system allows setting (within system immanent limits) of actuation amplitude and actuation frequency independently when using two different pressure supplies for the diverter and driving stage.

The performance of the AFC system was evaluated in bench-top experiments. Different pressure levels, resulting in different rates of flow, were applied to the two stages independently. Each combination of two pressure levels constitutes one point of operation of the AFC system. The mass flow rates were recorded, and the resulting output signal (in terms of total pressure of the air jets) of the actuator was determined using Kulite pressure transducers. The range of operation of the actuator system is shown in Fig. 3. The frequency of the AFC system is determined by the total mass flow through the stages and its distribution between the driving and outlet stage $[R(d/o)]$. The modulation of the pulsed air jets [as defined by $\text{Mod} = (p_{0,\text{max}} - p_{0,\text{min}})/p_{0,\text{max}}$] is above 95% for all data points presented. Within the bounds of the curves shown, any combination of total mass flow rate and frequency can be set. Two exemplary signals of the recorded total pressure fluctuation at the diverters' outlets are provided to illustrate the quality of the perturbations produced. As the switching is induced by the mass flow that propagates through the driving stage, there is a phase lag between two neighboring diverters, which are controlled by one driver. Its magnitude is not constant and is determined by the velocity of the internal flow. When using the valve-driven system all diverter arrays

operate in-phase, as all valves are controlled by the identical electrical signal. This is not the case for the oscillator driven configuration. Here, the phase relation between the diverter arrays is undetermined, as no attempt was made to synchronize the individual oscillators. As it is known from previous experiments [20] that the pulsed jets influence mainly the region immediately trailing them, the phase relation of distant actuators is considered to be of little importance for the overall flow control performance.

All momentum coefficients quoted are calculated using $c_\mu = (\dot{m} \cdot \bar{u}_{\text{jet,theo}})/(q_\infty \cdot A_{\text{ref}})$, where $\bar{u}_{\text{jet,theo}}$ is the jet velocity (assuming a uniform block profile) calculated from the measured mass flow rate and the geometry of the actuator outlets.

C. Experimental Uncertainty

The experimental uncertainty in determining the lift force using the balance system is estimated to be within the range of $\pm 0.1\%$ of cited values. No wind-tunnel correction is applied, as only lift gain is considered. The force exerted by the air jets was measured directly for each momentum coefficient without oncoming flow to subsequently correct the recorded data for those values. The manufacturer specifies an accuracy of $\pm 0.5\%$ for the sensors used for measuring the pressure distribution on the main element and flap, which corresponds to an error of less than 25 Pa. The momentum coefficient is calculated from the mass flow rate through the outlet slots measured in situ during the experiments. The uncertainty in measuring the mass flow rate is $\pm 1\%$. This translates into a deviation from the quoted momentum coefficients of less than $\Delta c_\mu = 0.05\%$. The homogeneity of the spanwise jet velocity was verified in bench-top experiments. The peak velocity differs by less than 5%. An adaptive cross-correlation algorithm with interrogation window shifting and deforming is used to evaluate the particle images. The starting size of the interrogation windows is 128×128 square pixels, which is reduced after each processing step to a final size of 24×24 square pixels (corresponding to a spatial resolution in x and y of approximately 1.2 mm) with 50% overlap for each step. Global velocity and local median filters were used during each evaluation step. Filtered vectors are recalculated on a larger interrogation window, except for the last step, where filtered vectors are interpolated. The rate of outliers for each evaluation step is less than 4%.

III. Results

This section reports on results obtained during the experiments. First, global force measurements are considered and static pressure measurement data are presented to illustrate the effect of actuation amplitudes on the flow's ability to withstand large positive pressure gradients. Subsequently, TR-PIV data are analyzed to show the effect of actuation on the flowfield near the wing's surface.

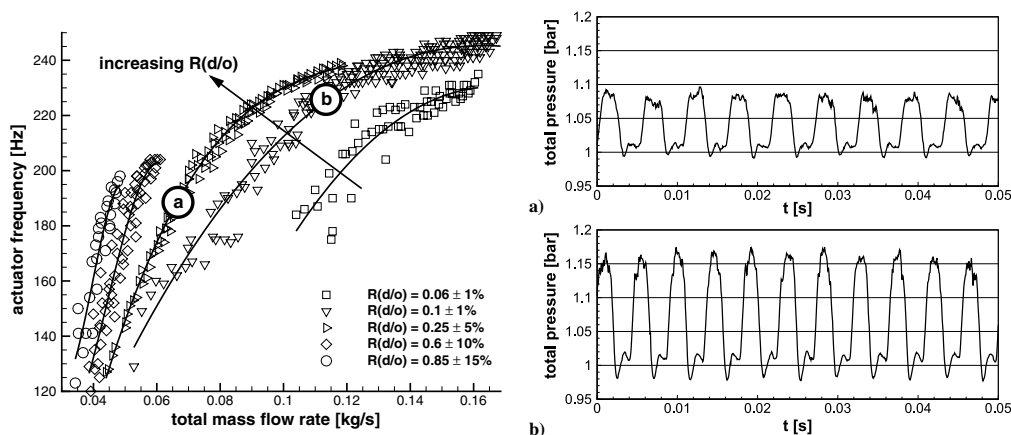


Fig. 3 Actuation frequency dependent on total mass flow rate and its distribution between driving and outlet stage. For the data points marked A and B, examples for the resulting total pressure signal of the emanating air jets are shown. The mass flow rate quoted is the one for the entire actuator system.

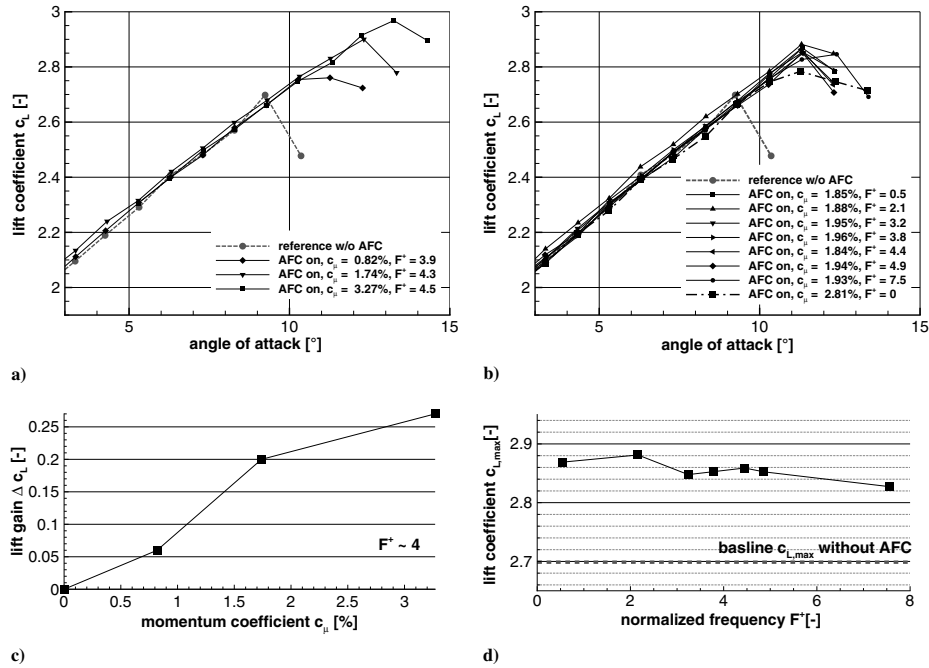


Fig. 4 Influence of momentum coefficient and actuation frequency on lift coefficient: a) variation of momentum coefficient, b) variation of actuation frequency, c) $c_{L,max}$ gain dependent on momentum coefficient, and d) maximum lift $c_{L,max}$ dependent on actuation frequency.

A. Force and Pressure

For the experiments, the angle of attack was changed from $\alpha = -5$ deg to a value beyond α_{max} by increments of 1 deg. For each angle of attack, static pressure and forces were measured and averaged over 4 s. Plots for the lift coefficient for different momentum coefficients c_μ applied are shown in Fig. 4a for the relevant angles of attack. These results were obtained with the oscillator-driven actuator system. The thick line shows the lift curve for the unforced flow. This is therefore the baseline with which the AFC cases are compared. Naturally, separation occurs for angles greater than $\alpha = 9$ deg and no more lift increase is possible. The results show that for increasing c_μ the achievable α_{max} before occurrence of separation increases. As higher incidence angles correspond to higher lift, the achievable maximum lift coefficient $c_{L,max}$ also increases with increasing c_μ (see Fig. 4c). The largest lift gain is achieved for the maximum momentum coefficient applied of $c_\mu = 3.27\%$, where α_{max} is offset by $\Delta\alpha = 4$ deg and lift is increased by $\Delta c_L = 0.27$. However, for smaller

c_μ values too, α_{max} is shifted, e.g., by $\Delta\alpha = 3$ deg for $c_\mu = 1.74\%$, resulting in a lift gain of $\Delta c_L = 0.20$.

In addition to varying the momentum coefficient, the effect of changing the actuation frequency was investigated. The valve-driven actuator system was employed for those cases. The results are given in Figs. 4b and 4d. They show that within the tested range of actuation frequencies the flow is indifferent to the specific time scale of forcing. Lift gain is similar for frequencies ranging from $F^+ = 0.5$ (25 Hz) to 7.5 (350 Hz). However, some kind of unsteady perturbations are necessary, which becomes obvious when comparing the resulting curves for pulsed blowing with the curve for continuous blowing (dash-dotted line). Even though the momentum coefficient is higher for the continuous blowing case, lift gain is reduced compared with all cases of pulsed actuation.

The pressure coefficient (c_p) distribution is displayed in Fig. 5a in the reference coordinate system of the main element. The pulsed jet in the forced case manifests as a kink in the c_p curve associated with the

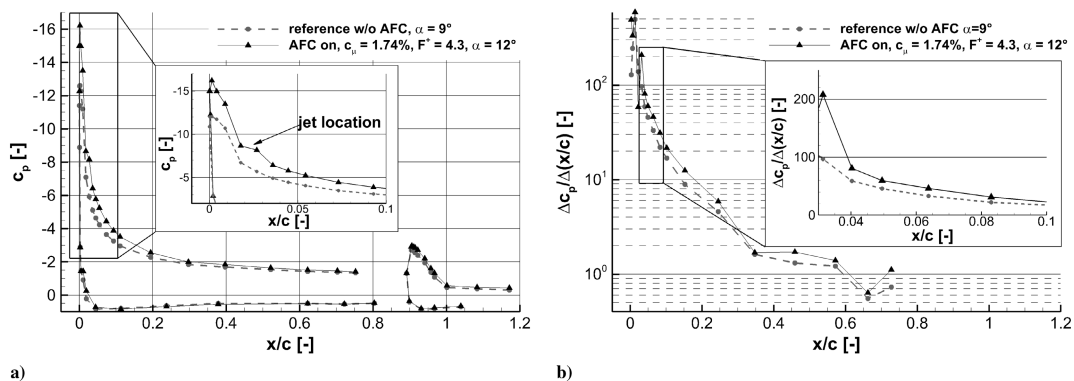


Fig. 5 Comparison of pressure coefficient (c_p) distributions illustrating that the forced flow is able to withstand stronger deceleration without separating from the wing: a) forced case ($c_\mu = 1.74\%$ and $F^+ = 4.3$) for $\alpha = 12$ deg and unforced case for $\alpha = 9$ deg just before separation occurs and b) comparison of explicit pressure gradient for the cases shown in panel a.

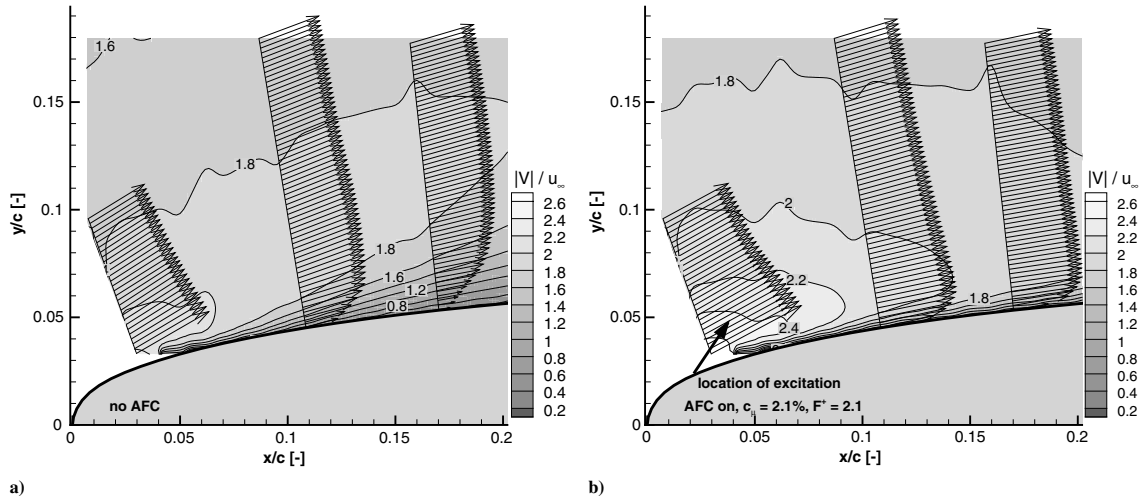


Fig. 6 Comparison of velocity fields from PIV for $\alpha = 11$ deg at leading edge: a) unforced flow and b) forced flow ($c_\mu = 2.1\%$, $F^+ = 2.1$).

suction side of the main element. Figure 5a shows a comparison of c_p distributions with and without pulsed blowing for respective angles of attack where the aerodynamic loading on the boundary layer is so high that any further increase would result in separation of the flow. For the forced flow, α_{max} is offset by $\Delta\alpha = 3$ deg and the surge tip decreases by an additional $\Delta c_p = 4$ to $c_{p,min} \approx -16$. Hence, as the main element's trailing-edge pressure remains unaffected, much higher recompression must occur on the identical geometry. The rate of recompression is shown explicitly in Fig. 5b, where $\Delta c_p / \Delta(x/c)$ is plotted for the suction-side surface of the main element. It is apparent that, when unsteady perturbations are introduced at the leading edge, stronger adverse pressure gradients can be sustained on the entire upper surface with fully attached flow. For the case presented of forcing with a momentum coefficient of $c_\mu = 1.74\%$ the achievable rate of recompression more than doubles (from $\Delta c_p / \Delta(x/c) = 95$ to $\Delta c_p / \Delta(x/c) = 205$) in the region immediately trailing the surge tip. The c_p distribution on the flap remains unaffected by flow control applied at the leading edge.

B. Velocity Field

Stereoscopic TR-PIV measurements on the leading and trailing edge of the main element allow for the analysis of the near-surface

velocity field. All data presented are time averaged from 1024 individual double exposures and normalized with the freestream velocity. The base flow is compared with forcing with a momentum coefficient of $c_\mu = 2.1\%$ and a normalized actuation frequency of $F^+ = 2.1$. Figure 6 shows the flowfield at the leading edge for the unactuated and actuated cases for an angle of attack of $\alpha = 11$ deg. The location of excitation is marked with an arrow in Fig. 6b. The velocity magnitude is calculated from the u , v , and w components, but only the in-plane velocity components are displayed as flow vectors for reasons of clarity.

The overall velocity level for the base flow is lower than for the forced case, as the flow turning and therefore the acceleration of the flow are reduced. The unforced flow separates in the region between 40 and 100 mm ($x/c = 6-16\%$) from the leading edge, which manifests in a decelerated flow near the wall and an outward direction of the flow as illustrated by the velocity vectors shown in Fig. 6a. This effect becomes even more apparent on the trailing edge, as presented in Fig. 7. Here, the region of low velocity has grown larger than the PIV interrogation area, which reaches up to a distance of 100 mm from the wing's surface. The forced flow on the other hand shows high velocity close to the wing, which indicates a fully attached flow. The velocity profile converges to a constant value approximately 10 mm away from the surface.

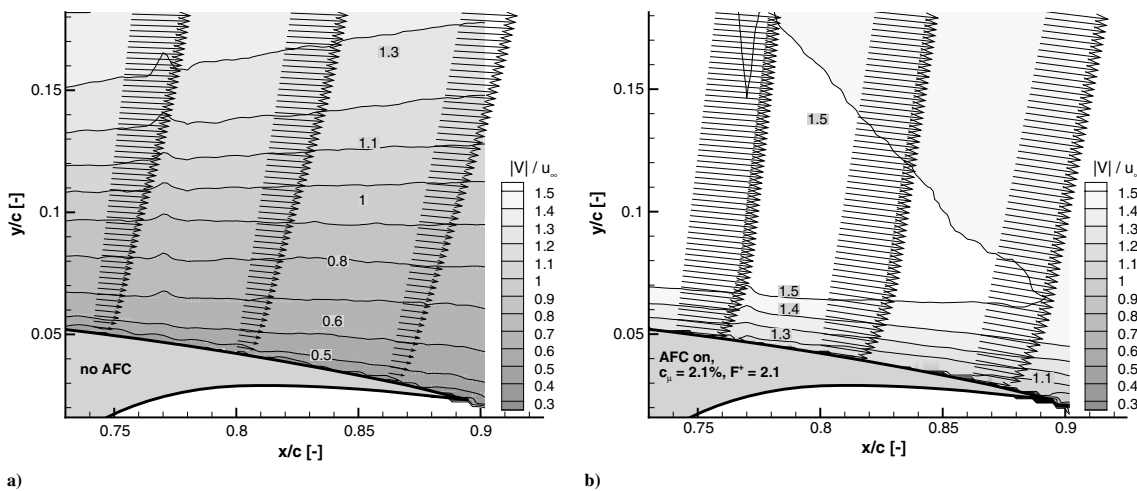


Fig. 7 Comparison of velocity fields from PIV for $\alpha = 11$ deg at trailing edge: a) unforced flow and b) forced flow ($c_\mu = 2.1\%$, $F^+ = 2.1$).

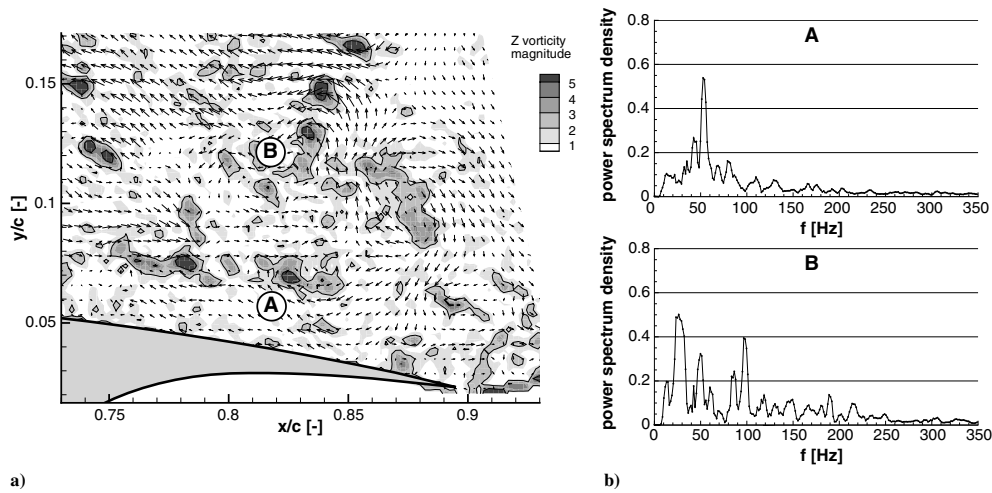


Fig. 8 Unsteady flow characteristics for the unforced detached flow: a) snapshot of z -vorticity magnitude and in-plane fluctuation velocity and b) power density spectrum at two locations (A and B) in the flowfield.

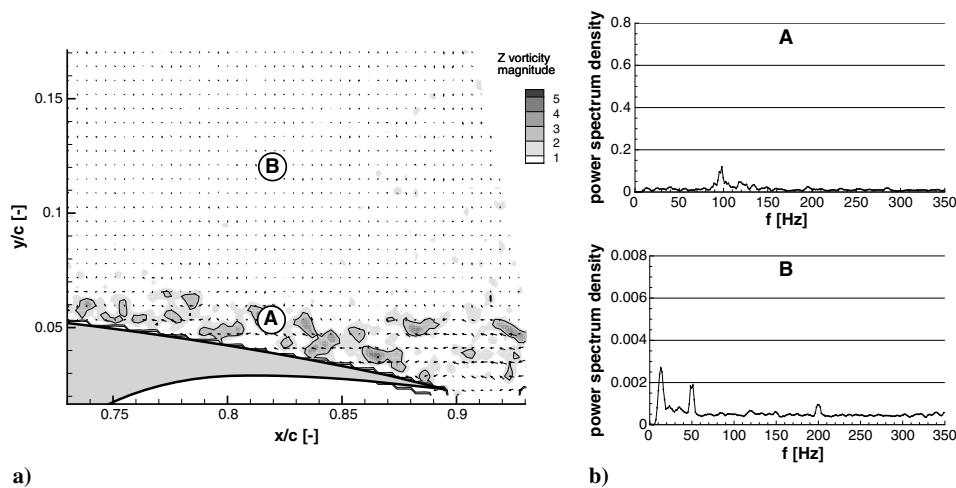


Fig. 9 Unsteady flow characteristics for the forced attached flow: a) snapshot of z -vorticity magnitude and in-plane fluctuation velocity and b) power density spectrum at two locations (A and B) in the flowfield.

C. Vorticity and Power Density Spectrum

Unsteady flow characteristics are analyzed in this section. For an individual time step the z -vorticity magnitude is calculated (from u and v velocity components) for the flowfield and displayed in Figs. 8a and 9a for the natural and actuated flow, respectively. The dominant frequencies in vorticity magnitude (calculated from u , v , and w velocity components) fluctuation are extracted from the TR-PIV data and presented in Figs. 8b and 9b. Actuation parameters are $c_{\mu} = 2.1\%$ and $F^{+} = 2.1$.

The results for the natural flow are shown in Fig. 8. As the flow is detached, the flowfield is dominated by large-scale vortical structures, which expand beyond the range of the PIV interrogation area. Frequency analysis is applied to two points (marked A and B) in the flowfield. Location A is at 7 mm, and location B is at 51 mm from the surface. In the unforced case, low-frequency high-amplitude fluctuation is apparent at both points. The highest amplitudes are found in a frequency range between 20 and 110 Hz. With increasing distance from the surface, only the peak at 54 Hz remains in the spectrum, which suggests that the other frequencies are sub- and higher harmonics of this base frequency. Normalizing this frequency

with the mean flow velocity ($c_{\text{mean}} = 30$ m/s) and the characteristic length of the main wing element ($c_{\text{ref,main}} = 0.54$ m) results in a Strouhal number of $St = 0.97 \approx 1$.

The unsteady characteristics of the flow change completely when leading-edge forcing is applied, as shown in Fig. 9. As the flow is attached, vorticity is now contained to a small layer close to the surface. There, the predominant frequency (location A in Fig. 9b) is the actuation frequency of 100 Hz ($F^{+} = 2.1$). At location B, which represents the far field of the flow, the power spectrum density shows only very low amplitudes of fluctuation velocity (note the different scaling of the axis). Peaks are found at 50 and 200 Hz, which are sub- and higher harmonics of the forcing frequency, but the amplitudes are more than two orders of magnitude smaller than in the near-surface region.

IV. Conclusions

AFC experiments were conducted on a two-element wind-tunnel model using a staged fluidic actuator system. The capability of pulsed jet actuation to delay stall is demonstrated. Measurements of the lift

force show that the stall angle of attack is increased with increasing actuation amplitude, whereas it is insensitive toward variation of forcing frequency within the tested bandwidth. The reason for the heightened α_{\max} and $c_{L,\max}$ is the flow's ability to withstand stronger adverse pressure gradients without separation when forcing is present. The velocity field above the surface at the trailing edge changes its characteristics completely when AFC is applied. Flow turning is increased and high momentum fluid is redirected to the near-surface region. In addition, whereas the natural flow is dominated by large-scale vortical structures in the separated region, vorticity is contained to a flat layer close to the wing in the controlled case, with the dominant frequency present being that of the pulsed air jets.

References

- [1] Smith, A. M. O., "High-Lift Aerodynamics," *Journal of Aircraft*, Vol. 12, No. 6, 1975, pp. 501–530.
doi:10.2514/3.59830
- [2] Melton, L., Schaeffler, N., Yao, C., and Seifert, A., "Active Control of Flow Separation from Supercritical Airfoil Leading-Edge Flap Shoulder," *Journal of Aircraft*, Vol. 42, No. 5, 2005, pp. 1142–1149.
doi:10.2514/1.10294
- [3] Melton, L., Schaeffler, N., and Lin, J., "High-Lift System for a Supercritical Airfoil: Simplified by Active Flow Control," AIAA Paper 2007-0707, 2007.
- [4] Scholz, P., Kaehler, C., Radespiel, R., Wild, J., and Wichmann, G., "Active Control of Leading-Edge Separation within the German Flow Control Network," AIAA Paper 2009-0529, 2009.
- [5] Kelley, C., Bowles, P., Cooney, J., He, C., and Corke, T., "High Mach Number Leading-Edge Flow Separation Control Using AC DBD Plasma Actuators," AIAA Paper 2012-0906, 2012.
- [6] Seifert, A., Bachar, T., Koss, D., Shepshelovich, M., and Wagnanski, I., "Oscillatory Blowing: A Tool to Delay Boundary-Layer Separation," *AIAA Journal*, Vol. 31, No. 11, 1993, pp. 2052–2060.
doi:10.2514/3.49121
- [7] Zander, V., Hecklau, M., Nitsche, W., Huppertz, A., and Swoboda, M., "Active Flow Control by Means of Synthetic Jets on a Highly Loaded Compressor Cascade," *Journal of Power and Energy*, Vol. 225, No. 7, 2011, pp. 897–906.
doi:10.1177/0957650911410275
- [8] Rathay, N., Boucher, M., Amitay, M., and Whalen, E., "Performance Enhancement of a Vertical Stabilizer Using Synthetic Jet Actuators: Non-Zero Sideslip," AIAA Paper 2012-2657, 2012.
- [9] Petz, R., and Nitsche, W., "Active Separation Control on the Flap of a Two-Dimensional Generic High-Lift Configuration," *Journal of Aircraft*, Vol. 44, No. 3, 2007, pp. 865–874.
doi:10.2514/1.25425
- [10] Haucke, F., and Nitsche, W., "Active Separation Control on a 2D High-Lift Wing Section Towards High Reynolds Number Application," AIAA Paper 2013-2514, 2013.
- [11] Seele, R., Graff, E., Lin, J., and Wagnanski, I., "Performance Enhancement of a Vertical Tail Model with Sweeping Jet Actuators," AIAA Paper 2013-0411, 2013.
- [12] Cattafesta, L. N., and Sheplack, M., "Actuators for Active Flow Control," *Annual Review of Fluid Mechanics*, Vol. 43, 2011, pp. 247–272.
doi:10.1146/annurev-fluid-122109-160634
- [13] Nagib, H., Kiedaisch, J., Wagnanski, I., Stalker, A., Wood, T., and McVeigh, M., "First-in-Flight Full-Scale Application of Active Flow Control: The XV-15 Tiltrotor Download Reduction," *RTO AVT Specialists' Meeting on "Enhancement of NATO Military Flight Vehicle Performance by Management of Interacting Boundary Layer Transition and Separation,"* Prague, Czech Republic, Proc. No. RTO-MP-AVT-111, 2004, pp. 29–1–29-36.
- [14] Seifert, A., David, S., Fono, I., Stalnov, O., and Dayan, I., "Roll Control via Active Flow Control: From Concept to Flight," *Journal of Aircraft*, Vol. 47, No. 3, 2010, pp. 864–874.
doi:10.2514/1.45910
- [15] Grund, T., and Nitsche, W., "Wind Tunnel and Flight Tests with Active Flow Control on a S10 Glider Configuration," *New Results in Numerical and Experimental Fluid Mechanics VIII*, edited by Dillmann, A., Heller, G., Kreplin, H., Nitsche, W., and Peltzer, I., Vol. 121, Notes on Numerical Fluid Mechanics and Multidisciplinary Design, Springer, New York, 2013, pp. 117–124.
- [16] Arwatz, G., Fono, I., and Seifert, A., "Suction and Oscillatory Blowing Actuator Modeling and Validation," *AIAA Journal*, Vol. 46, No. 5, 2008, pp. 1107–1117.
doi:10.2514/1.30468
- [17] Gregory, J., and Tomac, M. N., "A Review of Fluidic Oscillator Development," AIAA Paper 2013-2474, 2013.
- [18] Raghu, S., "Fluidic Oscillators for Flow Control," *Experiments in Fluids*, Vol. 54, No. 2, 2013, pp. 1–11.
doi:10.1007/s00348-012-1455-5
- [19] Wild, J., "Experimental Investigation of Mach- and Reynolds-Number Dependencies of the Stall Behavior of 2-Element and 3-Element High-Lift Wing Sections," AIAA Paper 2012-0108, 2012.
- [20] Bauer, M., Peltzer, I., Nitsche, W., and Goelling, B., "Active Flow Control on an Industry-Relevant Civil Aircraft Half Model," *Active Flow Control II*, edited by King, R., Vol. 108, Notes on Numerical Fluid Mechanics and Multidisciplinary Design, Springer, Berlin, 2010, pp. 95–107.

I. Gursul
Associate Editor

2.2 Bauer2014b

Bauer, M., Grund, T., and Nitsche, W.,

Experiments on Active Drag Reduction on a Complex Outer Wing Model,

AIAA Journal, 2014, DOI: 10.2514/1.J053515

Experiments on Active Drag Reduction on a Complex Outer Wing Model

Matthias Bauer,* Thomas Grund,† and Wolfgang Nitsche‡
Technische Universität Berlin, 10587 Berlin, Germany

DOI: 10.2514/1.J053515

The potential of active flow control by means of pulsed blowing to counter performance degradation at high angles of attack is demonstrated on a modern civil aircraft outer wing configuration provided by the European aeronautical industry. Flow control actuators are incorporated into the leading edge between the slat edge and the wingtip, where the wing's slender shape and its high local curvature do not allow for the integration of mechanical leading-edge devices. Surface flow visualization identifies the highly three-dimensional topology of the uncontrolled flow, which is dominated by the slat edge vortex and leading-edge flow separation at high incidence angles. The influence of the varying-momentum coefficient on drag reduction, lift gain, and aerodynamic efficiency is studied, considering force and pressure measurements, as well as flow visualization. Results indicate that a momentum coefficient of $c_{\mu} = 0.6\%$ suffices to reduce drag by up to 38%, compared to the uncontrolled baseline flow, and to offset aerodynamic performance degradation by 4 deg if the actuation effort is distributed efficiently along the span.

Nomenclature

A_{AFC}	=	total area of active outlets, m^2
A_{ref}	=	reference area for aerodynamic coefficients, m^2
b	=	span, m
$C_{D,norm}$	=	normalized drag coefficient; $C_D/C_{D,max,base}$
$C_{L,norm}$	=	normalized lift coefficient; $C_L/C_{L,max,base}$
c_p	=	pressure coefficient
c_{ref}	=	reference chord length, m
c_{μ}	=	momentum coefficient; $\dot{m} \cdot u_{jet,RMS}/q_{\infty} \cdot A_{ref}$
F^{+}	=	normalized forcing frequency; $f \cdot c_{ref}/u_{\infty}$
f	=	forcing frequency, Hz
\dot{m}	=	total mass flow rate, kg/s
s	=	slot centerline coordinate, m
$u_{jet,peak}$	=	peak jet velocity; $\dot{m}/\rho_{jet}A_{AFC}$, m/s
$u_{jet,RMS}$	=	root-mean-square value of $u_{jet,peak}$, m/s
u_{∞}	=	freestream velocity, m/s
x	=	streamwise direction, m
y	=	(spanwise) direction normal to tunnel floor, m
z	=	direction normal to tunnel side wall, m
α	=	angle of attack, deg
ρ_{jet}	=	density of air jet at outlet, kg/m^3

I. Introduction

ALL modern commercial airliners are equipped with mechanical high-lift devices to improve flight characteristics at low speed. Those devices are, to date, without an alternative to fulfill the performance requirements for start and landing, but they add weight and complexity to the overall system. However, their integration conflicts with developments in modern aircraft design. The diameters of jet engines have increased significantly over the past decades, as manufacturers realize higher bypass ratios in order to limit fuel consumption. To avoid the need for larger and heavier landing gear, those engines are moved closer to the wing. This makes it necessary to

increase the slat cutout (the section of the wing's leading edge where slats cannot be integrated), as they would collide with the nacelle when deployed. Slat integration also becomes problematic on the outer wing section due to its slender shape and high local curvature. Active flow control (AFC) technology might augment the overall high-lift system to prevent flow separation where mechanical devices cannot be integrated. Figure 1a shows a sketch of a civil airliner wing with regions prone to separation [1,2], where the two locations for possible AFC integration previously described are marked.

In this paper, we describe and analyze wind-tunnel experiments on the application of flow control by means of pulsed blowing applied at the outer wing section between the slat edge and the wingtip. The impact of local flow separation there on aerodynamic performance becomes apparent in the polar plot, presented in Fig. 1b, showing the wind-tunnel measurement data of the Do728 airliner (data from [3]). At an angle of attack well below stall angle, a sudden drag increase occurs and manifests as a kink in the polar. Our aim is to prevent early flow separation at high angles of attack in order to limit drag increase and to improve the wing's aerodynamic efficiency. A numerical study on this specific configuration is presented in [1], in which the authors demonstrate the successful delay of flow separation toward higher angles of attack and significant drag reduction. In practice, this aspect becomes relevant in the second segment of climb [4], when the landing gear is retracted and a minimum gradient of climb is prescribed, even with one engine inoperative. In [5], the climb gradient $\tan(\gamma)$ is defined as a function of available thrust T , aircraft weight W , the aerodynamic efficiency, and the ratio of lift L and drag D :

$$\tan(\gamma) = \frac{T}{W} - \frac{1}{(L/D)}$$

Although the available thrust and weight are specific characteristics of an aircraft type, we aim at increasing the lift-to-drag ratio L/D by AFC, which feeds forward directly to a steeper climb gradient. Note that, in our experiments, the onset of leading-edge separation on the outer wing model coincides with the maximum angle of attack with respect to lift. This would not be the case on a full wing, where the (much larger) lifting surface from the wing's root to the outer slat edge would continue to provide increasing lift for increasing incidence angles. A stalled outer wing section, however, reduces the overall aerodynamic performance of the wing in an angle-of-attack range that is relevant from an operational point of view.

Flow control applied to the wing leading edge is a topic of ongoing research [6–9]. Those experiments were conducted on slatless (one or two element) airfoils. The work focused primarily on increasing the maximum lift and stall angle, but research on localized flow control also found its way into industry research with a broader, multidisciplinary

Received 2 April 2014; revision received 8 September 2014; accepted for publication 11 September 2014; published online 16 December 2014. Copyright © 2014 by the American Institute of Aeronautics and Astronautics, Inc. All rights reserved. Copies of this paper may be made for personal or internal use, on condition that the copier pay the \$10.00 per-copy fee to the Copyright Clearance Center, Inc., 222 Rosewood Drive, Danvers, MA 01923; include the code 1533-385X/14 and \$10.00 in correspondence with the CCC.

*Ph.D. Student, Department of Aeronautics and Astronautics; matthias.bauer@ilr.tu-berlin.de.

†Ph.D. Research Scientist, Department of Aeronautics and Astronautics; thomas.grund@ilr.tu-berlin.de.

‡Professor, Department of Aeronautics and Astronautics; wolfgang.nitsche@ilr.tu-berlin.de.

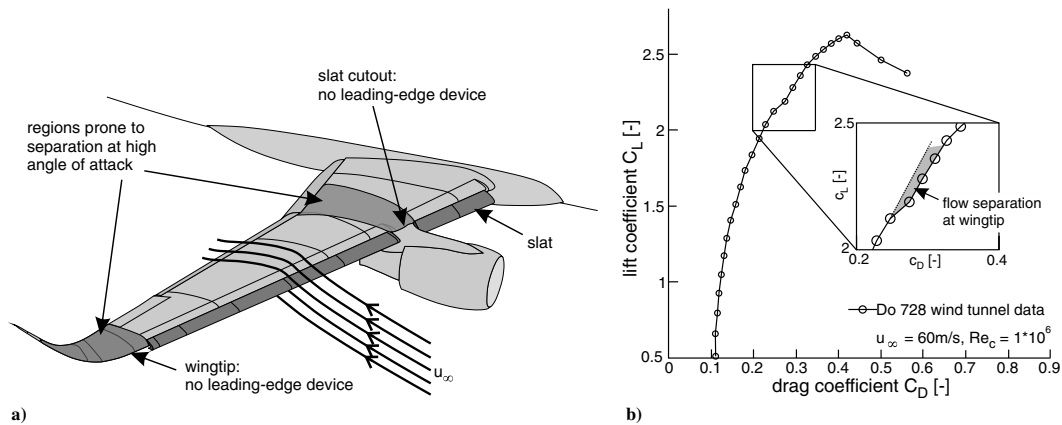


Fig. 1 Representation of regions prone to separation a) and wind-tunnel data of the Do728 airliner b).

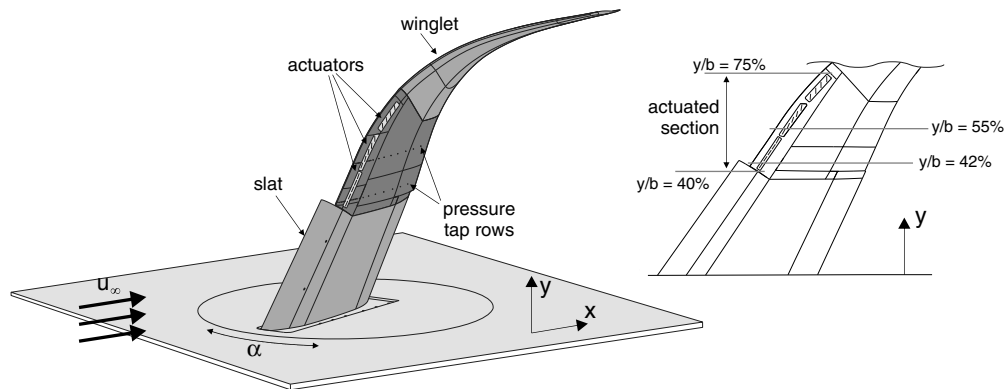


Fig. 2 Outer wing model experimental setup.

basis [10]. A common approach is to employ unsteady excitation instead of continuous blowing, as this was found to be more efficient [11]. Our flow control system incorporates fluid amplifier components. This technology was first researched at the Harry Diamond Laboratories [12] in the early 1960s. The fluid amplifiers are attractive for generating pulsed-air jets, as they are efficient and robust. They are employed, e.g., in [13,14] in experiments to improve the rudder effectiveness of the vertical tail plane model.

In the present experiment, we employ a staged fluidic system: Arrays of fluidic diverters are driven by either a mechanical valve or a fluidic oscillator. Here, we present results with the valve-driven system only, as this allows us to completely decouple the frequency from the amplitude of actuation. We study the effect of spanwise distribution of the actuation and investigate the influence of the introduced momentum coefficient on drag reduction, lift increase, and stall angle. With a suitable combination of control parameters, we reduce drag forces acting on the outer wing model by up to 42% and increase the aerodynamic efficiency of the wing section investigated by more than 80% compared to the respective baseline values.

II. Experimental Setup

This section describes the wind-tunnel model including the fluidic actuator system and specifies the experimental uncertainty.

A. Wind-Tunnel Model and Instrumentation

The outer wing model investigated is tapered and swept back at an angle of 35 deg. It consists of three distinct sections with different

aerodynamic behaviors. The inner section is equipped with a slat that is deployed to a takeoff setting with a sealed slat gap. On an aircraft, this sealed gap is realized by positioning the slat so that it touches the main element. In our experiments, we additionally employed thin aluminum tape to ensure that no flow is allowed between the slat and the main element. At this section's trailing edge, an aileron is deflected to a fixed angle. The middle part of the model is not equipped with a slat. The leading-edge radius is small, as it is optimized for cruise. Therefore, this section is prone to leading-edge separation at high incidence angles. Our flow control system is installed here. Adjacent to that, a winglet forms the third section of the model (see Fig. 2).

The span b of the model measures 1040 mm. Its reference chord length c_{ref} is 443 mm. All experiments were conducted at a chord Reynolds number of $Re_c = 1.05 \times 10^6$ and a Mach number of $Ma \approx 0.13$. Tripping was applied to ensure a turbulent state of the boundary layer on the model and to minimize transition effects. Two strips of tape (40 μm high and 1 mm wide) were attached at $x/c = 0.1\%$ and $x/c = 0.5\%$ on the pressure side of the model. At high incidence angles, the stagnation point was located beyond that position on the pressure side, and the tripping affected the suction side surface.

The model is mounted on a six-component strain-gauge balance located beneath the wind-tunnel floor, and forces and moments acting on the model were measured directly. The force exerted by the pulsed-air jets was measured directly for each momentum coefficient and actuator segment at still air, and these values were subtracted from the results recorded during the experiments. This approach is based on the considerations presented in [15], in which the authors

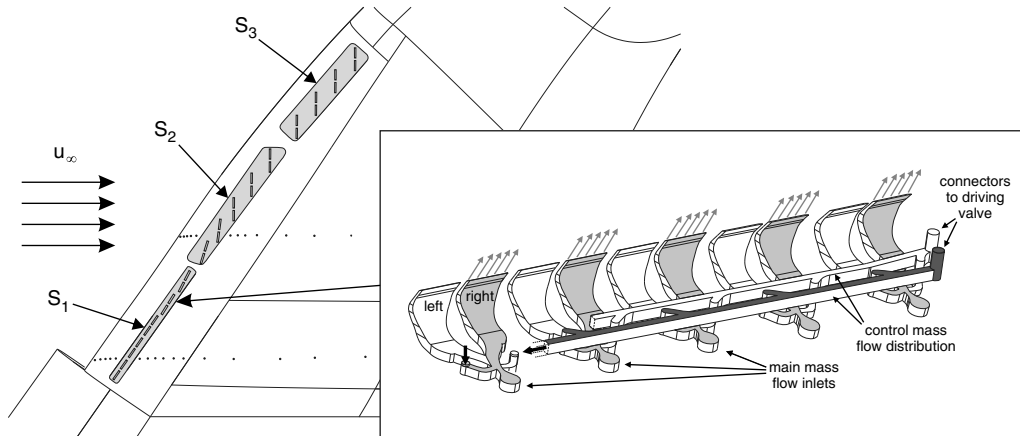


Fig. 3 Illustration of the outlet geometry and the internal structure of one actuator segment.

add the momentum coefficient to the drag coefficient to include it in efficiency calculations. The aerodynamic coefficients are calculated from the modified values. Thus, the results compensated for the added momentum, which allows for the undistorted comparison of baseline drag and lift to the respective values of the controlled flow. The model is equipped with 48 static pressure taps in two rows (at $y/b = 42\%$ and $y/b = 55\%$) oriented in a streamwise direction. The inner row comprises 30 stations on the suction and pressure surface, and the outer row comprises 18 stations on the suction side surface only. In addition, oil and tuft flow visualizations were employed to study the surface flowfield.

Rotating the balance around the y axis allows for varying the angle of attack of the model.

All experiments were conducted at the big wind-tunnel facility (known as GroWiKa) at the Technische Universität Berlin,[§] which is a closed-circuit wind tunnel with a 1400×2000 mm test section.

B. Active Flow Control System

The controlled section of the wing model spans from $y/b = 40\%$ to $y/b = 75\%$, as separation occurs here first. A total of 28 rectangular slots, measuring 11.2×0.8 mm and grouped in three segments, is integrated at approximately $x/c = 9\%$ of the chordwise position on the suction side surface. Geometric restraints did not allow the AFC system to be moved any closer to the leading edge. Through those slots, compressed air is ejected periodically. The air jets are tilted by 30 deg relative to the model's surface. Their orientation with respect to the leading-edge changes along the span. For the most inboard actuator, the slots are aligned parallel to the leading edge. Each subsequent actuator is rotated incrementally so that the most outboard slots are oriented perpendicular to the chord and the freestream flow direction. Hence, the surface area covered by the air jets is increased compared to a setup with uniform slot orientation. The outlet geometry and a fluidic actuator segment are presented in Fig. 3, where the grayed area of the segment illustrates the internal flow for a given point in time when the "right" outlets are active.

The pulsed-air jets are generated using arrays of fluidic diverter elements, which are based on the principle of fluid amplification [16]. An alternating pressure source applied to the diverters' control ports pushes the fluid entering to either side, and therefore switches the outflow periodically between the two respective outlets of one diverter. As a result, the pulsed jet flow of neighboring slots is phase shifted by 180 deg. For the experiments presented, we employed fast-switching solenoid valves to provide the actuator elements with the

required pneumatic driving signal. By doing so, we could easily manipulate the switching frequency imposed on the actuator elements with an electrical signal generator. Approximately 10% of the total mass flow is routed through the valves as driving mass flow. The fluidic actuators are integrated into segments of five (S1 and S2) or four (S3) individual elements. Each segment is driven by one solenoid valve. When multiple segments were operated simultaneously, they were controlled by a single electrical signal. Therefore, all segments operate in phase with the same frequency. As switching between respective outlets of one diverter is induced by the mass flow that propagates through the control flow channels, there is a phase lag between the two neighboring actuator elements of one segment. In contrast to the forcing frequency, the supply air pressure for each segment is controlled independently by a pressure regulator valve, allowing different forcing amplitudes across the segments. Mass flow meters based on a thermoelectrical principle are used to measure the flow rate of the ejected air for each actuator array.

All momentum coefficients quoted are calculated using

$$c_{\mu} = \frac{\dot{m} \cdot u_{\text{jet,RMS}}}{q_{\infty} \cdot A_{\text{ref}}}$$

where $u_{\text{jet,RMS}}$ is the root-mean-square value of the peak jet velocity. Assuming a uniform velocity profile (plug flow) across the outlet and the form of a square wave signal in time, $u_{\text{jet,RMS}}$ can be approximated by

$$u_{\text{jet,RMS}} = \frac{1}{2\sqrt{\text{DC}}} u_{\text{jet,peak}}$$

The duty cycle (DC) describes the fraction of time that one outlet is active during one switching cycle. It is fixed to 50% (DC = 0.5) in our studies. The peak jet velocity $u_{\text{jet,peak}}$ is calculated from the measured mass flow rate \dot{m} , the area of the active actuator outlets A_{AFC} , and the density of the fluid at the outlets ρ_{jet} using

$$u_{\text{jet,peak}} = \frac{\dot{m}}{\rho_{\text{jet}} A_{\text{AFC}}}$$

The respective jet densities for different mass flow rates were established in benchtop experiments. This was done by first calculating the peak Mach number of the air jets from the measured total and static pressure at the outlets using isentropic relation. From this value and the total temperature measured in the actuators' plenum, the static temperature in the jet was calculated assuming an isentropic process. The calculated temperature together with the measured static pressure at the outlets allow for calculating the

[§]Data available online at <http://fd.tu-berlin.de/en/facilities/wind-tunnels/growika/> [retrieved 2014].

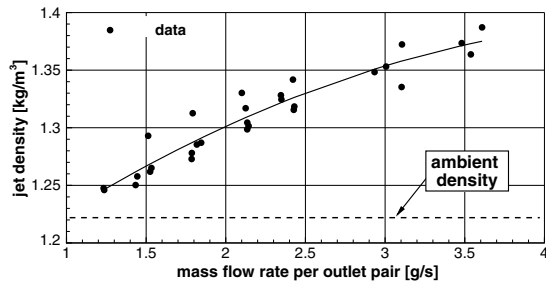


Fig. 4 Correlation of fluid density at outlets and mass flow rate.

relevant air jet density using an equation of state. The resulting correlation between the mass flow rate and the density is provided in Fig. 4. The AFC system performance was evaluated before wind-tunnel testing to ensure a sufficiently homogeneous jet velocity distribution along the span. For that purpose, the total pressure along the centerline of each outlet was measured with a pitot tube connected to a Kulite pressure transducer. For the inboard segment, one exemplary jet total pressure distribution for a moderate mass flow rate is presented in Fig. 5a for one point in time during the switching cycle to document the spanwise homogeneity. Those results show that the peak total pressure measured at the individual outlets lies within $\pm 2\%$ of the average peak value recorded across all outlets. In Fig. 5b, a time history of the air jet total pressure at the center of one outlet is plotted to document the switching quality of the actuator operated at 150 Hz. During the half-cycle, a given slot of the outlet pair of one actuator element is inactive; there is inflow into that orifice. This is an effect of the high-velocity flow inside the switching body that entrains fluid through the open (and inactive) actuator orifice.

C. Experimental Uncertainty

The experimental uncertainty in determining the drag and lift force using the balance system is estimated to be within the range of $\pm 0.025\%$ of cited values. No wind-tunnel correction is applied, as only changes in drag and lift are considered. The manufacturer specifies an accuracy of $\pm 0.5\%$ for the sensors used for measuring the pressure distribution on the model, which corresponds to an error of less than 25 Pa. For the Kulite pressure transducers used for measuring total and static pressure at the actuator outlets, the manufacturer specifies a typical measurement uncertainty of less than $\pm 0.1\%$ of the full-scale span of 0.7 and 0.35 bar, respectively. The momentum coefficient is calculated from the mass flow rate through the outlet slots measured in situ during the experiments and the jet density at the outlets, which was determined in benchtop experiments as previously described. The deviation of the momentum coefficients quoted from the exact values is determined by the simplifying assumptions regarding velocity profile in time and space and the measurement error in the mass flow rate and density. This (absolute)

uncertainty is difficult to quantify. However, as the uncertainty in the density and velocity profile produces a systematic error, the relative uncertainty between the various c_μ values quoted is determined by the uncertainty in measuring the mass flow rate only, which is specified with $\pm 1\%$ of the sensors' full-scale range. This translates to an uncertainty in c_μ of approximately $\pm 0.02\%$.

III. Results

The major findings of our wind-tunnel experiments are presented in this section. We describe the topology of the base flow and discuss the effects of flow control on the aerodynamic performance of the model wing. All aerodynamic coefficients presented are normalized with their respective base-flow values $C_{D,\min,\text{base}}$, $C_{L,\max,\text{base}}$, and $(C_D/C_L)_{\max,\text{base}}$. With the exception of the base flow, where we show results for the entire range of angles of attack tested; the range of the abscissa axis is limited to the region of interest but constant for all figures presented.

A. Base Flow

Tuft flow visualization was used to investigate the direction and steadiness of the surface flow for the entire range of angles of attack tested. Observations for relevant angles of attack are presented in Fig. 6. For incidence angles much smaller than α_{\max} (Fig. 6a), the surface flow shows no recirculation or orientation that is opposite to the expected flow direction for attached flow. It shows no signs of unsteadiness, with the exception of the region downstream of the slat edge and a small area near the trailing edge close to the wingtip. Flow unsteadiness increases significantly on the slatless section of the wing at an angle of attack close the stall angle (Fig. 6b). The flow is directed outward (towards the wingtip) in this region, and although the measured lift force still increases, local separation is observable on the model's outboard section. Further increasing the angle of attack (Fig. 6c) leads to leading-edge stall of the entire slatless section, with strong backflow and highly unsteady flow direction. No separation is observed downstream of the slat up to 80% of the chord position. The characteristic topology of the separated flow is presented in Fig. 7a. Oilflow visualization was used to identify the features of the separated flow on the suction side surface of the wing. Two longitudinal vortices dominate the structures on the inboard half of the model. One strong longitudinal vortex is formed due to the interaction of the lifting surface and the wind-tunnel wall, which grows in strength and cross section with increasing angle of attack. This feature would not be present on a full wing. The second longitudinal vortex forms at the slat edge (slat edge vortex). It causes the streamlines in its vicinity to curve toward the wingtip. When the stall angle of attack is reached, the flow separates abruptly from the surface. The separation line is located at approximately 10% of the x/c position, with strong backflow trailing the separation. Next to the slat edge vortex, a recirculation region (rotating in counterclockwise sense) is formed, reaching up to $x/c = 2\%$ of the chord position. The pressure coefficient distribution at two locations is shown in Fig. 7b for cases before and after stall occurs. The outboard pressure tap row (only data for the suction side

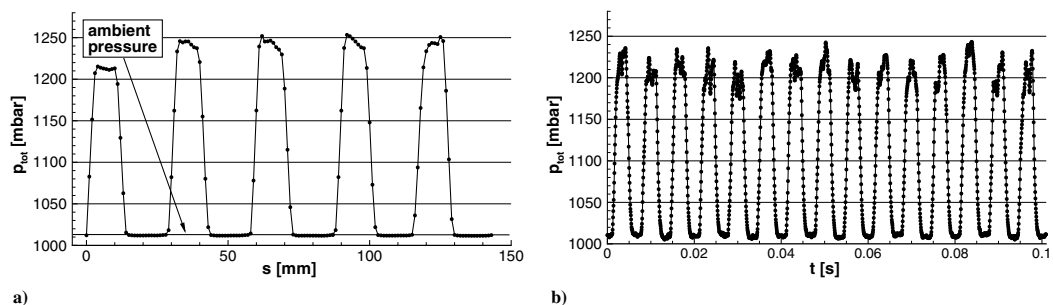


Fig. 5 Air jet total pressure at the actuator's outlet: a) spatial distribution; and b) time history.

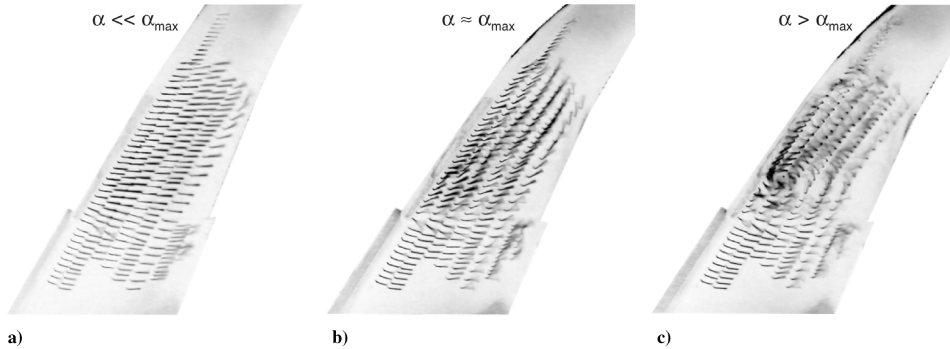


Fig. 6 Tuft visualization of the base flow for three angles of attack: a) completely attached flow; b) onset of stall; and c) stalled wing.

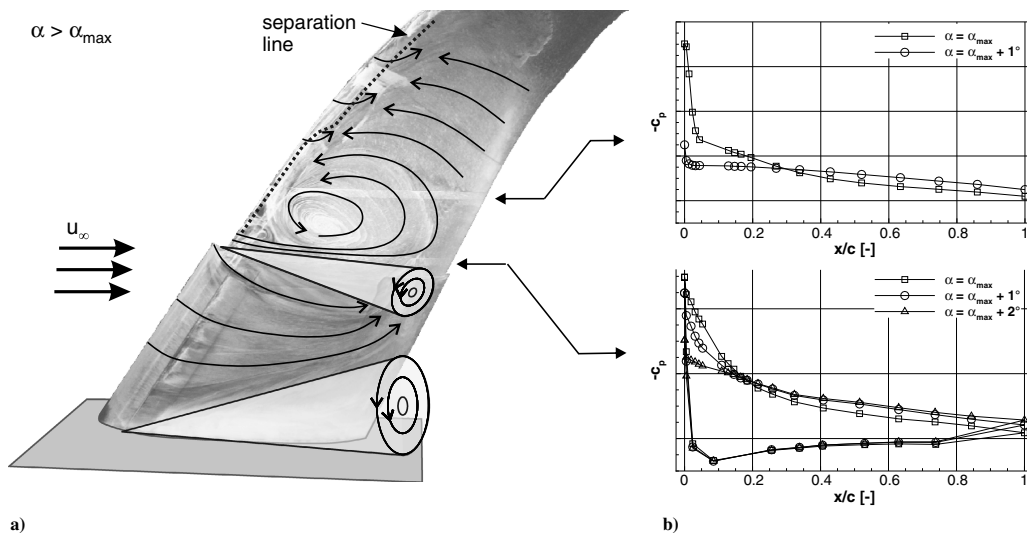


Fig. 7 Characterization of the base flow: a) oilflow visualization with highlighted topology; and b) pressure coefficient distribution at two positions for cases before and after stall.

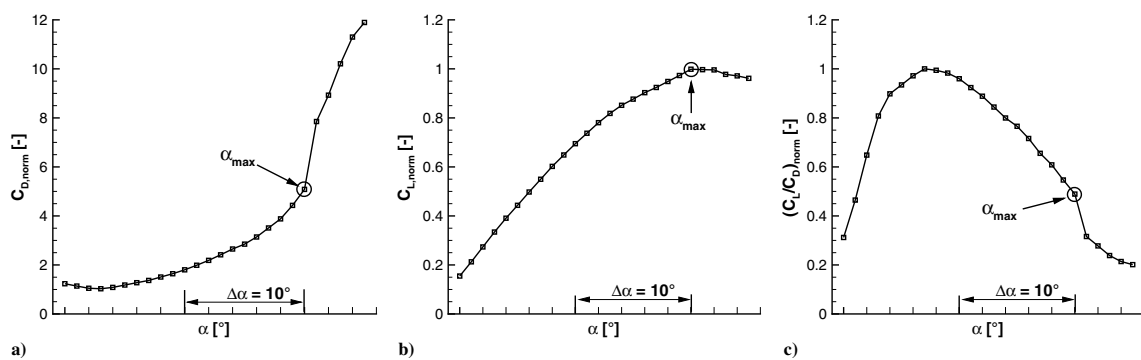


Fig. 8 Baseline force data for the tested range of angles of attack: a) drag coefficient, b) lift coefficient, and c) aerodynamic efficiency: lift-to-drag ratio.

are plotted) shows a significant decrease in the suction peak in poststall to one-third of its value at α_{max} . Recompression is reduced on the entire surface, and the trailing-edge pressure is lower than for the unstalled wing. Those tendencies are also found for the inboard pressure tap row, but to a lesser extent. In the vicinity of the slat edge vortex, the flow is more stable; therefore, the suction peak

is reduced by only 10%. A further increase in the angle of attack leads to a breakdown of the suction peak at the inboard pressure tap row too.

Results from the force measurements for the uncontrolled flow are presented in Fig. 8. These are the reference data to which the controlled cases are compared. The maximum angle of attack is

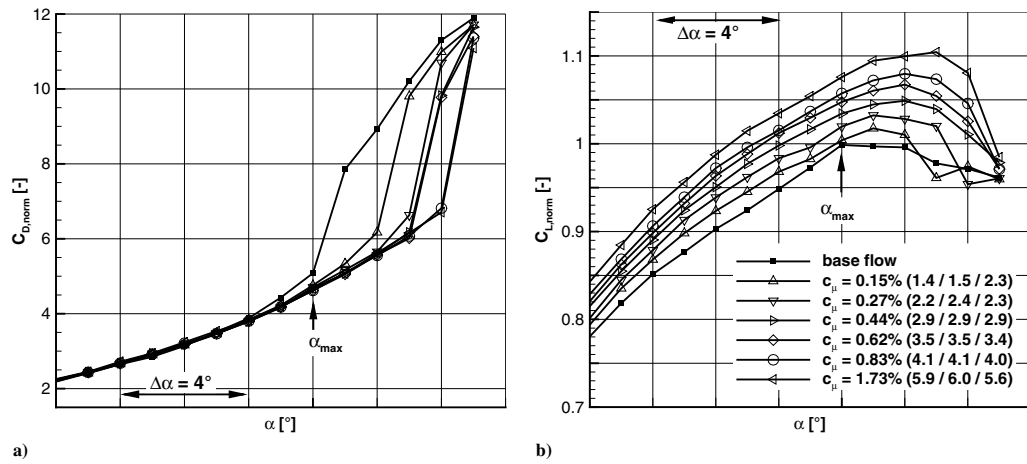


Fig. 9 Representation of a) drag coefficient and b) lift coefficient for different momentum coefficients.

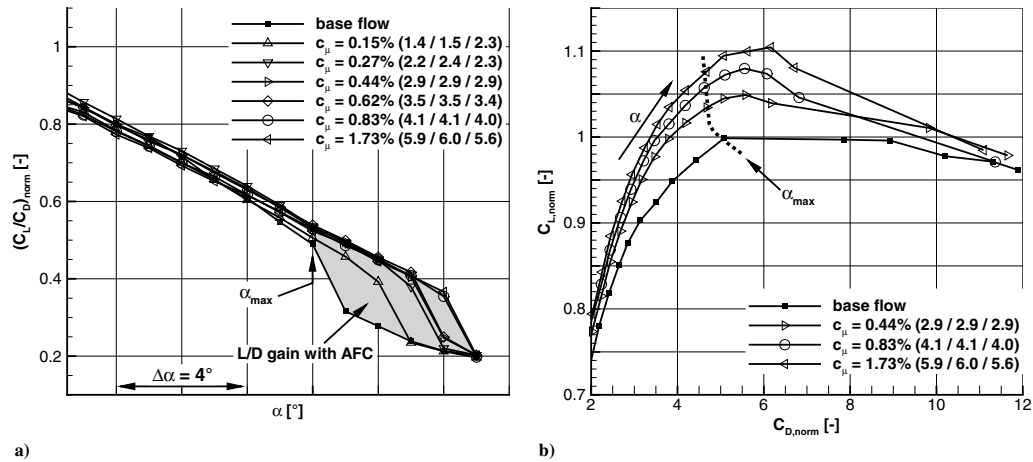


Fig. 10 Representation of a) lift-to-drag ratio and b) drag polar for different momentum coefficients.

defined as the angle for which the highest lift coefficient is observed. Further increasing the incidence angle results in a sudden increase in drag and a drop in aerodynamic efficiency.

B. Controlled Flow

The results for the controlled flow are presented in this section. At the beginning of the campaign, the influence of actuation frequency (with all other parameters kept constant) on flow control results was evaluated, and no significant change in control authority was found within the frequency range [50 Hz ($F^+ \approx 0.6$) to 250 Hz ($F^+ \approx 2.9$)] tested. Therefore, we used the fixed frequency of 150 Hz ($F^+ \approx 1.75$) for all cases presented here.

The resulting drag and lift curves for forcing with different momentum coefficients are shown in Fig. 9. For this case, the velocity ratio of the peak jet velocity to the freestream velocity ($u_{jet, peak} / u_{\infty}$) was kept constant across the three segments. The respective values are quoted in the figure legend next to the momentum coefficient, and they are ordered from inboard (S1) to outboard (S3), e.g., $((u_{jet, peak} / u_{\infty})_{S1} / (u_{jet, peak} / u_{\infty})_{S2} / (u_{jet, peak} / u_{\infty})_{S3})$. Figure 9a illustrates that, for increasing the momentum coefficient, the angle before drag increases abruptly and can be offset by up to 4 deg. Independent of c_{μ} , drag remains unaffected from flow control up to $\alpha_{max} - 2$ deg.

From there on, all levels of forcing tested reduce drag slightly and, to the same extent, until the original α_{max} is reached. The lowest c_{μ} applied of 0.15% offsets the significant drag increase by 2 deg. Increasing the momentum coefficient up to 0.83% incrementally shifts this angle to 4 deg above α_{max} , which corresponds to a drag reduction of 39% compared to the unactuated flow. A further increase of the forcing amplitude does not affect the drag on the wing. Even forcing with more than double that momentum coefficient ($c_{\mu} = 1.73\%$) is not more beneficial in terms of drag reduction. In contrast to drag, the lift force is affected by flow control over the entire range of angles tested, and no saturation is found with respect to the lift increase with increasing momentum coefficient (see Fig. 9b). For the highest value of c_{μ} applied ($c_{\mu} = 1.73\%$), the lift is enhanced by 11% relative to the uncontrolled $C_{L, max}$ and by 8% for $c_{\mu} = 0.83\%$, which is the highest value that provided significant drag reduction before saturation. For the uncontrolled flow, the maximum angle of attack before drag increases concurs with the stall angle at which lift decreases. It is interesting to note that this is not the case for the controlled flow. The maximum angle of attack is offset differently for different amplitudes of forcing, but in all cases, stall occurs earlier than the significant drag increase becomes apparent. Dividing C_L by C_D gives the aerodynamic efficiency of the wing segment, which is of

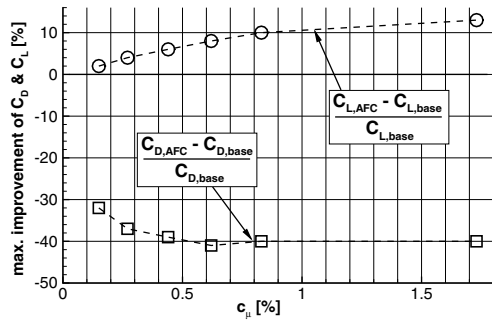


Fig. 11 Maximum (max.) benefit with respect to lift increase and reduction of drag in percentages for different momentum coefficients.

interest for the aim of increasing the climb gradient of an aircraft. This quantity is plotted in Fig. 10a for the momentum coefficient variation previously discussed. Similar to the presentation of the drag and lift coefficients, only the region of the maximum angle of attack is considered, although the apparent lift increase across all angles would contribute to an improved aerodynamic efficiency for $\alpha \ll \alpha_{max}$. We find that the improvement in aerodynamic efficiency is driven by drag reduction rather than by increasing lift. Depending on the momentum coefficient, the allowable angle before a sudden drop in efficiency occurs is offset by up to 4 deg, but even the lowest forcing amplitude increases that range by 2 deg and leads to an increase of the ratio C_L/C_D by 46%. For higher-momentum coefficients, the aerodynamic efficiency more than doubles compared to the uncontrolled case. This finding is again clearly observable in Fig. 10b, which shows C_L plotted against C_D . Note that the results for several momentum coefficients tested were omitted to increase the readability. The gradient of each curve increases for the increasing momentum coefficient, indicating an improvement of the glide ratio. The maximum benefit (decrease in drag and increase in lift) of the flow control cases previously presented is plotted in Fig. 11 versus the momentum coefficient. The values presented are changes in percent with respect to the uncontrolled baseline flow. The saturation in c_μ for the reduction of drag becomes apparent as previously denoted, and although no saturation is reached with respect to lift gain, the gradient of the lift gain curve is reduced for the high-momentum coefficient compared to forcing with low amplitudes.

The strongly three-dimensional characteristics of the model and flow suggest that a constant forcing amplitude along the model's span might be suboptimal in terms of actuation efficiency. To test that

assumption, we make use of the possibility to set actuation amplitudes of individual segments independently. In Fig. 12, the resulting drag and lift curves are presented for flow control with a momentum coefficient of $c_\mu = 0.33\% \pm 0.06\%$. Although keeping the total momentum added constant, the jet amplitude, and hence the local control authority of different segments, was varied. With respect to drag (see Fig. 12a), the control approach with all three segments working with the same amplitude performs best, shifting a significant drag increase by 3 deg. Operating the two inner segments (S1,S2) and the inner segment alone (S1) provides an offset of α_{max} by 3 deg, but it results in slightly higher drag. Forcing with the inner and outer segments only (S1,S3) reduces the effect of flow control, and a drag increase occurs 1 deg earlier. The lift gain (Fig. 12b) is independent of the distribution of the actuation for angles lower than α_{max} , but $C_{L,max}$ and the offset of the stall angle are sensitive toward the local amplitude of forcing. The trend is different than with drag. Here, equal distribution of the actuation produces the least lift gain, whereas control with segments S1 and S3 has the largest positive effect on lift, offsetting stall by 2 deg. Compared to that case, forcing with the inner segment (S1) only increases the stall angle by one additional degree (although the momentum coefficient is $c_\mu \approx 0.08\%$ lower), but $C_{L,max}$ is lower. Considering those two cases suggests that there is strong interaction of the flow in the spanwise direction and increasing lift on one part of the wing leads to higher aerodynamic loading, and therefore earlier separation. Those results show that, for a momentum coefficient of $c_\mu \approx 0.3\%$, no apparent advantage is found using locally diversified actuation, as the overall flow control effectiveness is not increased within the scope of the parameter combinations tested. This is different for actuation with higher amplitudes.

In Fig. 13, we present the resulting drag and lift curves for a spanwise variation of forcing amplitudes analogous to the one previously presented but using a higher-momentum coefficient of $c_\mu = 0.6\% \pm 0.05\%$. Forcing only with the inboard and outboard segments (S1 and S3) is similarly the least beneficial approach in terms of drag reduction (see Fig. 13a), but in contrast to the low-momentum coefficient case, the best results are now produced using the inboard and middle segments (S1 and S2) rather than employing all three segments simultaneously. Forcing with those two segments offsets the critical drag increase by 4 deg, whereas the other combinations of segments and distributions of actuation amplitude tested result in an offset of 3 deg or less. Although the lift gain is highest for the setup that results in maximum drag reduction, no additional beneficial effect is observed when considering stall angle (see Fig. 13b). The maximum angle with respect to lift is offset by 3 deg for the optimal parameter set, which is similar to the other combinations of segments and forcing amplitudes tested. With

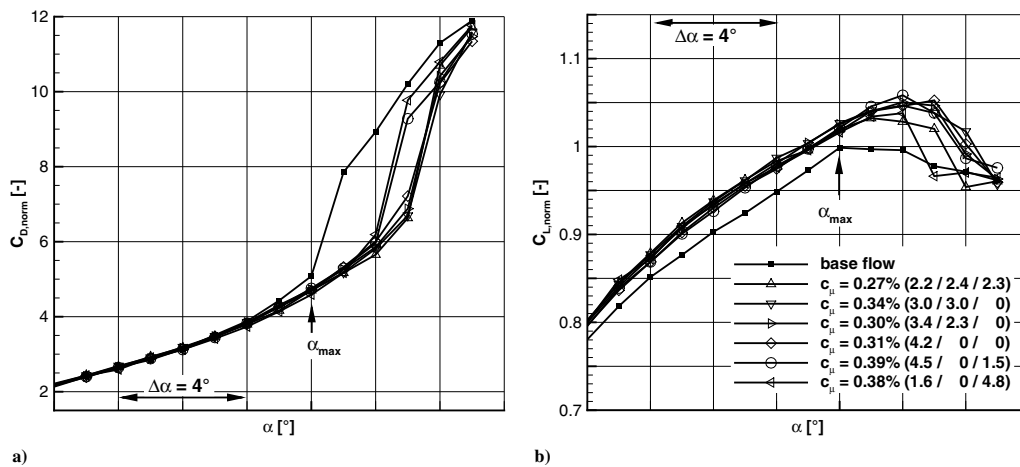


Fig. 12 Representations of a) drag coefficient and b) lift coefficient for $c_\mu \approx 0.33\% \pm 0.06\%$ with different spanwise distributions of actuation intensity.

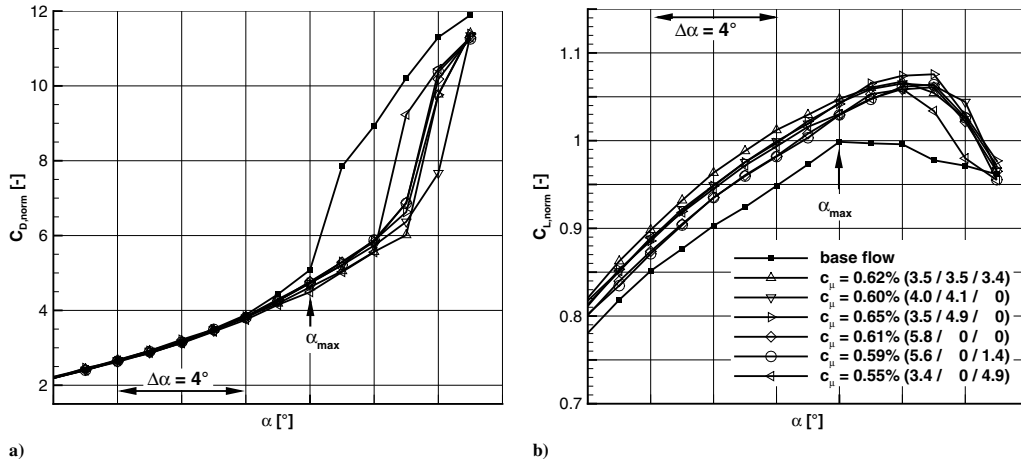


Fig. 13 Representations of a) drag coefficient and b) lift coefficient for $c_{\mu} \approx 0.6\% \pm 0.05\%$ with different spanwise distributions of actuation intensity.

respect to aerodynamic efficiency (see Fig. 14), this optimum configuration produces an increase of 58% compared to the baseline case at 4 deg beyond the original α_{max} . The benefit is as high as 74% for up to 3 deg beyond the base-flow stall angle.

The observation of the inner two segments contributing the most to the aerodynamic performance improvement is explained by the interaction of the different segments. From tuft visualization, it

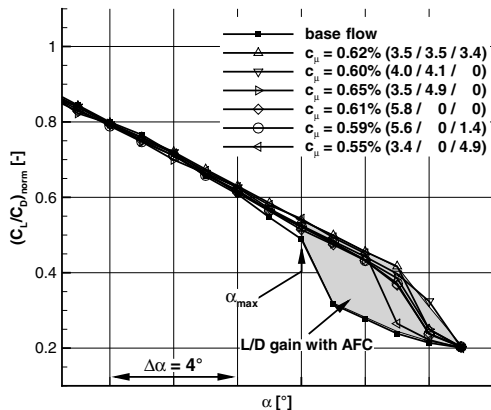


Fig. 14 Lift-to-drag ratio for $c_{\mu} \approx 0.6\% \pm 0.05\%$ with different spanwise distributions of actuation intensity.

becomes apparent that the inner segment, which is operated at a sufficiently high forcing amplitude, is capable of preventing flow separation in the region trailing it for all incidence angles tested, as the neighboring flow to its inboard side is stabilized by the slat; see Fig. 15a. Performance degradation begins with the onset of separation on the outboard half of the model. When operated individually, neither the middle nor the outboard segment prevents flow separation for more than 1 deg beyond the original α_{max} . Combined with the inboard actuator set, the middle segment achieves reattachment in the region trailing it, as the flow neighboring it in its inboard side is already stabilized by the inner segment, as is apparent from Fig. 15b. The outboard actuator operated in combination with the inboard segment, as shown in Fig. 15c; however, it is incapable of providing sufficient control authority to keep the flow on its wing section attached. The destabilizing effect of the large regions of separated flow neighboring the segment on either side dominates the flowfield in the vicinity of the outboard actuator row, so that reattaching the flow was not possible for any local momentum coefficient tested. In tuft flow visualization, the effect of the outboard segment is just visible; thus, most of the performance benefit is attributed to the controlling effect of the inboard segment in this case. Hence, the only beneficial combination here is that of segments S1 and S2. In the drag-optimized configuration, the saved momentum from the outboard actuator is distributed equally in the two remaining segments. The local velocity ratio increases from $u_{jet}/u_{\infty} = 3.5$ to $u_{jet}/u_{\infty} = 4.0$, which is sufficient to delay separation, trailing the inboard segment by an additional degree. Therefore, in terms of the optimal use of introduced momentum, employing only two segments

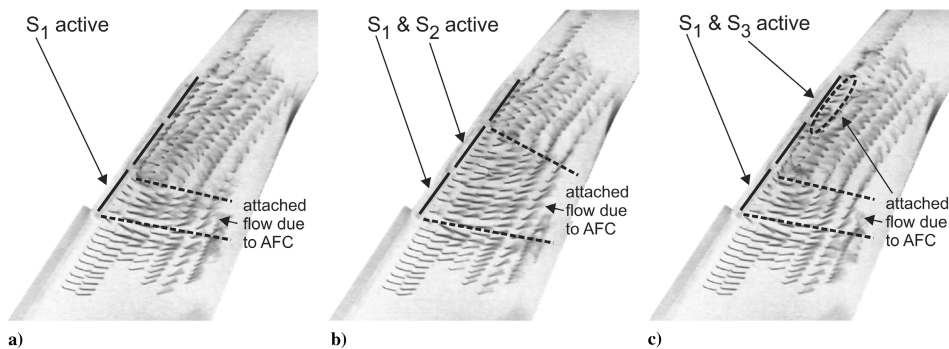


Fig. 15 Tuft visualization of the controlled flow for $\alpha_{max, base} + 3$ deg and different distributions of actuation amplitude.

Case	$\frac{C_{D,AFC} - C_{D,base}}{C_{D,base}}$ [%]						$\frac{(C_L/C_D)_{AFC} - (C_L/C_D)_{base}}{(C_L/C_D)_{base}}$ [%]						
	AOA	$\alpha_{max} - 1^\circ$	α_{max}	$\alpha_{max} + 1^\circ$	$\alpha_{max} + 2^\circ$	$\alpha_{max} + 3^\circ$	$\alpha_{max} + 4^\circ$	$\alpha_{max} - 1^\circ$	α_{max}	$\alpha_{max} + 1^\circ$	$\alpha_{max} + 2^\circ$	$\alpha_{max} + 3^\circ$	$\alpha_{max} + 4^\circ$
	$c_{\mu} = 0.15\%$ (1.4 / 1.5 / 2.3)	-4	6	-6	7	-32	50	-31	46	-4	2	-3	3
$c_{\mu} = 0.44\%$ (2.9 / 2.9 / 2.9)	-5	10	-8	12	-35	62	-37	68	-39	75	-13	19	
$c_{\mu} = 0.62\%$ (3.5 / 3.5 / 3.4)	-5	12	-9	15	-36	65	-38	72	-41	83	-13	22	
$c_{\mu} = 0.60\%$ (4.0 / 4.1 / 0)	-4	8	-7	12	-34	60	-36	66	-38	74	-32	58	
$c_{\mu} = 0.83\%$ (4.1 / 4.1 / 4.0)	-5	13	-9	16	-35	65	-38	74	-40	84	-40	78	

Fig. 16 Effect of flow control efforts on drag reduction and aerodynamic efficiency improvement. (AOA denotes angle of attack.)

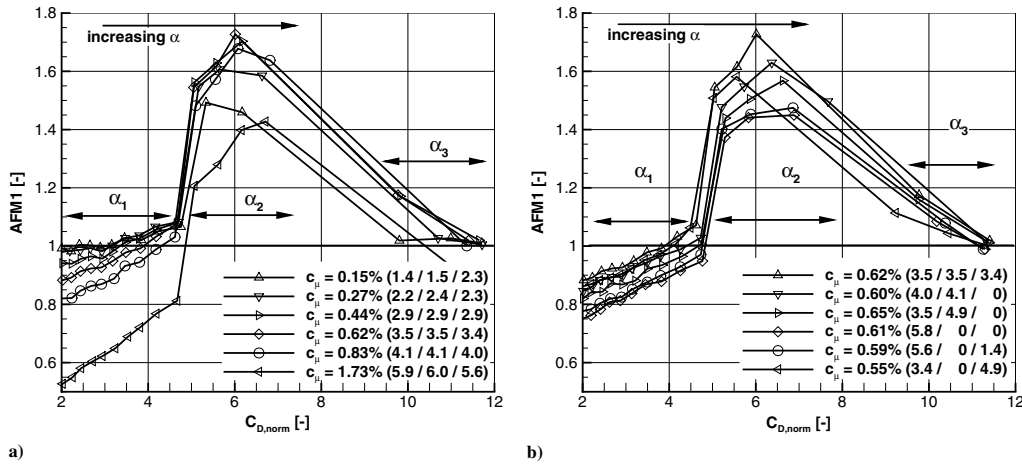


Fig. 17 Representation of AFM1 for a) spanwise invariant and b) spanwise distributed actuation intensity.

with higher forcing amplitudes is superior to operating all actuators at a lower jet velocity ratio. To reach a similar benefit in drag and aerodynamic efficiency, equally distributed actuation requires a total momentum coefficient of $c_{\mu} \approx 0.83\%$ (cf. Fig. 9b). However, to quantify reliably and in depth the gain of distributed actuation, it is necessary to increase the angular resolution. This is envisaged for a future wind-tunnel test campaign.

Concluding the section on flow control results, we present an overview of its effect in Fig. 16. Drag reduction and a gain in aerodynamic efficiency are given in explicit numbers for different angles of attack and parameter combinations previously presented.

C. Consideration of Active Flow Control Efficiency

Following the description of the flow control effect on aerodynamic performance, we want to direct our focus to the efficiency of our flow control approach. To quantify this, we employ the first aerodynamic figure of merit (AFM1), as introduced by Seifert [17]. It is defined as

$$AFM1 = \frac{u_{\infty} L / (u_{\infty} D + P_{AFC})}{(L/D)_{baseline}} \quad (1)$$

L and D are the integral (balance-measured) values of lift and drag, respectively; and P_{AFC} refers to the actuator power consumption. The ratio in the denominator with the subscript of baseline is the value for the uncontrolled flow. The jet power P_{jet} of the AFC system is calculated, based on the same assumptions as for the calculation of the momentum coefficient, from the peak jet velocity and measured mass flow rate. This value is modified by a loss factor ξ_{AFC} that describes the actuator internal energy conversion efficiency to arrive

at the flow control system power consumption $P_{AFC} = \xi_{AFC} \cdot P_{jet}$. To portray the efficiency of a more realistic actuator system, the value for the loss factor is estimated to be $\xi_{AFC} = 0.5$, which is considered to be a conservative assumption based on previous work with this type of actuator system, as reported, e.g., in [18]. The actual energy supplied to the model AFC system was not recorded, as this value would be misrepresentative due to the design compromises necessary to fit the actuators into the model at wind-tunnel scale.** The AFM1 is plotted in Fig. 17 for two of the AFC parameter sets previously presented. For low angles of attack (α_1 range), the flow is attached naturally, and it is inefficient to employ forcing, as indicated by AFM1 values of close to or even less than unity, because the aerodynamic gain is minimal while energy is invested into the flow. The AFM1 reaches values significantly larger than unity (implying efficient use of energy) in the range of angles of attack (α_2 range) where the flow is kept attached only due to flow control. The efficiency is highest for the respective angles of attack, which correspond to the angle of maximum (controlled) lift, and it drops to AFM1 values of approximately unity or below once the flow separates from the wing model, despite the AFC effort (α_3 range).

IV. Conclusions

Active flow control experiments were conducted on a highly three-dimensional modern civil aircraft outer wing configuration provided by the European aeronautical industry, aiming at improving this model's aerodynamic performance at high angles of attack. The

**Note that, for the data shown, an energy conversion efficiency as low as $\xi_{AFC} = 0.1$ would still produce AFM1 values of larger than unity.

capability of pulsed jet actuation to reduce drag and to enhance the aerodynamic efficiency of a wing segment is demonstrated. It is shown that, by choosing adequate parameters of control, it is possible to offset performance degradation by up to 4 deg. For a moderate momentum coefficient of $c_{\mu} \approx 0.62\%$ invested, drag on the wing segment is reduced by more than 40% and the aerodynamic efficiency therefore increases by over 80%. Although the controlled flow cases exhibit higher maximum lift coefficients, this increase is secondary to drag reduction with respect to aerodynamic efficiency, as the ratio of C_D/C_L is dominated by the drag increase due to separation. For a given (sufficiently high) total momentum coefficient, it is found that the local distribution of the momentum introduced (namely, forcing concentrated on the inboard section of the model) is beneficial in terms of actuation efficiency.

Acknowledgments

This work was supported by the German Federal Ministry for Economics and Technology (BMWi) through funding of the German National project Federal research programme aeronautics IV–MOVable dEsign and Optimisation of performance and low Noise (LuFo IV MOVE.ON). The authors would like to acknowledge the help of Airbus Germany (A-D) and the DLR, German Aerospace Center (DLR). We would like to thank Jochen Wild (DLR) and Vlad Ciobaca (DLR) for fruitful discussions and their support.

References

- [1] Ciobaca, V., and Wild, J., "Active Flow Control for an Outer Wing Model of a Take-Off Transport Aircraft Configuration—A Numerical Study," *32nd AIAA Applied Aerodynamics Conference*, AIAA Paper 2014-2403, 2014.
- [2] Haines, A., "Scale Effects on Aircraft and Weapon Aerodynamics," AGARD AGARDograph 323, 1994.
- [3] Ciobaca, V., Melber-Wilkending, S., Wichmann, G., Bergmann, A., and Kuepper, A., "Experimental and Numerical Studies of the Low Speed Wind Tunnel DNW-NWB's Open Test Section Towards an Aeroacoustic Facility," *33rd AIAA Aeroacoustics Conference*, AIAA Paper 2012-2174, 2012.
- [4] "Airworthiness Standards: Transport Category Airplanes," *Aeronautics and Space*, U.S. Code of Federal Regulations 14, Part 25, 2011.
- [5] Butter, D. J., "Recent Progress on Development and Understanding of High Lift Systems," *AGARD Conference on Improvement of Aerodynamic Performance Through Boundary Layer Control and High Lift Systems*, AGARD CP-365, 1984, pp. 1.1–1.26.
- [6] Melton, L., Schaeffler, N., Yao, C., and Seifert, A., "Active Control of Flow Separation from Supercritical Airfoil Leading-Edge Flap Shoulder," *Journal of Aircraft*, Vol. 42, No. 5, 2005, pp. 1142–1149. doi:10.2514/1.10294
- [7] Scholz, P., Casper, M., Ortmanns, J., Kaehler, C., and Radespiel, R., "Leading-Edge Separation Control by Means of Pulsed Vortex Generator Jets," *AIAA Journal*, Vol. 46, No. 4, April 2008, pp. 837–846. doi:10.2514/1.26176
- [8] Kelley, C., Bowles, P., Cooney, J., He, C., and Corke, T., "High Mach Number Leading-Edge Flow Separation Control Using AC DBD Plasma Actuators," *50th AIAA Aerospace Sciences Meeting*, AIAA Paper 2012-0906, 2012.
- [9] Bauer, M., Lohse, J., Hauke, F., and Nitsche, W., "High-Lift Performance Investigation of a Two-Element Configuration with a Two-Stage Actuator System," *AIAA Journal*, Vol. 52, No. 6, 2014, pp. 1307–1313. doi:10.2514/1.J052639
- [10] Lengers, M., "Industrial Assessment of Overall Aircraft Driven Local Active Flow Control," *ICAS Proceedings: 29th Congress of the International Council of the Aeronautical Sciences*, ICAS Paper ICAS2014-1.1.1_0175, 2014.
- [11] Seifert, A., Bachar, T., Koss, D., Shepshelovich, M., and Wagnanski, I., "Oscillatory Blowing: A Tool to Delay Boundary-Layer Separation," *AIAA Journal*, Vol. 31, No. 11, 1993, pp. 2052–2060. doi:10.2514/3.49121
- [12] Kirshner, J. M., *Fluid Amplifiers*, McGraw-Hill, New York, 1966.
- [13] Seele, R., Graff, E., Gharib, M., Taubert, L., Lin, J., and Wagnanski, I., "Improving Rudder Effectiveness with Sweeping Jet Actuators," *6th AIAA Flow Control Conference*, AIAA Paper 2012-3244, 2012.
- [14] Seele, R., Graff, E., Lin, J., and Wagnanski, I., "Performance Enhancement of a Vertical Tail Model with Sweeping Jet Actuators," *51st AIAA Aerospace Sciences Meeting*, AIAA Paper 2013-0411, 2013.
- [15] Greenblatt, D., and Wagnanski, I. J., "The Control of Flow Separation by Periodic Excitation," *Progress in Aerospace Sciences*, Vol. 36, No. 7, 2000, pp. 487–545. doi:10.1016/S0376-0421(00)00008-7
- [16] Horton, B. M., U.S. Patent for "Fluid-Operated System" Publ. No. US3122165-A, filed 19 Sept. 1960, Feb. 1964.
- [17] Seifert, A., "Closed-loop Active Flow Control Systems: Actuators," *Active Flow Control*, edited by King, R., Vol. 95, Notes on Numerical Fluid Mechanics and Multidisciplinary Design, Springer, New York, 2007, pp. 85–102.
- [18] Meyer, M., Machunze, W., and Bauer, M., "Towards the Industrial Application of Active Flow Control in Civil Aircraft—An Active Highlift Flap," *32nd AIAA Applied Aerodynamics Conference*, AIAA Paper 2014-2401, 2014.

F. Coton
Associate Editor

2.3 Bauer2015a

Bauer, M., Grund, T., Nitsche, W., and Ciobaca, V.,
Wing Tip Drag Reduction at Nominal Take-Off Mach Number,
submitted for publication to the AIAA Journal on 14th Feb. 2015

Wing Tip Drag Reduction at Nominal Take-Off Mach Number

Matthias Bauer*, Thomas Grund †, and Wolfgang Nitsche ‡

*Technische Universitaet Berlin
10587 Berlin, Germany*

and

Vlad Ciobaca§

*Deutsches Zentrum fuer Luft- und Raumfahrt e.V. (DLR)
38108 Braunschweig, Germany*

This paper discusses wind tunnel test results aimed at advancing active flow control technology to increase the aerodynamic efficiency of an aircraft during take-off. A model of the outer section of a representative civil airliner wing was equipped with two-stage fluidic actuators between the slat edge and wing tip, where mechanical high-lift devices fail to integrate. The experiments were conducted at a nominal take-off Mach number of $M = 0.2$. At this incidence velocity, separation on the wing section, accompanied by increased drag, is triggered by the strong slat edge vortex at high angles of attack. On the basis of global force measurements and local static pressure data, the effect of pulsed blowing on the complex flow is evaluated, considering various momentum coefficients and spanwise distributions of the actuation effort. It is shown that through local intensification of forcing, a momentum coefficient of less than $c_\mu = 0.6\%$ suffices to offset the stall by 2.4° , increase the maximum lift by more than 10% , and reduce the drag by 37% compared to the uncontrolled flow.

Nomenclature

α	[deg]	= angle of attack
c_p	[-]	= pressure coefficient
$C_{L,norm}$	[-]	= normalized lift coefficient $C_{L,norm} = \frac{C_L}{C_{L,max,base}}$
$C_{D,norm}$	[-]	= normalized drag coefficient $C_{D,norm} = \frac{C_D}{C_{D,min,base}}$
$AFM1$	[-]	= first aerodynamic figure of merit
c_{ref}	[m]	= reference chord length
b	[m]	= span
u_∞	[m/s]	= freestream velocity
$u_{jet,peak}$	[m/s]	= peak jet velocity $u_{jet,peak} = \frac{\dot{m}}{\rho_{jet} A_{AFC}}$
$u_{jet,RMS}$	[m/s]	= root mean square value of $u_{jet,peak}$
f	[Hz]	= forcing frequency
\dot{m}	[kg/s]	= total mass flow rate
ρ_{jet}	[kg/m ³]	= density of air jet at outlet
A_{ref}	[m ²]	= reference area for aerodynamic coefficients
A_{AFC}	[m ²]	= total area of active outlets
c_μ	[-]	= momentum coefficient $c_\mu = \frac{\dot{m} \cdot u_{jet,RMS}}{q_\infty \cdot A_{ref}}$
F^+	[-]	= normalized forcing frequency $F^+ = \frac{f \cdot c_{ref}}{u_\infty}$
x	[m]	= streamwise direction
y	[m]	= (spanwise) direction normal to tunnel floor
z	[m]	= direction normal to tunnel side wall

*Research Scientist, Department of Aeronautics and Astronautics, matthias.bauer@ilr.tu-berlin.de

†Professor, Department of Aeronautics and Astronautics, thomas.grund@ilr.tu-berlin.de

‡Professor, Department of Aeronautics and Astronautics, wolfgang.nitsche@ilr.tu-berlin.de

§PhD Research Scientist, Institute of Aerodynamics and Flow Technology, Vlad.Ciobaca@dlr.de

I. Introduction

The design of wing tip devices on civil airliners has changed remarkably in past decades. The conception of wing tip devices dates back more than a century, with the first functioning design patented in 1915 [1]^a. However, it was not until the research of Whitcomb [2] 60 years later, triggered by an energy crisis that resulted in the need for better fuel performance, that wing tip devices found their way into practice. Winglets (and all derivatives thereof) are designed to minimize the drag during cruise flight. This approach conflicts with performance requirements during low-speed flight when a high-lift system is needed, as the slender shape and high local curvature of modern wing tip devices inhibit the integration of a slat, resulting in early separation at the wing tip at high angles of attack. This optimization conflict might be resolved by active flow control (AFC), as this technology has the potential to augment the overall high-lift system to prevent flow separation where the integration of mechanical devices fails. The suppression of local flow separation is most relevant during the second segment of climb^b, when the landing gear is retracted and a minimum gradient of climb is prescribed even with one engine inoperative. In [3], the climb gradient $\tan(\gamma)$ is defined as a function of the available thrust (T), aircraft weight (W), and aerodynamic efficiency, which is the ratio of the lift (L) and drag (D):

$$\tan(\gamma) = \frac{T}{W} - \frac{1}{(L/D)}$$

. Increasing the lift-to-drag ratio ($\frac{L}{D}$) by local flow control would make it possible to reduce the installed thrust (use smaller engines) or to increase the maximum take-off weight (realize higher passenger capacity).

In this paper, we report the results of wind tunnel experiments conducted on a realistic outer wing model at the nominal take-off Mach number of $M = 0.2$, with local flow control applied between the outer slat edge and wing tip. Pulsed blowing is employed to increase the wing model's aerodynamic efficiency by offsetting the increase in drag. The feasibility of preventing separation at the leading edge by AFC was demonstrated successfully in recent studies [4–9], which focused primarily on increasing the maximum lift and stall angle of slatless single- or multi-element airfoils. Research on localized flow control has also appeared in a multidisciplinary study from the aeronautical industry [10]. Most researchers resort to unsteady excitation of the flow, as this was found to be more efficient than, e.g., steady blowing [11]. Our flow control system relies on fluid amplifier components, which were first studied at the Harry Diamond Laboratories in the early 1960s [12] and have resurfaced in the form of flow control actuators in recent years, as their robustness and

simplicity make them a candidate technology for transfer into industry applications. A review of different types of fluid amplifiers and their application for flow control is given in [13]. Impressive results were obtained using this actuator type, e.g., in experiments to improve the rudder effectiveness of a full-scale vertical tail plane [14, 15] and in studies to reduce the drag on an axis-symmetric bluff-body model [16].

In this paper, we study the effect of the spanwise distribution of the actuation and investigate the effect of the momentum coefficient and jet velocity ratio on the aerodynamic performance of the outer wing model. Localized changes in the model's wake flow field are analyzed using five-hole probe data gathered downstream of the model, and the net benefit of controlling the flow is quantified in terms of the first aerodynamic figure of merit. We show that with a suitable combination of control parameters, we can reduce the drag at the maximum angle of attack by 37% compared to the baseflow value while increasing the maximum lift by more than 10%.

II. Experimental setup

This section describes the wind tunnel model, including the fluidic actuator system, and specifies the experimental uncertainty.

A. Wind tunnel model and instrumentation

The experiments were conducted on the model of an outer wing section representative of a modern civil aircraft (see fig. 1), similar to the one used in [17]. The inner part of the model ($y/b < 0.37$) is equipped with a leading edge slat and an aileron deflected to the take-off configuration. Adjacent to this, a highly three-dimensional wing tip device optimized for cruise flight is mounted. This part of the wing model is not protected by a slat. The model measures approximately 1400 mm from wind tunnel floor to wing tip. A peniche (164 mm in height) and a splitter plate, which are employed to reduce the effect of the wind tunnel floor boundary layer and which are not connected to the balance system, reduce the effective span b of the model to 1250 mm. The test campaign was conducted in the atmospheric large low-speed wind tunnel facility of DNW-NWB^c (German-Dutch Wind Tunnels, Low-Speed Wind Tunnel, Braunschweig) in a 3.25 m × 2.8 m × 8.0 m closed test section. The investigations were performed at a typical take-off Mach number of $M = 0.2$. The resulting Reynolds number based on the model's reference chord length c_{ref} of 490 mm is $Re \approx 2 \times 10^6$. The forces and moments acting on the model were measured using a six-component balance system mounted beneath the wind tunnel floor. Rotating the balance with the model made it possible to vary the incidence angle. Static pressure data were acquired in six chordwise and three spanwise

^aW.E. Somerville described a "Flying-machine" with wings of which "... the extreme end [is] curved upward."

^bCf. FAR Part 25

^cData available online at <http://www.dnw.aero/Wind-tunnels/NWB.aspx>, [retrieved 2014]

sections totaling more than 150 pressure taps. Tufts in combination with high-resolution cameras were used to monitor the surface flow on the suction side of the model wing. The topology of the model wake was measured with a traversable five-hole probe rake positioned at a constant x position downstream of the swept model, which results in a locally variable downstream distance from the trailing edge between $0.5c_{ref}$ and $1.5c_{ref}$. The rake consists of 18 equidistant probes. The flow field investigated spans $0.15 < y/b < 0.85$ in the y direction and is $\Delta z/b = 0.4$ wide. The spatial resolution of the datapoints is 15 mm in both directions.

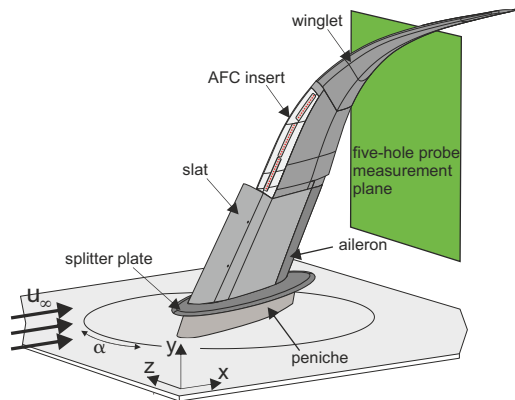


Figure 1. Sketch of wind tunnel model analogous to [17]

B. Active flow control system

The flow control system (see fig. 2) is located between $y/b = 40%$ and $y/b = 75%$ of the model's span. Its design is based on experience from numerical and experimental studies on a similar geometry [17, 18]. A total of 28 rectangular slots are integrated parallel to the leading edge at $x/c_{ref} \approx 5%$ on the suction-side surface. Each slot measures 12.4 mm in the spanwise direction and 0.88 mm in the chordwise direction. The gap between two neighboring outlets is approximately 3.1 mm. Through those slots, compressed air is ejected periodically. The air jets are tilted by 30° relative to the model's surface. The outlets are grouped in three segments with a design-related spacing of 15 mm between them.

The pulsed air jets required for the flow control approach pursued in this paper are generated using fluidic elements based on the principle of fluid amplification. Those devices make it possible to switch the primary jet between two stable states by applying a much weaker (in terms of lower momentum and mass flow rate) control jet. The flow control system employed here follows the two-stage approach presented in [9] and consists of a fluidic oscillator acting as the driving stage and an array of five (segments S1 and S2) or four (segment S3) fluidic diverter elements acting as the outlet stage. Within the driving stage,

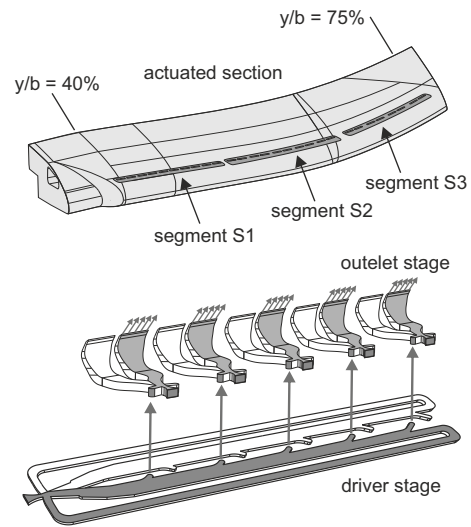


Figure 2. Sketch of the AFC system

a feedback mechanism causes the flow to switch periodically between two branches when fluid passes through it. Each branch has outlets connected to the second stages' control ports, providing this stage with the required control signal. In turn, this pneumatic control signal switches the flow in the second stage between the two corresponding outlets of one diverter element. This results in a pulsed jet flow in which neighboring air jets have a phase shift of 180° . As switching between the outlets of one diverter is induced by the mass flow that propagates through the branches of the control stages, there is a phase lag in switching between two neighboring actuator elements in one segment. The air pressure supply for each segment's first and second stages is controlled independently by a pressure regulator valve, allowing different forcing amplitudes across the segments and fine-tuning of the actuation frequency. Mass flow meters based on the thermoelectrical principle are used to measure the flow rate of the ejected air for each actuator array. The frequency of actuation was determined using Kulite pressure transducers installed in the AFC system's driving stages during the experiments. The system performance was evaluated before the wind tunnel testing to ensure a sufficiently homogeneous jet velocity distribution along the span. For that purpose, the total pressure along the centerline of each outlet was measured with a Pitot tube connected to a Kulite pressure transducer. The peak total pressure measured at the individual outlets lies within $\pm 2%$ of the average peak value recorded across all outlets. To illustrate the switching quality of the actuators, the time history of the total pressure data recorded at the center of one outlet of segment S1 is provided in fig. 3, demonstrating fully modulated operation. As this flow control system incorporates no moving or electrical components, the switching frequency

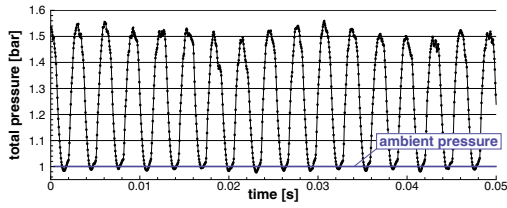


Figure 3. Time history of total pressure data for one outlet of segment S1

depends only on the mass flow rates through the driving and outlet stages and the ratio thereof. An example of a map of this correlation is shown in fig. 4.

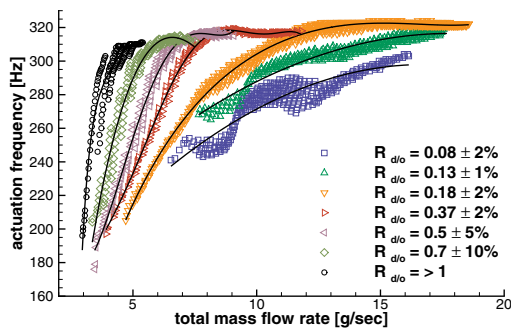


Figure 4. Frequency map for segment S1

All the quoted momentum coefficients are calculated using $c_\mu = \frac{\dot{m} \cdot u_{jet,RMS}}{q_\infty \cdot A_{ref}}$, where $u_{jet,RMS}$ is the RMS value of the peak jet velocity. Assuming a uniform velocity profile (plug flow) across the outlet and the form of a square wave signal in time, $u_{jet,RMS}$ can be approximated by $u_{jet,RMS} = \frac{1}{2\sqrt{DC}} u_{jet,peak}$. The duty cycle (DC) describes the fraction of time one outlet is active during one switching cycle. It is fixed at 50% (DC = 0.5) in our studies. The peak jet velocity $u_{jet,peak}$ is calculated from the measured mass flow rate (\dot{m}), the area of the active actuator outlets (A_{AFC}), and the density of the fluid at the outlets (ρ_{jet}), using $u_{jet,peak} = \frac{\dot{m}}{\rho_{jet} A_{AFC}}$. The jet densities for different mass flow rates were established in bench-top experiments. A more detailed description of the c_μ calculation is found in [17]. When multiple segments were active, the c_μ value quoted is the sum of the values for each active segment.

C. Experimental uncertainty

The uncertainty in measuring forces with the balance system is 0.3% of each of the full scale spans, which are 2000 N for the drag and 8100 N for the lift. This translates to an uncertainty of less than $\Delta C_L \pm 0.007$ in the lift coefficient and of less than $\Delta C_D \pm 0.002$ in the drag coefficient. The maximum expected error in measuring the pressure

is 0.1% of the full span ranges of the pressure transducers, which are 5 psi and 15 psi for static pressure on the model and 5 psi for the five-hole probe wake rake. The results presented are corrected for wind tunnel effects using the method described in [19]. The momentum coefficient is calculated from the mass flow rate through the outlet slots measured *in situ* during the experiments and the jet density at the outlets, which was determined in bench-top experiments. The deviation of the quoted momentum coefficients from the exact values is determined by the simplifying assumptions regarding the velocity profile in time and space and the measurement error in the mass flow rate and density. This (absolute) uncertainty is difficult to quantify. However, as the uncertainty in the density and velocity profiles produces a systematic error, the relative uncertainty between the various c_μ values quoted is determined only by the uncertainty in measuring the mass flow rate, which is specified as $\pm 1\%$ of the sensors' full scale range. This translates to an uncertainty in c_μ of approximately $\pm 0.01\%$.

III. Results

The major findings of our wind tunnel experiments are presented in this section. We describe the topology and separation behavior of the baseflow and discuss the effects of flow control on the aerodynamic performance of the model wing. All the aerodynamic coefficients are normalized by their respective baseflow values, $C_{D,min,base}$, $C_{L,max,base}$, and $(C_L/C_D)_{max,base}$.

A. Baseflow

Because the model wing is three-dimensional, the baseflow topology is highly complex and dominated by a strong outboard-directed cross-flow component over a wide range of incidence angles. Separation occurs locally at different angles of attack until the slat edge vortex has grown strong enough to induce flow separation in its vicinity, resulting in an almost instantaneous separation of the remaining attached flow on the slatless wing section. In this section, the separation process is described in terms of global force measurements, surface pressure data, and surface tuft flow visualization, in order to revisit these findings later in the light of our flow control attempts.

Fig. 5 shows the lift and drag coefficients for the uncontrolled flow against the angle of attack. The lift increases linearly with increasing incidence angle up to the maximum angle of attack region, where the onset of separation reduces the slope of the lift curve and results in increased drag. For selected angles of attack (marked in fig. 5), the pressure coefficient curves in the spanwise direction are shown in fig. 6. The static pressure taps for which the data are plotted are located at the leading edge at $x/c = 0\%$, which is near the suction peak for the incidence angles shown. The data are normalized with re-

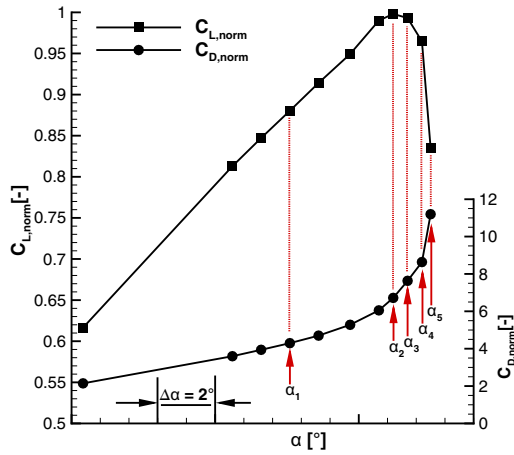


Figure 5. Lift and drag coefficients vs. angle of attack

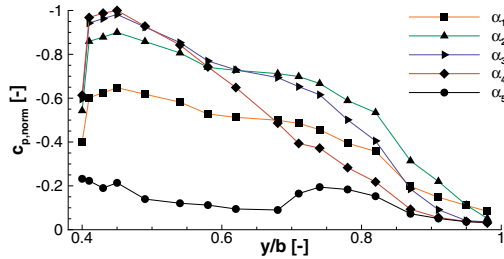


Figure 6. Pressure coefficient curve in spanwise direction for various incidence angles

spect to the magnitude of the lowest recorded c_p value. From these data, it is apparent that flow separation progresses from wing tip to wing root with increasing incidence. At a sufficiently low angle of attack (α_1), a suction peak manifests along the entire span, indicating attached flow. For increasing incidence ($\alpha_1 \rightarrow \alpha_4$), the magnitude of the c_p values increases continuously in the portion of the span where there is attached flow. The static pressure on the surface is lowest downstream of the slat edge at $y/b \approx 0.45$. Concurrently, the fraction of the span where the flow separates at the leading edge and no suction peak is formed progresses inward, from $y/b \approx 0.9$ for α_1 to $y/b \approx 0.7$ for α_4 . A further increase in the incidence angle (α_5) results in an abrupt separation on the entire unslatted (unprotected) section of the model wing, which causes a drop in c_p at all the stations plotted. This is confirmed in the tuft flow visualization presented in fig. 7, which shows the outer part of the wing model from $y/b = 0.66$ to $y/b = 1$. For low incidence (α_1), the tufts indicate attached flow with a significant cross-flow component directed toward the wing tip. Increasing the angle of attack to α_2 results in an even more prominent cross-flow component, a higher unsteadiness of the tufts in the aft region

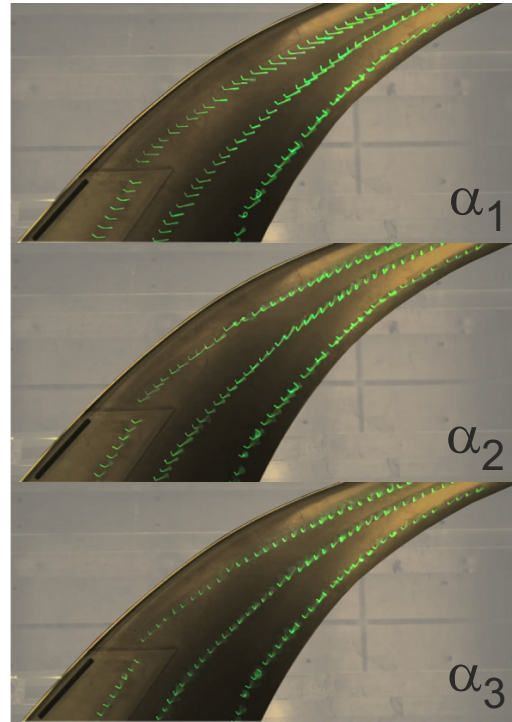


Figure 7. Progression of separation on the outboard section

of the model, and the onset of separation on the wing tip, as indicated by the orientation of the tufts. At α_3 , the flow on the part of the model shown in the figure is mostly separated, and the tufts show highly erratic motion and reversed orientation. At this angle of attack (α_3), which is just beyond α_{max} , the lift force begins to decrease with increasing incidence, but the flow in the region downstream of the slat edge is still attached. There, separation is triggered by the increasing strength of the slat-edge longitudinal vortex, which induces a velocity component directed away from the surface. This mode of separation is relevant, as it is the mechanism that limits the effectiveness of our flow control attempt presented below. Therefore, it is documented in fig. 8, which shows a sequence of consecutive frames (recorded at 50 Hz, $\Delta t = 20$ ms) from the tuft flow visualization video for increasing incidence from α_4 to α_5 . The first frame (t_0) shows attached flow trailing the slat edge. One timestep later ($t_0 + 20$ ms), the tufts begin to detach from the surface in the area of upwash induced by the slat-edge vortex. At $t_0 + 40$ ms, the separation has progressed further inboard, and at $t_0 + 60$ ms, the flow trailing the slat edge is completely separated.

B. Controlled flow

The results for the controlled flow are presented in this section. The performance of AFC will be quantified in

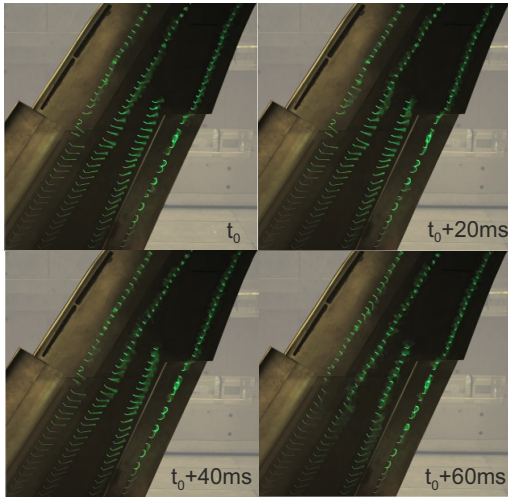


Figure 8. Progression of separation on the inboard section

terms of the gain in the maximum lift, reduction in drag compared to the baseflow at $\alpha(C_{L,max,AFC})$, and offset of the stall angle. A deeper understanding of the changes in the flowfield is gained by analyzing wake measurements conducted with a traversable five-hole probe rake. Finally, the efficiency of this AFC approach is evaluated in terms of the first aerodynamic figure of merit. In addition to the momentum coefficient, the jet velocity ratios $VR = u_{jet,peak}/u_\infty$ are quoted in the figure legend in order from inboard (S1) to outboard (S3), i.e., $(VR_{S1}, VR_{S2}, VR_{S3})$. Although previous experiments on a similar geometry have shown no significant impact of the actuation frequency on the control results, an attempt was made to keep the forcing frequency constant across the actuation amplitude range tested. The frequency band for segments S1 and S2 ranges from $F_{min}^+ = 2.06$ (295 Hz) for $VR = 2.0$ to $F_{max}^+ = 2.2$ (315 Hz) for $VR = 4.5$. Geometric constraints required a shorter feedback structure on segment S3, resulting in a higher frequency band, which ranges from $F_{min}^+ = 2.66$ (380 Hz) for $VR = 2.0$ to $F_{max}^+ = 2.85$ (407 Hz) for $VR = 4.8$.

1. Global Effects of Flow Control

In previous experiments on a similar geometry, we observed that the flow control effectiveness was sensitive to the distribution of actuation along the span. Therefore, the effect of different combinations of segment-wise actuation was evaluated for a constant overall forcing amplitude of $c_\mu \approx 0.6\%$. The resulting drag and lift coefficient curves are presented in figs. 9 and 10, respectively. All the combinations tested improved the stall behavior of the model wing. Although the extent of the improvement differs, the underlying trends are similar. At a sufficiently low incidence (e.g., $\alpha_{max} - 4^\circ$), the effect of flow control

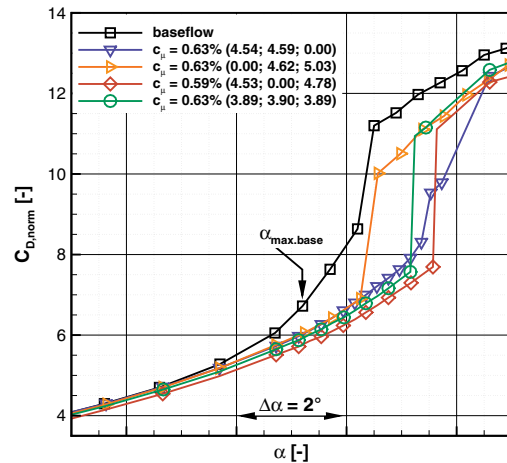


Figure 9. Drag coefficient for forcing with $c_\mu \approx 0.6\%$

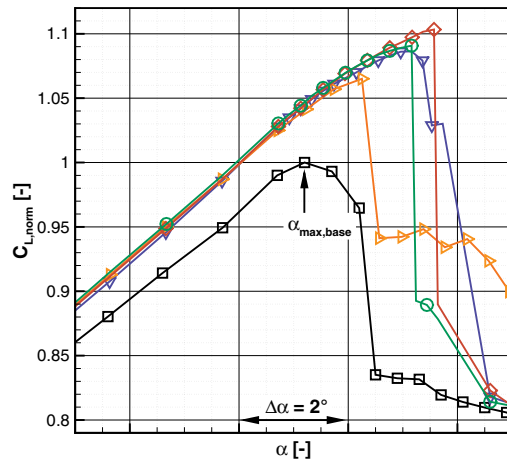


Figure 10. Lift coefficient for forcing with $c_\mu \approx 0.6\%$

on the drag coefficient is negligibly small. In the incidence range between $\alpha_{max,base} - 3^\circ$ and the corresponding $\alpha_{max,AFC}$, the (ideally) parabolic shape of the drag coefficient curve is maintained as a result of forcing. This can be attributed to the reduction in the cross flow on the model and the prevention of separation on the outboard half of the wing. In contrast to the drag, the lift is affected by flow control over the entire range of angles of attack tested. In the linear range of the lift curve, the lift coefficient is offset by a constant ΔC_L depending on the momentum coefficient, but not on the distribution of the actuation along the span. Once stall occurs, the resulting drag rise and lift drop are more abrupt than those for the baseflow. Here, the exception is actuation with segments S1 and S2 combined, for which separation on the model

occurs in two distinct steps. For this combination, the flow on the winglet separates, but the flow stays attached in the region trailing the slat edge for an additional $\Delta\alpha = 0.4^\circ$. This results in an intermediate step in the drag coefficient curve and milder stall behavior.

The difference in effectiveness for the segment combinations tested becomes apparent when the stall angle ($\alpha_{max,AFC}$), maximum lift ($C_{L,max,AFC}$), and drag coefficient value (C_D) at each $\alpha_{max,AFC}$ are considered. According to those indicators, actuation with segments S1 and S3 yields the highest benefit. For a momentum coefficient of $c_\mu = 0.6\%$, forcing with these two segments offsets stall by 2.4° and increases the maximum lift coefficient by more than 10%. The drag coefficient at $\alpha_{max,AFC,S1\&S3}$ is reduced by 37% with respect to the baseflow value.

The aerodynamic efficiency of a wing is given by the

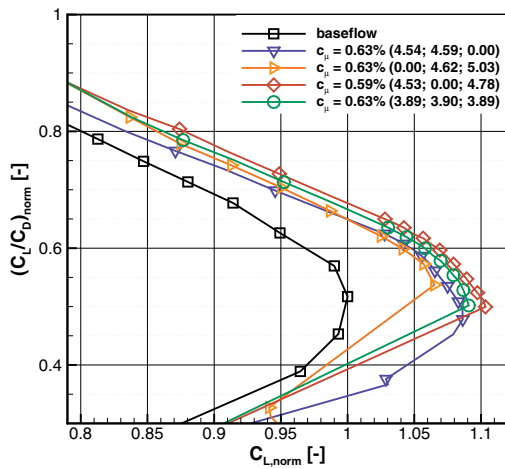


Figure 11. Aerodynamic efficiency vs. lift coefficient for forcing with $c_\mu \approx 0.6\%$

ratio of C_L over C_D , which is plotted versus the lift coefficient in fig. 11 for the segment variation considered above. Again, with respect to this quantity, the combination of segments S1 and S3 produces the best results. The effect of flow control is positive over the entire incidence range. At the original (baseflow) $C_{L,max,base}$, the aerodynamic efficiency is increased by 30%, whereas for maintaining the original aerodynamic efficiency, a lift increase of 9.5% is achievable. Actuation with all other combinations of segments is beneficial as well, but to a lesser extent.

For actuation using the most effective segment combination, segments S1 and S3, the drag and lift coefficient curves for different forcing amplitudes are presented in figs. 12 and 13, respectively. Increasing the forcing amplitude successively improves the aerodynamic performance of the model wing, and no saturation is observed within the available range of momentum coefficients. The highest forcing amplitude of $c_\mu = 0.59\%$ is produced at a jet

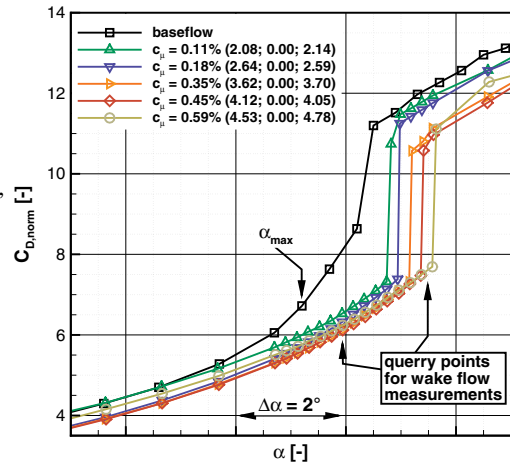


Figure 12. Drag coefficient for forcing with segments 1 and 3 for various c_μ

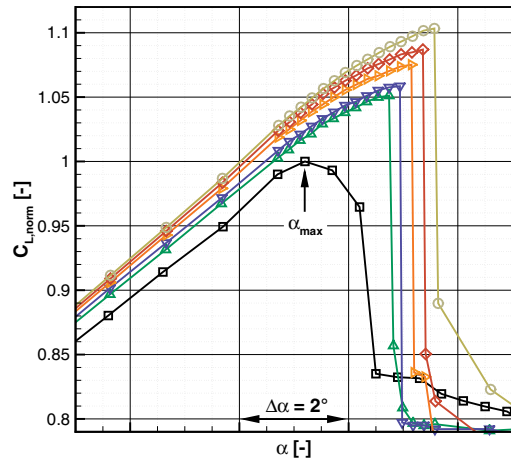


Figure 13. Lift coefficient for forcing with segments 1 and 3 for various c_μ

velocity ratio of approximately 4.7, which implies an almost sonic peak jet exit velocity ($Ma_{jet,peak} \approx 0.95$). Between the lowest ($c_\mu = 0.11\%$) and highest ($c_\mu = 0.59\%$) forcing amplitudes tested, the resulting offset in stall angle ranges from $1.5^\circ < \Delta\alpha_{max,AFC} < 2.4^\circ$, and the maximum lift increases in the range of $5\% < \Delta C_{L,max,AFC} < 10.4\%$. The drag reduction at $\alpha_{max,AFC}$ varies only slightly within the band of forcing amplitudes tested, showing an improvement of approximately 37% compared to the uncontrolled baseflow. An overview of the flow control performance as a function of the momentum coefficient and jet velocity ratio for different combinations of segments is provided in figs. 14–17. Note that only one data point is available for the combination of segments S2 and S3. The

offset in the stall angle is presented in fig. 14 as a function of the momentum coefficient. With respect to the stall

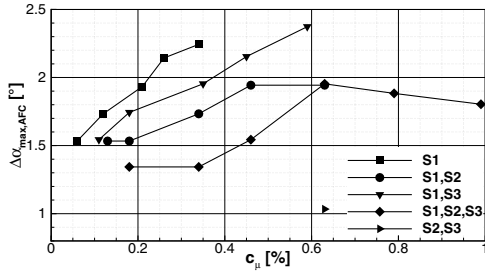


Figure 14. Stall angle offset for different momentum coefficients and segment combinations

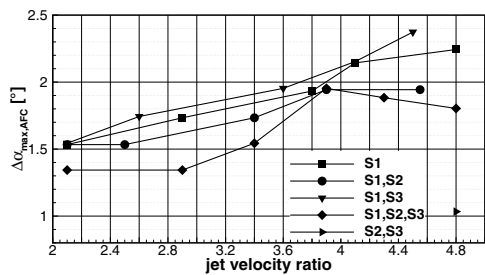


Figure 15. Stall angle offset for different velocity ratios and segment combinations

angle, it is noteworthy that forcing with only segment S1 significantly shifts the onset of stall to higher incidences at relatively low momentum coefficients, offsetting stall by up to $\approx 2.2^\circ$ at a momentum coefficient of $c_\mu = 0.34\%$. In comparison, actuation with segments S1 and S3 can produce a higher maximum shift in α_{max} (additional $\Delta\alpha_{max}$ of 0.25°), but this combination requires almost twice the investment in terms of the momentum coefficient to produce an identical offset in the stall angle. All other combinations of segments increase the stall angle by less than 2° . Plotting $\Delta\alpha_{max,AFC}$ versus the jet velocity ratio (see fig. 15) appears much better suited to collapse the curves shown, indicating that, with respect to the increase in the stall angle, this ratio is the dominant AFC parameter compared to the total momentum or mass addition. For velocity ratios smaller than 4, the curves for the segment combinations (S1), (S1,S2), and (S1,S3) lie within a band of $\Delta\alpha_{max,AFC} \pm 0.1^\circ$ from the average value. The results for forcing with all three segments (S1,S2,S3) lie below this band as a result of the different (two-step) stall behavior described above. For velocity ratios larger than 4, the curves diverge, as forcing combinations that include segment S2 do not lead to additional benefit in terms of a further increase in jet exit velocity. The lift gain as a function of c_μ is presented in fig. 16. Here, an almost linear increase in the lift gain is observed with increasing momentum coefficient. The slope ($d(\Delta C_{L,max})/dc_\mu$) of the curves

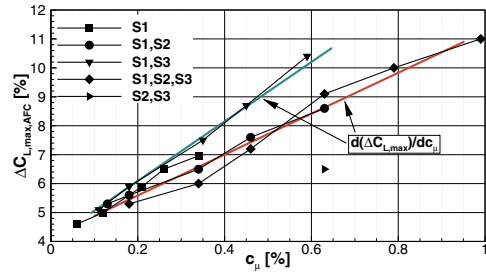


Figure 16. Maximum lift increase for different momentum coefficients and segment combinations

associated with forcing with segment S1 only and with segments S1 and S3 combined is steeper than that for any segment combination that includes forcing with segment S2. The inefficiency of including segment S2 in the control attempt becomes apparent when actuation with segments S1 and S3 is compared to actuation with all three segments. While the maximum increase in $C_{L,max,AFC}$ is marginally higher when all three segments are operated ($\Delta C_{L,max,S1\&S2\&S3} = 11\%$ vs. $\Delta C_{L,max,S1\&S3} = 10.4\%$), the required momentum input in terms of momentum coefficient to achieve a similar lift gain is approximately 40% higher than for actuation with segments S1 and S3 only. Although the offsets in the stall angle and lift gain exhibit a distinct dependence on the momentum coefficient, this is not observed in the reduction of the drag at $\alpha_{max,AFC}$ relative to the respective baseflow values, as shown in fig. 17. Here, the percentage by which the drag coefficient is

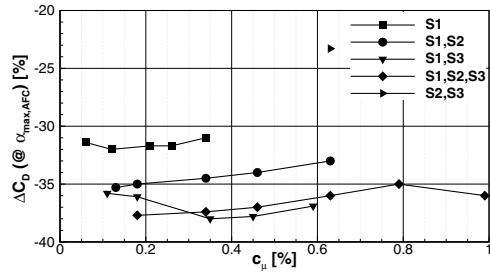


Figure 17. Drag reduction at $\alpha_{max,AFC}$ for different momentum coefficients and segment combinations

reduced is approximately constant across the range of momentum coefficients tested and depends only on the combination of segments operated. The highest drag reduction is realized using the combination of segments S1 and S3 or segments S1, S2, and S3, which decreases the drag coefficient by approximately 37%. Operation of segments S2 and S3 yields the least benefit, resulting in a drag decrease of less than 23%.

To conclude this section on the global effects of flow control, we attempt to explain the counterintuitive observation that the *addition* of local forcing (namely with seg-

ment S2) deteriorates the effectiveness of AFC for otherwise identical forcing parameters. For this purpose, the pressure coefficient distribution along the span (constant $x/c = 0\%$) is displayed in fig. 18 for two different combinations of segments: inner and outer segments (S1,S3; $c_\mu = 0.59\%$) and all three segments (S1,S2,S3; $c_\mu = 0.79\%$), with all segments operated at a velocity ratio of $u_{jet,peak}/u_\infty \approx 4.5$. The incidence angles shown correspond to $\alpha_{max,AFC,S1\&S2}$ (which is 1.7° beyond $\alpha_{max,base}$) and an additional increment of $+0.2^\circ$. Near the active segment S2 (as marked in

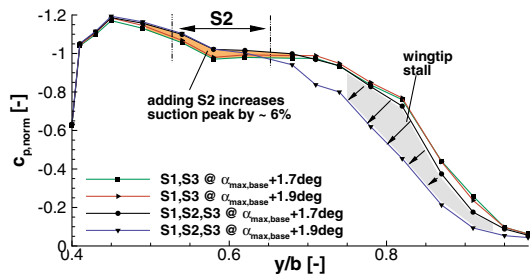


Figure 18. Effect of segment S2 on the normalized pressure coefficient distribution

the figure), we find that the suction peak is 6% larger than when S2 is inactive. This favorably affects the lift coefficient at lower angles of attack. However, the reduced pressure in this region causes increased aerodynamic loading on the model wing in this area, making it more prone to separation. Additionally, this low pressure region causes the jets emanating from the outboard segment S3 to be attracted into this region, directing their effect away from the wing tip, where, in consequence, separation occurs earlier. This observation is confirmed in tuft flow visualization (not shown here).

2. Effect of AFC on Model Wake Flow

A traversable five-hole probe rake was used to quantify the effect of flow control on the wake flow of the outer wing model to gain insight into how the changes are spatially distributed in the flow field. The flow conditions for two incidence angles (marked in fig. 12) are evaluated. The plots show the Mach number (normalized by the incidence Mach number) measured in the plane of the rake together with the vectors for the velocity components in the y and z directions observed from a downstream position looking upstream.

First, the data for an angle of attack of ($\alpha_{max,base} + 0.7^\circ$) are presented, at which a significant drag reduction of more than 20% is noted, although the baseline flow is not fully separated yet. The results for the uncontrolled flow are shown in fig. 19. Here, the most prominent feature is the large vortical structure formed at the wing tip by flow separation. It manifests as a region of low velocity, highly rotational flow motion in the wake field, and low static pressure (not shown here). Flow control can

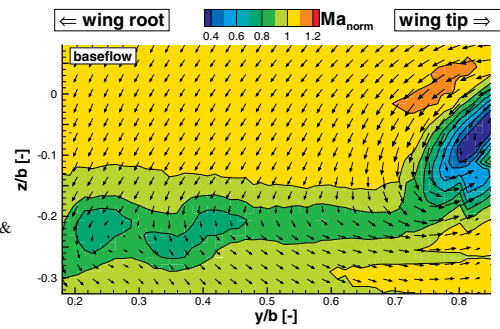


Figure 19. Wake flow at $\alpha_{max,base} + 0.7^\circ$ for the baseflow

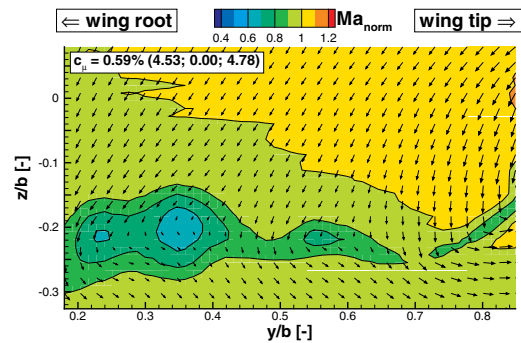
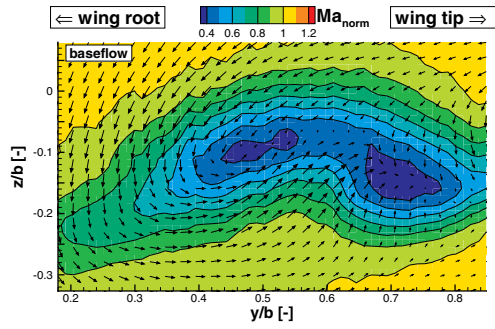
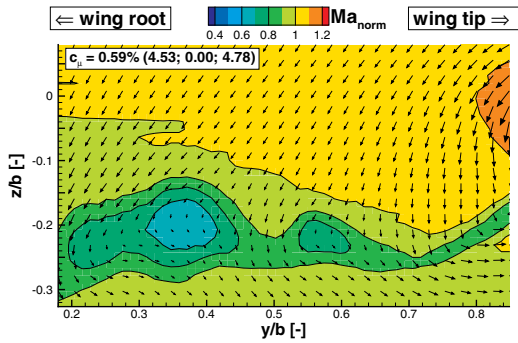


Figure 20. Wake flow at $\alpha_{max,base} + 0.7^\circ$ for the controlled flow

completely suppress the separation on the wing tip, as is apparent from fig. 20. The velocity losses associated with the onset of trailing edge separation on the entire span are reduced, and the slat edge vortex (at $y/b \approx 0.35$) is more defined in the case of controlled flow. Note that the magnitude of the cross-flow component directed outward (positive y direction) is also reduced when forcing is applied. A second set of data is presented for an incidence close to the maximum angle of attack of the controlled flow ($\alpha_{max,AFC,S1\&S3} \approx \alpha_{max,base} + 2.3^\circ$). For the baseflow (see fig. 21), a massive separation is observed downstream of the model where no slat is installed, accompanied by extensive velocity losses (down to 30% of the incidence velocity). The downwash normally produced by the lifting surface is replaced in parts by upwash, reflecting the shedding of vortices at the leading and trailing edges of the wing model.

In comparison, the wake flow measurements for the controlled flow, shown in fig. 22, illustrate the ability of AFC to stabilize the flow on the wing and to suppress separation completely. The large region of high velocity losses is reduced to the size commonly found downstream of the trailing edge of a wing. Now, the highest magnitude of the velocity deficit is found in the center of the slat edge vortex and its associated secondary

Figure 21. Wake flow at $\alpha_{\max,base} + 2.3^\circ$ for the baseflowFigure 22. Wake flow at $\alpha_{\max,base} + 2.3^\circ$ for the controlled flow

vortex (at $y/b \approx 0.35$), and downstream of the location of the (inactive) segment S2. It is noteworthy that the (controlled) flow structure at this high angle of attack closely resembles that shown at lower incidence angles—differing mainly in the size of the slat-edge-induced velocity deficit—although the wing is very close to stall.

3. Consideration of Flow Control Efficiency

To conclude the analysis of the effect of flow control on the aerodynamic performance, we focus on the *efficiency* of our flow control approach. To quantify this, we employ the first aerodynamic figure of merit, as introduced by Seifert [20]. It is defined as

$$AFM1 = \frac{u_\infty L}{(u_\infty D + P_{AFC})} \cdot \frac{(L/D)_{baseline}}{(L/D)_{baseline}}. \quad (1)$$

L and D are the integral (balance-measured) values of the lift and drag, respectively, and P_{AFC} refers to the actuator power consumption. The ratio in the denominator with subscript *baseline* is the value for the uncontrolled flow. The jet power P_{jet} of the AFC system is calculated, under the same assumptions as those for the calculation of the momentum coefficient, from the peak jet velocity

and measured mass flow rate. This value is modified by a loss factor ξ_{AFC} that describes the actuator internal energy conversion efficiency to yield the flow control system power consumption $P_{AFC} = P_{jet}/\xi_{AFC}$. To portray the efficiency of a more realistic actuator system, the value for the loss factor is estimated to be $\xi_{AFC} = 0.5$, which is considered to be a conservative assumption based on previous work with this type of actuator system as reported in, e.g., [21]. The actual energy supplied to the model AFC system was not recorded, as this value would not be representative owing to the design compromises necessary to fit the actuators into the model at wind tunnel scale^d. The AFM1 value for different segment combina-

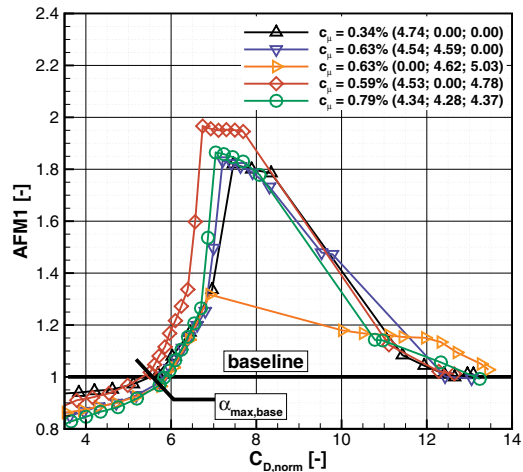


Figure 23. First aerodynamic figure of merit for a constant jet velocity ratio

tions is plotted in fig. 23 for a constant jet velocity ratio of $u_{jet}/u_\infty \approx 4.4$ and in fig. 24 for a constant total momentum coefficient of $c_\mu \approx 0.34\%$. AFM1 values larger than unity reflect efficient use of the energy supplied. Three distinct regimes can be identified. For low drag coefficient values, which correspond to low angles of attack, the flow is attached naturally to the wing, and the lift increase produced at those incidences does not warrant the efficient use of flow control, as indicated by AFM1 values smaller than unity. At incidence angles where the flow is kept attached only because of flow control, all the combinations of segments tested produce AFM1 values larger than unity. The peak values, however, depend largely on the combination of segments chosen. For a similar momentum coefficient and jet velocity ratio, forcing with segments S2 and S3 combined yields $AFM1 \approx 1.3$, whereas the combination of segments S1 and S3 combined produces $AFM1 \approx 1.95$. A comparison of the curves for the combination of S1 and S3 in figs. 23 and 24 shows that lowering the forcing amplitude to a certain degree in-

^dNote that for the data shown, an energy conversion efficiency of approximately 3% would still produce AFM1 values greater than unity.

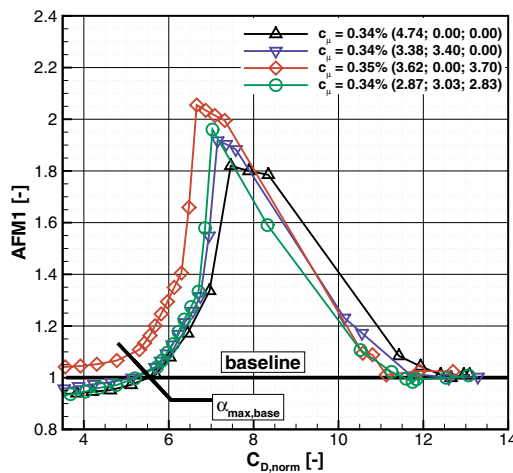


Figure 24. First aerodynamic figure of merit for a constant momentum coefficient

increases the AFM1 value [$AFM1(c_\mu = 0.59\%) \approx 1.95 \Rightarrow AFM1(c_\mu = 0.35\%) \approx 2.05$], indicating a more efficient use of energy, but the effectiveness is reduced. Once the flow separates from the wing, despite the attempt at flow control, the AFM1 values drop to approximately unity.

IV. Conclusion

AFC by means of pulsed air jet blowing was applied to a realistic outer wing model to counter performance degradation at high angles of attack. The experiments were conducted at the nominal take-off incidence Mach number of $M = 0.2$. Although all the forcing parameter variations tested improve the aerodynamic performance, the results reveal that the control effect is highly sensitive to the local distribution of momentum and mass introduction. The most effective set of forcing parameters, actuation with segments S1 and S3 combined using a momentum coefficient of $c_\mu = 0.59\%$, offsets the stall angle by 2.4° , increases the maximum lift by 10.5% , and decreases the drag at $\alpha_{max,AFC}$ by 37% . The application of flow control was found to change the stall behavior of the model wing. As the baseflow separates gradually from the wing, with separation progressing from outboard to inboard with increasing incidence, stall occurs abruptly on the entire model under controlled flow. The actuation efficiency, measured in terms of the first aerodynamic figure of merit, improves significantly if the actuation effort is distributed advantageously along the span.

Acknowledgments

The work was supported by the German federal Ministry for Economics and Technology (BMWi) through funding of the German national project LuFo IV MOVE.ON.

References

- [1] Somerville, W., "Flying-Machine." Sept. 21 1915, US Patent 1,154,214.
- [2] Whitcomb, R. T., "A Design Approach and Selected Wind Tunnel Results at High Subsonic Speeds for Wing-Tip Mounted Winglets," Tech. Rep. NASA-TN-D-8260, NASA Langley Research Center, 1976.
- [3] Butter, D. J., "Recent Progress on Development and Understanding of High Lift Systems," *AGARD Conference on Improvement of Aerodynamic Performance Through Boundary Layer Control and High Lift Systems*, No. AGARD-CP-365, 1984, pp. 1.1–1.26.
- [4] Melton, L., Schaeffler, N., Yao, C., and Seifert, A., "Active Control of Flow Separation from Supercritical Airfoil Leading-Edge Flap Shoulder," *Journal of Aircraft*, Vol. 42, No. 5, 2005, pp. 1142–1149.
- [5] Khodadoust, A. and Washburn, A., "Active Control of Flow Separation on a High-Lift System with Slotted Flap at high Reynolds Number," *25th AIAA Applied Aerodynamics Conference, Miami, FL*, No. AIAA 2007-4424, 2007.
- [6] Casper, M., Scholz, P., Radespiel, R., Wild, J., and Ciobaca, V., "Separation Control on a High-Lift Airfoil using Vortex Generator Jets at High Reynolds numbers," *41st AIAA Fluid Dynamics Conference and Exhibit, Honolulu, Hawaii*, No. AIAA 2011-3442, 2011.
- [7] Kelley, C., Bowles, P., Cooney, J., He, C., and Corke, T., "High Mach Number Leading-Edge Flow Separation Control Using AC DBD Plasma Actuators," *50th AIAA Aerospace Sciences Meeting, Nashville, Tennessee*, No. AIAA 2012-0906, 2012.
- [8] Brunet, V., Dandois, J., and Verbeke, C., "Recent On-era Flow Control Research on High-Lift Configurations," *AerospaceLab Journal*, Vol. 6, No. AL06-05, June 2013.
- [9] Bauer, M., Lohse, J., Haucke, F., and Nitsche, W., "High-Lift Performance Investigation of a Two-Element Configuration with a Two-Stage Actuator System," *AIAA Journal*, Vol. 52, No. 6, 2014, pp. 1307–1313.
- [10] Lengers, M., "Industrial Assessment of Overall Aircraft Driven Local Active Flow Control," *ICAS Proceedings: 29th Congress of the International Council of the Aeronautical Sciences, St. Petersburg, Russia*, No. Paper 1.1.1, 2014.
- [11] Seifert, A., Bachar, T., Koss, D., Shepshelovich, M., and Wagnanski, I., "Oscillatory Blowing: A Tool to Delay Boundary-Layer Separation," *AIAA Journal*, Vol. 31, No. 11, 1993, pp. 2052–2060.
- [12] Horton, B., "Fluid-Operated System," Feb. 25 1964, US Patent 3,122,165.
- [13] Gregory, J. and Tomac, M. N., "A Review of Fluidic Oscillator Development," *43rd Fluid Dynamics Conference, San Diego, CA*, No. AIAA 2013-2474, American Institute of Aeronautics and Astronautics, 2013.
- [14] Whalen, E. A., Lacy, D. S., Lin, J. C., Andino, M. Y., Washburn, A. E., Graff, E. C., and Wagnanski, I. J., "Performance Enhancement of a Full-Scale Vertical Tail Model Equipped with Active Flow Control," *53rd*

- AIAA Aerospace Sciences Meeting*, No. AIAA 2015-0784, American Institute of Aeronautics and Astronautics, 2015.
- [15] Andino, M. Y., Lin, J. C., Washburn, A. E., Whalen, E. A., Graff, E. C., and Wygnanski, I. J., “Flow Separation Control on a Full-Scale Vertical Tail Model using Sweeping Jet Actuators,” *53rd AIAA Aerospace Sciences Meeting*, No. AIAA 2015-0785, American Institute of Aeronautics and Astronautics, 2015.
- [16] Schatzman, D., Wilson, J., Arad, E., Seifert, A., and Shtendel, T., “Drag-Reduction Mechanisms of Suction-and-Oscillatory-Blowing Flow Control,” *AIAA Journal*, Vol. 52, No. 11, Sept. 2014, pp. 2491–2505.
- [17] Bauer, M., Grund, T., and Nitsche, W., “Experiments on Active Drag Reduction on a Complex Outer Wing Model,” *AIAA Journal*, , No. <http://dx.doi.org/10.2514/1.J053515>, Dec. 2014, pp. 1–10.
- [18] Ciobaca, V. and Wild, J., “Active Flow Control for an Outer Wing Model of a Take-off Transport Aircraft Configuration - A Numerical Study,” *32nd AIAA Applied Aerodynamics Conference*, No. AIAA 2014-2403, 2014.
- [19] Ewald, B. E., “Wind Tunnel Wall Correction,” Tech. Rep. AGARD-AG-336, AGARD, 1998.
- [20] Seifert, A., “Closed-Loop Active Flow Control Systems: Actuators,” *Active Flow Control*, edited by R. King, Vol. 95 of *Notes on Numerical Fluid Mechanics and Multidisciplinary Design*, Springer, 2007, pp. 85–102.
- [21] Meyer, M., Machunze, W., and Bauer, M., “Towards the Industrial Application of Active Flow Control in Civil Aircraft - An Active Highlift Flap,” *32nd AIAA Applied Aerodynamics Conference*, No. AIAA 2014-2401, 2014.

3 Methodology and discussion of results

This chapter will provide an overview of the methodology used for the research work completed and will summarize and discuss the results from the individual publications presented in chapter 2 in a comprehensive manner.

3.1 Summary of methodology

This section summarizes the methodology employed, detailing the actuation concept, the experimental setup including wind tunnel models and research facilities, and the measurement techniques applied. In addition, the effect of AFC on the flow will be contrasted to the underlying physical mechanisms of conventional multi-element high-lift systems with a focus on the effect of a slat.

Actuation concept

For the results presented in this dissertation, the employed concept of actuation bases on the induction of vortical structures by means of pulsed air jet blowing from rectangular slots with an inclination angle of approximately 30° relative to the local model surface. The concept aims at enhancing the mixing rate of low- and high-momentum fluid across the near wall flow field. The mediate effect is an increased ability of the flow to withstand stronger adverse pressure gradients without separating from the aerodynamic body.

The pulsed air jets required for that concept were generated using fluidic actuators. A single element of such a fluidic actuator is shown in fig. 3.1. Those devices require a pneumatic driving signal to induce periodic operation, which was supplied either by mechanical valves or by fluidic oscillators. The valve driven actuator system allows to test a broader parameter range, as actuation frequency is completely decoupled from actuation amplitude. The oscillator driven system, constituting a two-stage fluidic actuator concept without any moving or electrical

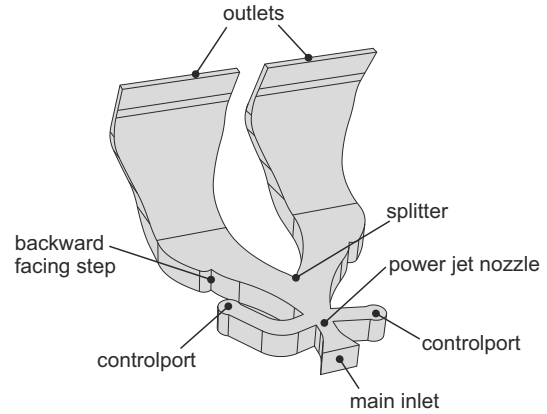


Figure 3.1: Sketch and nomenclature of a single element fluidic diverter as employed throughout the work reported

components, is considered a more industry-near design as it is more robust. Both systems are portrayed in fig. 3.2.

Fluidic actuators were selected for the work reported here, because they offer advantages over alternative actuator concepts (see sec. 1.3). The most important one is their ability to provide high actuation amplitudes with respect to both, peak jet velocity and allowable mass flow rates, while allowing for a compact

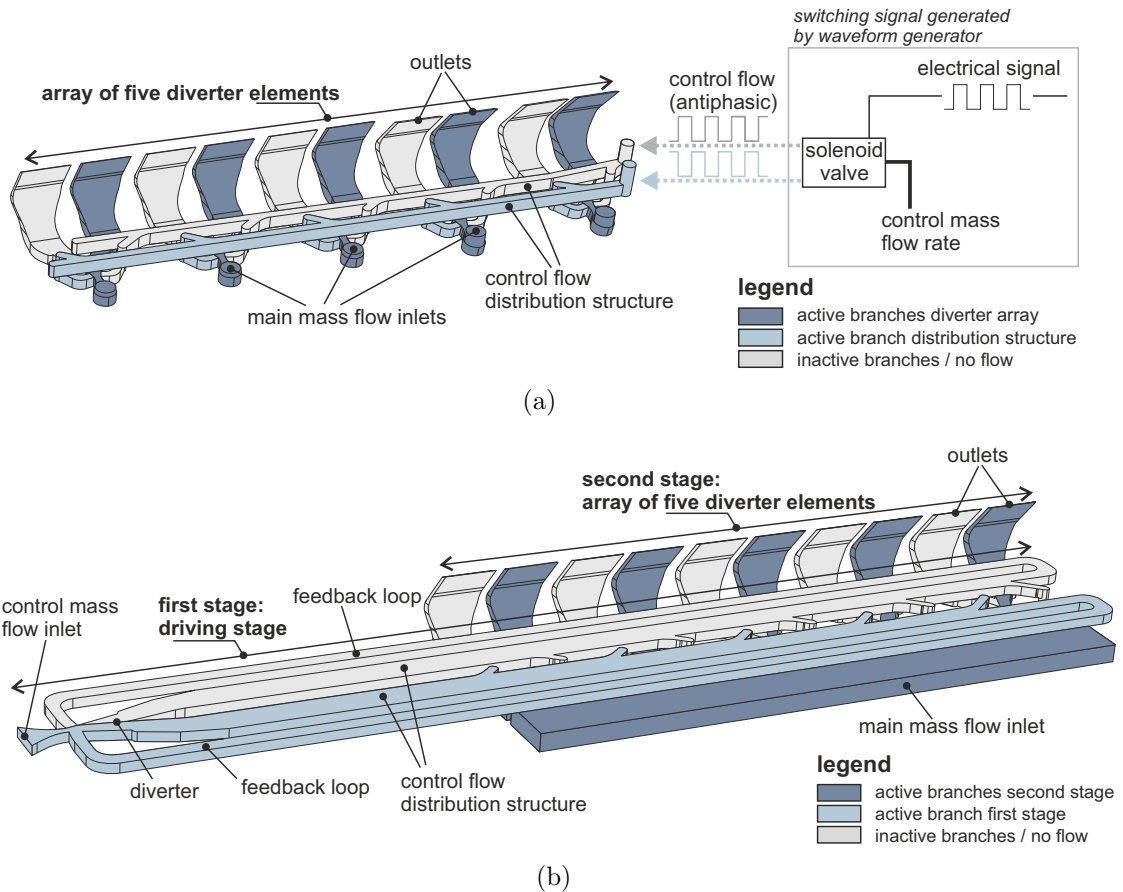


Figure 3.2: Comparison of the two AFC system layouts: a) valve driven; b) oscillator driven

design. This is especially relevant in the context of leading edge flow control, as the distance from the location of actuation to the element's trailing edge is usually much larger than for actuation on e.g. the trailing edge flap, therefore requiring higher control authority. In addition, fluidic actuators can be scaled easily, which favored their transfer between the different models employed.

Prior to entering into the individual wind tunnel test campaigns, the respective actuator system was qualified in bench-top experiments in still air. Those tests served to verify the spanwise homogeneity of actuation amplitude (i.e. that the peak jet velocity of individual actuator deviates less than 5% from the averaged peak jet velocity across the span) and that the modulation Mod of the air jets (as defined in eqn. 3.1) satisfies $Mod > 95\%$.

$$Mod = \frac{u_{jet,max} - u_{jet,min}}{u_{jet,max}} \quad (3.1)$$

Where $u_{jet,max}$ and $u_{jet,min}$ being the maximum and minimum values of the measured jet velocity at the outlets.

In addition, those experiments served to establish the fluid density of the air jets at the outlets, required for calculating, e.g., the momentum coefficients c_μ quoted in [Bauer2014b,Bauer2015a].

Wind tunnel models and instrumentation

The experiments were conducted on three different wind tunnel models. Those are a generic 2D two-element model (**F15**) in [Bauer2014a], a complex 3D outer wing model (**OWM1**) in [Bauer2014b], and a similar outer wing model with increased fidelity (**OWM2**) in [Bauer2015a]. In all experiments, the flow control system was integrated at the leading edge of the respective model, in the region of re-compression just downstream of the suction peak. Fig. 3.3 depicts the 2D model and the high-fidelity outer wing model during the test campaign.

The results presented in [Bauer2014a] were obtained in experiments conducted on a wind tunnel model of the 2D DLR-F15 high-lift airfoil in a two-element

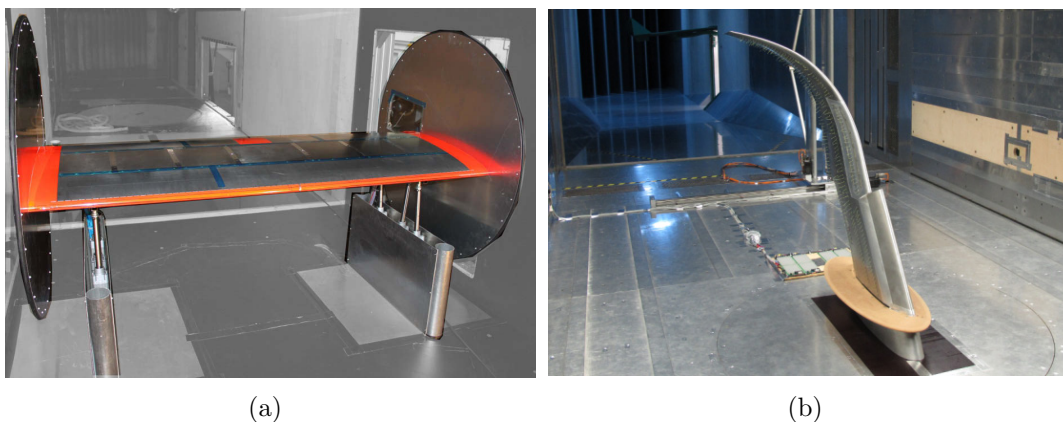


Figure 3.3: Wind tunnel models: a) F15 model; b) OWM2 model

set-up. This airfoil is a section of a three-element generic civil airliner wing. The slat was retracted into the main element. The flap was deployed to an AFC reference setting with a flap deflection angle of $\delta_f = 45^\circ$ (with gap = 15.9mm and overlap = 3.3mm). The chord of the model in clean configuration is $c_{ref} = 600\text{mm}$ and its span measures 1660mm. The airfoil was mounted between two circular endplates to prevent pressure equalization between the upper and lower surface. Testing was conducted at a chord REYNOLDS number of $Re_c \approx 1 \cdot 10^6$ and a MACH number of $Ma = 0.08$. Tripping was applied to ensure a turbulent state of the boundary layer. Therefore a $40\mu\text{m}$ high and 1mm wide tape was applied to the main element at $x/c=0\%$, $x/c=2\%$ on the pressure side surface, and $x/c=1\%$ on the suction side surface. The aerodynamic coefficients presented in this publication were calculated from integral force measurements obtained using a six-component strain gage balance. Additionally, static surface pressure was measured at the midspan of the model at 32 stations on the main element and at 16 stations on the flap. Detailed flow field information was gathered via stereoscopic time-resolved (TR) particle image velocimetry (PIV) measurements at midspan for individual angles of attack and actuation parameter combinations at the main element's leading and trailing edge.

The model under investigation for the results presented in [Bauer2014b] is much more complex. Its shape is highly three-dimensional, it is finite, tapered, and swept back at an angle of 35° . It consists of three distinct sections with different aerodynamic behavior. The inner section is equipped with a slat which is deployed to a take-off setting with a sealed slat gap. At this section's trailing edge the model's contour is kinked to mimic an aileron deflected to a fixed angle. The middle part of the model is not equipped with a slat and is prone to leading edge separation at high incidence angles. The flow control system is installed here. Adjacent to that a winglet forms the third section of the model. The span of this model measures 1040mm. Its reference chord length c_{ref} is 443mm. The experiments were conducted at a reference chord REYNOLDS number of $Re_c = 1.05 \cdot 10^6$ and a MACH number of $Ma \approx 0.13$. Tripping was applied at two locations using strips of tape ($40\mu\text{m}$ high, 1mm wide), attached at $x/c = 0.1\%$ and $x/c = 0.5\%$ on the pressure side surface of the model. Again, a six-component wind tunnel balance located beneath the wind tunnel floor was employed to measure global forces and moments acting on the model and the aerodynamic coefficients were calculated from that data. The model was equipped with 48 static pressure taps in two rows (at $y/b = 42\%$ and $y/b = 55\%$) oriented in streamwise direction. The inner row comprised 30 stations on the suction and pressure surface, the outer row comprised 18 stations on the suction side surface only. In addition, oil and tuft flow visualizations were considered to study the surface flow field.

The model researched in the remaining publication [Bauer2015b] is geometrically similar to the one reported in [Bauer2014b], but its fidelity is further increased. Main differences are the more realistic wing shape, the integration of an actual aileron, and the addition of a splitter plate and a peniche to reduce wind tunnel boundary layer effects on the results. This model measures approximately 1400 mm from wind tunnel floor to wing tip. The peniche (164 mm in height) and the splitter plate reduce the effective span b of the model to 1250 mm. The

most relevant change with respect to previous experiments is the increase of the MACH number to a typical take-off MACH number of $Ma = 0.2$. The resulting Reynolds number based on the model's reference chord length c_{ref} of 490 mm is $Re_c \approx 2 \cdot 10^6$. No boundary layer tripping was deemed necessary for those experiments. The measurement techniques employed for this test campaign comprised integral forces and moments measurements using a six-component balance system, static pressure data acquisition at six chordwise and three spanwise sections totaling more than 150 pressure taps, and tufts flow visualization in combination with high-resolution cameras. In addition, the topology of the model wake was measured with a traversable five-hole probe rake positioned at a constant position in flow direction downstream of the swept model, which resulted in a locally variable downstream distance from the trailing edge between $0.5c_{ref}$ and $1.5c_{ref}$. The information above is summarized in table 3.1.

	model name		
	F15	OWM1	OWM2
used for	Bauer2014a	Bauer2014b	Bauer2015a
driver type	valve & oscillator	valve	oscillator
geometry	2D	3D	3D
A_{ref}	$0.99m^2$	$0.47m^2$	$0.58m^2$
c_{ref}	0.6m	0.44m	0.49m
span	1.66m	1.04m	1.25m
Ma	0.08	0.13	0.2
Re	$1.0 \cdot 10^6$	$1.05 \cdot 10^6$	$2.0 \cdot 10^6$
types of measurement	force, pressure, TR-PIV	force, pressure, surface flow visualization	force, pressure, surface flow visualization, wake flow

Table 3.1: Summary of experiment parameters and types of measurements

Test facilities

The experiments presented in the publications were conducted in two different test facilities: the GroWiKa wind tunnel facility at TU Berlin see fig. 3.4(a)¹ and the DNW-NWB wind tunnel facility at Brunswick see fig. 3.4(b)². Both facilities are closed circuit wind tunnels, but differ in size and operating range. Some specifications for the facilities are summarized in table 3.2. For the pre-studies

facility	GroWiKa	DNW-NWB
used for	Bauer2014a, Bauer2014b	Bauer2015a
test section	1.44m x 2m x 10m	3.25m x 2.8m x 8.0m
operating range	0m/s < V < 50m/s 0 < Ma < 0.15	0m/s < V < 90m/s 0 < Ma < 0.27

Table 3.2: Technical specifications of the wind tunnel facilities.

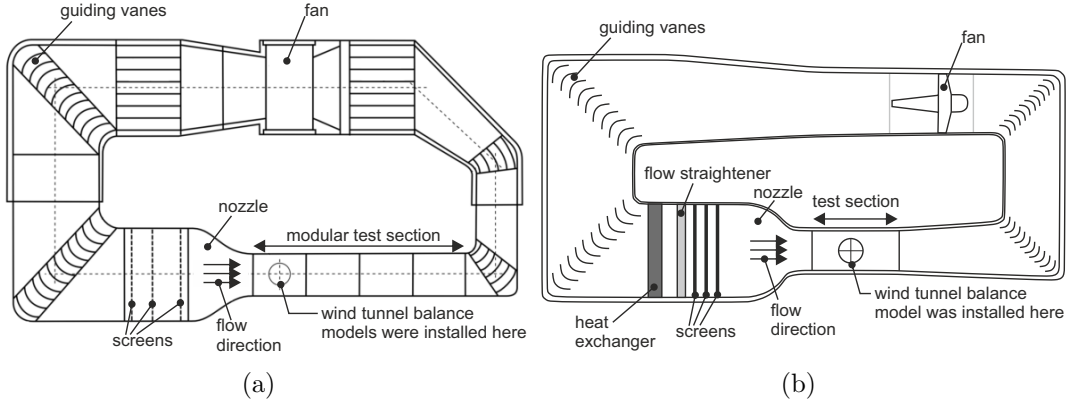


Figure 3.4: Wind tunnels: a) GroWiKa facility at TU Berlin; b) DNW-NWB facility at Braunschweig

conducted in the GroWiKa facility, the ratio of model reference area A_{ref} and test section cross section $A_{w/t}$ are $\frac{A_{ref,F15}}{A_{w/t,GroWiKa}} \approx 35\%$ for the 2D model reported in [Bauer2014a] and $\frac{A_{ref,OWM1}}{A_{w/t,GroWiKa}} \approx 17\%$ for the outer wing model reported in [Bauer2014b]. In comparison, the blockage in the final validation experiments of [Bauer2015a] conducted in the DNW-NWB facility is much smaller due to the larger wind tunnel cross section, resulting in a ratio of $\frac{A_{ref,OWM2}}{A_{w/t,DNW-NWB}} \approx 6\%$.

¹<http://fd.tu-berlin.de/en/facilities/wind-tunnels/growika/>

²<http://sata.tamu.edu/members/tunnels/DNW.html>

Effect of flow control

Closing this section on methodology an attempt is made to contrast the effect of conventional high-lift systems to the effect obtained by active flow control as employed across all publications presented here.

The physical principles on which multi-element high-lift systems rely are summarized by Smith [1], who identifies five different effects:

- *Slat Effect*
- *Circulation Effect*
- *Dumping Effect*
- *Off-the-Surface Pressure Recovery*
- *Fresh-Boundary-Layer Effect*

Each of those effects, individually and in interaction with each other, acts favorably on the surface pressure distribution on the wing to allow for higher circulation (and therefore higher lift) without the occurrence of separation. However, only the *slat effect* is discussed here as within this dissertation the removal of the slat and its replacement with AFC is undoubtedly the most significant change in the overall configuration.

Smith attributes the beneficial effect of the slat to the induction of a velocity field and its favorable superposition on the velocity field of the trailing element. In his analysis Smith simulates the slat effect by a point vortex located in front of

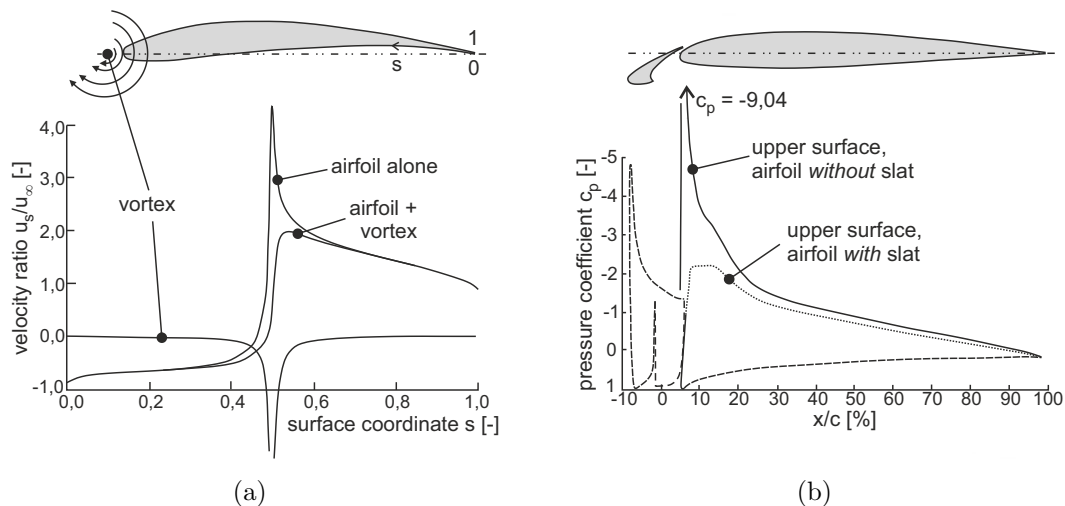


Figure 3.5: Slat effect according to [1]: a) Influence of a point vortex on the velocity field of a trailing element; b) Comparison of pressure coefficient distribution on the main element with and without a slat installed

the main element (see fig. 3.5(a)) and observes the resulting modification of the velocity field around it. He finds the vortex induced velocities running counter to those found in the nose region of the trailing element and concludes that the superposition of both velocity fields would therefore reduce the pressure peak in this region as illustrated in fig. 3.5(b). The influence of the vortex on the flow field decreases with increasing distance from its origin, therefore the flow around the trailing edge of the second element remains largely unaffected. The consequence of a reduced suction peak and an unchanged trailing edge pressure is that less re-compression must take place between those two locations, which leads to a flow less prone to separation. In summary, the slat effectively reduces the need for large positive pressure gradients $\frac{dp}{dx}$ in chordwise (x) direction to reach the trailing edge pressure. In contrast, flow control as applied here *enables* the flow to

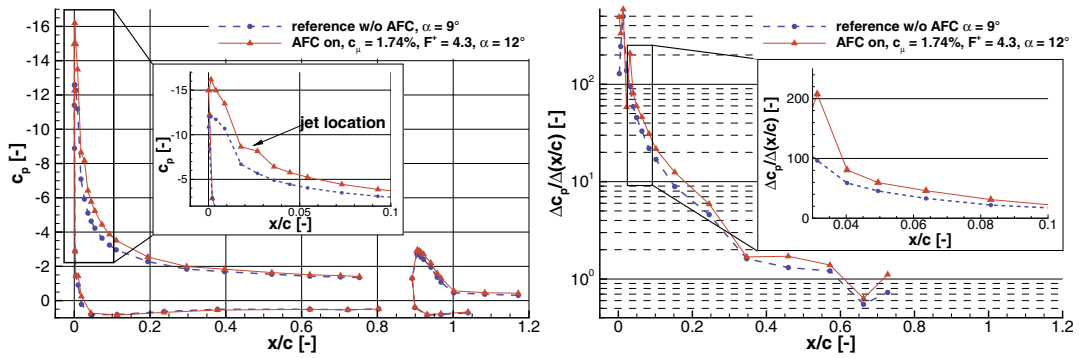


Figure 3.6: Comparison of pressure coefficient distributions (left) and re-compression rates for for the controlled and the uncontrolled flow just before stall angle (right).

remain attached *despite* large positive pressure gradients. This is best illustrated by results obtained on the 2D model reported in [Bauer2014a]. In fig. 3.6 the pressure coefficient distributions corresponding to the angles of attack just before separation occurs are shown for the controlled and uncontrolled flow respectively. In addition, the explicit re-compression rate is provided for those two cases on the right hand side of that figure. It is apparent from those results that the flow is capable of sustaining much higher adverse pressure gradients when forcing is applied. For both cases shown, the pressure coefficient at the most downstream station ($x/c \approx 0.75$) has a similar value of about $c_p \approx -1.4$, but the suction peak for the case of controlled flow is increased by almost 30% compared to the highest recorded baseflow value. Consequently, the re-compression rate, which is allowed for the controlled flow due to the application of forcing, more than doubles locally (from $\frac{\Delta c_p}{\Delta(x/c)} = 95$ to $\frac{\Delta c_p}{\Delta(x/c)} = 205$) for the cases shown here. This illustrates that although arriving at the same effect the underlying mechanism is completely different.

3.2 Summary of results

The results of all three individual papers prove the aerodynamic benefit of applying active flow control by means of periodic pulsed blowing to the leading edges of different wing models. This section summarizes major findings of the different contributions to further discuss them in the subsequent section.

The results of [Bauer2014a] showed that active flow control applied to a 2D two-element wind tunnel model using a staged fluidic actuator system delays the onset of stall by up to 4° . This maximum offset was obtained with a momentum coefficient of $c_\mu = 3.27\%$ and lead to an increase of maximum lift of $\Delta C_L \approx 0.26$ (approximately 10% increase compared to the uncontrolled flow). The correlation of lift increase and actuation intensity was found to be non-linear, with decreasing dC_L/dc_μ for increasing c_μ -values, but no saturation was observed within the range of momentum coefficients tested. Although it was shown that in agreement with literature (e.g. [22]) continuous blowing is less effective (and efficient) than pulsed blowing, the flow control effectiveness is largely independent of the specific time scale of the forcing. However, a marginal improvement of the actuation effectiveness was identified for forcing with an F^+ -value of approximately $F^+ \approx 2$. Using stereoscopic time-resolved PIV it was proven that the velocity field above the surface at the leading and trailing edges changes its characteristics completely when AFC is applied. Flow turning is increased significantly and high momentum fluid is redirected to the surface-near region. Frequency analysis of this data allows to conclude, that while the natural flow is dominated by large-scale vortical structures in the separated region, vorticity is contained to a flat layer close to the wing in the controlled case, with the dominant frequency present being that of the pulsed air jets. This pre-study proved the feasibility of the actuation system concept and the flow control approach.

Those results were then transferred to separation control experiments, reported in [Bauer2014b], which were conducted on a highly three-dimensional modern civil aircraft outer wing configuration. Here, the focus of research lay on drag reduction (i.e. the offset of drag increase to higher angles of attack) more than on maximum lift increase. Those experiments demonstrated the capability of pulsed jet actuation to enhance the aerodynamic efficiency by reduction of drag of the wing segment. The results showed that by choosing adequate parameters of control it is possible to offset performance degradation by up to 4 degrees. Here, saturation was observed with respect to actuation amplitude. Dependent on the distribution of actuation effort along the span, increasing the momentum coefficient beyond $c_\mu = 0.83\%$ (all three segments operated) or $c_\mu = 0.62\%$ (inner two segments operated) did not yield any additional benefit, even for doubling the actuation amplitude. For the limiting momentum coefficient of $c_\mu \approx 0.62\%$ drag on the wing segment was reduced by more than 40% and the aerodynamic efficiency was therefore increased by over 80%. Although the controlled flow cases exhibited higher maximum lift coefficients this increase was found to be secondary to drag reduction with respect to aerodynamic efficiency, as the ratio of C_D/C_L is dominated by the drag increase due to separation. For a given (sufficiently high) total momentum coefficient results indicated that the local dis-

tribution of momentum introduced, namely forcing concentrated on the inboard section of the model, is beneficial in terms of actuation efficiency.

Finally, the results reported in [Bauer2015a] delineate the successful synthesis of the two-stage actuator system approach of [Bauer2014a] and of the insights gained on controlling a complex flow detailed in [Bauer2014b] to their application to a high fidelity model. The aim was, again, to counter aerodynamic performance degradation of the model at high angles of attack. The experiments were conducted at the nominal take-off incidence MACH number of $Ma = 0.2$. It was shown that although all the forcing parameter variations tested improve the aerodynamic performance, the control effect is highly sensitive to the local distribution of momentum and mass introduction. The most effective set of forcing parameters found was actuation with the inner and the outer segment combined. For this combination, a momentum coefficient of $c_\mu = 0.59\%$, offsetted the stall angle by 2.4° , increased the maximum lift by 10.5% , and decreased the drag at $\alpha_{max,AFC}$ by 37% . The application of flow control changed the stall behavior of the model wing. While the baseflow separated gradually from the wing, with separation progressing from outboard to inboard with increasing incidence, stall occurred abruptly on the entire model under controlled flow. The actuation efficiency, measured in terms of the first aerodynamic figure of merit, improved significantly if the actuation effort was distributed advantageously along the span.

3.3 Discussion of results

The results presented in this dissertation illustrate the successful application of active flow control to the leading edge of different wind tunnel models using a newly developed fluidic actuator system. Throughout the individual publications the effectiveness of the control attempts was quantified in terms of offsetting stall to higher angles of attack, increasing the value of maximum lift, and reducing drag induced by the onset of separation. Common to all experiments is the observation that increasing the actuation amplitude, quantified in terms of momentum coefficient c_μ , is the dominant parameter determining the control effectiveness. Only in [Bauer2014b] saturation was observed with respect to this parameter, while in [Bauer2014a] and [Bauer2015a] increasing benefit was noted up to the maximum realizable momentum coefficient. In contrast, the exact value of the forcing frequency was found to be of only secondary importance throughout all three publications. As the results of [Bauer2014a] were obtained on a configuration that was also researched by Casper et al. [35] and Scholz et al. [43, 46], a comparison of the flow control effectiveness is attempted here (see fig. 3.7). In their contributions the authors report on experiments conducted at REYNOLDS numbers in the range of $2 \cdot 10^6 < Re < 9.2 \cdot 10^6$ and MACH numbers in the range of $0.14 < Ma < 0.19$. Those ranges do not overlap with the similarity parameters used for the experiments in [Bauer2014a], which were $Re = 1 \cdot 10^6$ and $Ma = 0.08$. Furthermore, the aspect ratios of the wing models differ between the experiments of Scholz and Casper ($b/c_{ref} \approx 4.6$) and the experiments reported in [Bauer2014a] ($b/c_{ref} \approx 2.8$). The most fundamental difference, however, is the location of actuation and the orientation and shape of the outlet structures.

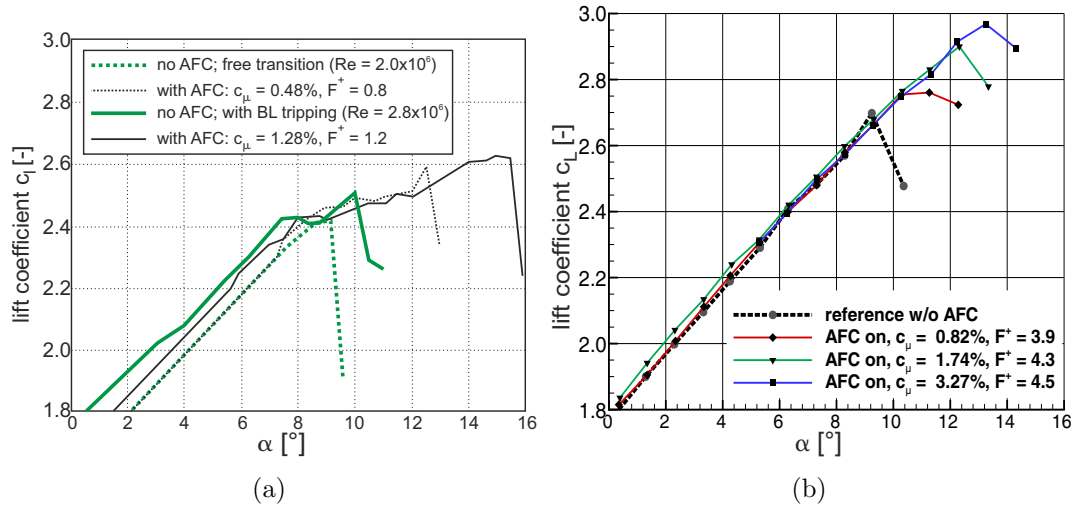


Figure 3.7: Comparison of lift gain on DRL-F15 wind tunnel model: a) data extracted from Scholz [46]; data from [Bauer2014a]

Although throughout all contributions pulsed blowing is the means of choice for controlling the flow, Scholz and Capser resort to pulsed blowing from circular holes on the pressure side surface of the model, while the flow control system in [Bauer2014a] is integrated on the suction side surface ejecting pulsed air jets from rectangular slots. To compare the results presented within the scope of this dissertation to the reported state of the art, the experiments with the nearest match of aerodynamic similarity parameters were chosen, which are experiment at $Re = 2.0..2.8 \cdot 10^6$ and $Ma = 0.15..0.19$ from Scholz [46], shown in fig. 3.7(a). As apparent from fig. 3.7, both concepts of actuation improve the aerodynamic performance of the model airfoil by increasing maximum lift and shifting stall to higher angle of attack. However, the underlying trends in the lift coefficient curves are remarkably different. The results from [Bauer2014a] show increasing maximum lift with increasing momentum coefficient while maintaining the original slope $dC_L/d\alpha$ of the curve up to the maximum angle of attack. Further increase in incidence results in complete stalling of the wing. In contrast, the lift coefficient curves from Scholz [46] (fig. 3.7(a)) shows a variable gradient $dC_L/d\alpha$ for the controlled cases, with the kink in the curve appearing at the respective maximum angle of attack of the uncontrolled baseflow. Besides the changing slope, the lift coefficient curves exhibit erratic behavior and possess several local maxima. It is for this reason that the gain in maximum lift is similar for both experiments although the increase in maximum angle of attack is higher in the experiments reported by Scholz. Extending the comparison of results beyond the specific example presented above to the experiments summarized in table 1.1 it becomes apparent that the results presented in [Bauer2014a] are in line with the findings of those researches, both with respect to momentum effort invested and aerodynamic benefit gained. The second major aspect of the work summarized in [Bauer2014a], which was then transferred into application in [Bauer2015a], is the establishment of a two-stage fluidic actuator system. In literature, only single

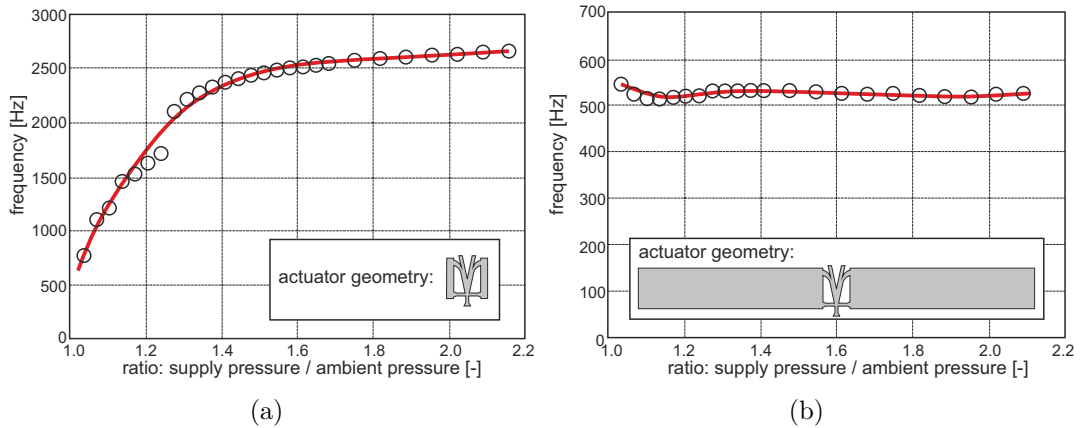


Figure 3.8: Correlation of switching frequency and actuator supply pressure proportional to the mass flow rate (experimental data extracted from Cerretelli et al. [77]): a) resistance dominated feedback structure; b) capacity dominated feedback structure

stage fluidic actuator systems (e.g. [77, 82], among many others) are reported. Those systems exhibit a direct dependency of the switching frequency on flow rate (which is proportional to the supply pressure) through the device (see fig. 3.8(a)), unless they are equipped with a feedback structure that is much larger than the switching body itself (see fig. 3.8(b)). For single stage systems the specific correlation of frequency and mass flow rate is determined by the fluid-mechanical resistance and capacity of the feedback structure, which is in turn a function of the feedback structure's geometry. In cases where the feedback mechanism is resistance dominated, the switching frequency increases with increasing mass flow rate. In contrast, devices in which the feedback mechanism is capacity driven, the switching frequency is almost constant over a wide range of flow rates. However, the later concept requires the feedback structure to be very large, which often conflicts with geometric (model size) constraints when considering those devices as flow control actuators. Therefore single stage fluidic actuators rely on a resistance driven feedback mechanism in most practical applications. In contrast, for an invariant geometric design, the two-stage actuator system reported in [Bauer2014a] and [Bauer2015a] does not operate on a fixed correlation curve of frequency and mass flow rate. Exemplary operating ranges of the two-stage actuator designs are presented in fig. 3.9. The additional degree of freedom that is added to the system is founded in the ability to control the mass flow rate through the driving (first) stage (i.e. feedback structure) independently of the mass flow rate through the second stage. This significant step beyond the current state of the art offers advantages from a practical perspective, especially when bearing industry applications in mind. As the (total) mass flow rate through the actuator system is a measure of actuation amplitude, changing this parameter without affecting the actuation frequency would allow to operate the system at the frequency that was identified as being optimal from a control effectiveness point of view over a wider range of momentum coefficients. Alterna-

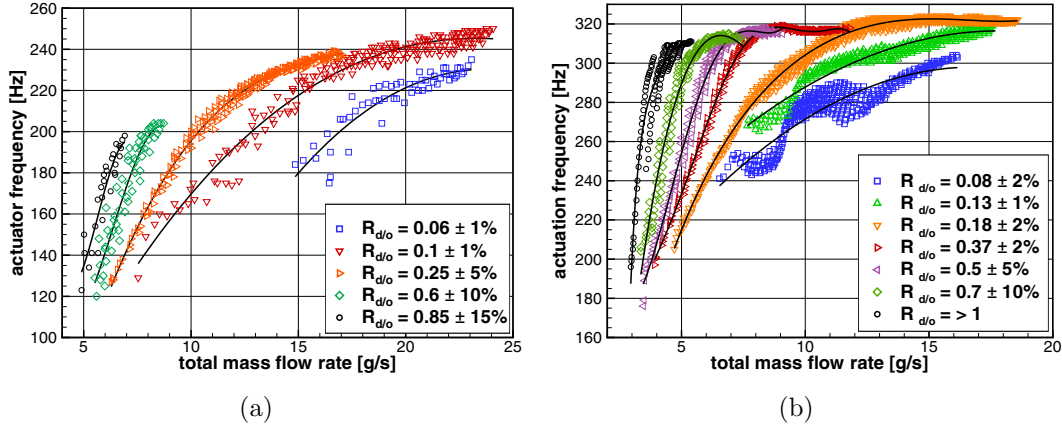


Figure 3.9: Correlation of switching frequency and mass flow rate for fixed geometry actuators. The total mass flow rate is the sum of the mass flow rates through the first (driving) and the second (outlet) stage. $R_{d/o}$ denotes the ratio thereof: a) data from [Bauer2014a]; b) data from [Bauer2015a]

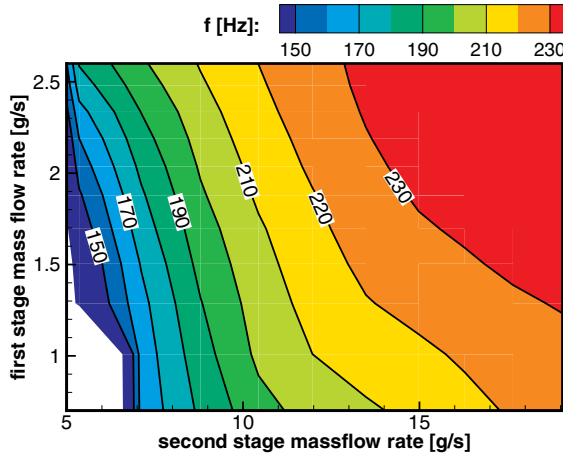


Figure 3.10: Influence of mass flow rates through first and second stage on switching frequency for the two-stage actuator system employed in [Bauer2014a].

tively, an application could benefit from providing variable frequency for a given actuation amplitude, either to adopt the AFC approach to varying flow conditions or to avoid actuation frequencies close to structural resonance frequencies of the airframe.

Analytical formulations for the switching frequency exist for self-oscillatory single stage actuator systems. Those approaches make use of electrical analogies to describe the feedback network either as L - R circuit [82] or as R - C - R circuit [77] (with L - impedance, R - resistance, and C - capacity). The resulting (lengthy) equations introduce empirical constants, but show good agreement between theory and experiment. No such description is available for the two-stage system, as the interaction between the first and the second stage introduces additional complexity beyond the scope of electrical analogy. In particular, the entrainment rate of the second stages' power jets, which is a function of the mass flow rate through this stage, directly influences the outflow condition of the first stage and

therefore dominates the switching behavior of the staged system. This observation is illustrated in fig. 3.10, which shows the frequency map of the two-stage actuator system employed in [Bauer2014a]. As apparent from those results, the mass flow rate through the second stage is dominant in terms of resulting actuation frequency.

In the analytical descriptions reverenced above, the switching frequency is described as a function of the feedback network only, neglecting the time necessary for the jet to detach from one side and to reattach to the other, because this switching time is assumed to be much smaller than the transport time of the network [77]. This is, however, true for small devices only. For fluidic actuators at the scale used for the experiments reported in [Bauer2014a,Bauer2015a] the switching time of the amplifier is of the same order of magnitude as the feedback network’s transport time, therefore forbidding negligence. For even larger scales, i.e. fluidic actuators sized for integration at aircraft level, the switching time of the jet is commonly the limiting factor with respect to maximum actuation frequency. To address this under-researched aspect of fluidic actuator design, an attempt to provide insight on the effect of scaling was attempted based on the actuator geometry of [Bauer2014a], which was taken as the smallest design. From this design, three additional actuator elements were scaled according to table 3.3 and manufactured.

#	A_{pj} [mm^2]	scale factor [-]
1	12.8	1
2	28.8	1.5
3	39.2	1.75
4	51.2	2

Table 3.3: Overview of power jet nozzle cross sections A_{pj} and scaling factors for the diverter elements tested

Each actuator was equipped with pressure sensors measuring the unsteady static pressure at the actuators’ control ports and the unsteady total pressure at each of the actuators’ outlets. The dynamic pressure of the power jet was calculated based on the total pressure in each actuator’s plenum and the static pressure recorded at the exit of the respective power jet nozzle (contraction ratio of 33:1 from plenum to power jet nozzle). In addition, the mass flow rates through power jet nozzle and control ports were measured. For each actuator sample several hundred points of operation, defined by one set of power jet mass flow rate and control mass flow rate, were tested and the quantities listed above were recorded. All unsteady pressure data was subsequently phase averaged to minimize statistical errors. The switching time t_s of the elements was defined (arbitrarily, but consistently across all scales) as the time necessary for the total pressure at one outlet to rise from 5% to 95% of its respective maximum value (see fig. 3.11(top) for illustration). Only points of operation for which the modulation (see equation 3.1) was larger than $Mod > 95\%$ were considered for this evalua-

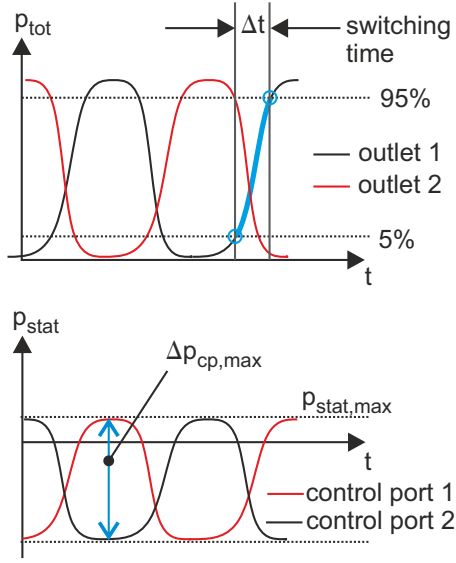


Figure 3.11: Definition of switching time t_s (top) and maximum differential pressure between the control ports $\Delta p_{cp,max}$ (bottom)

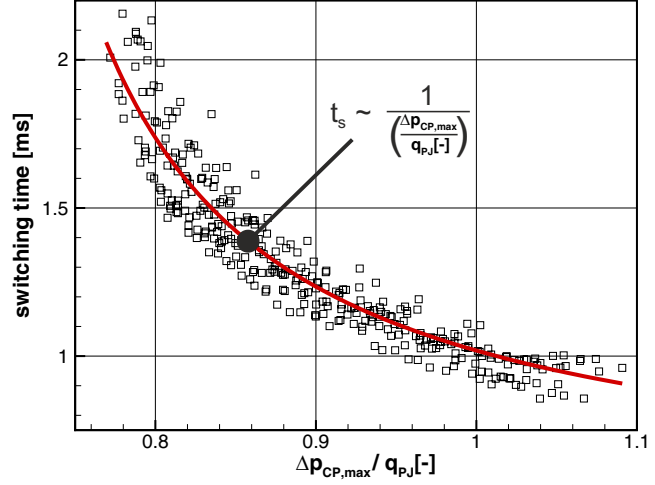
tion. Analysis of the data shows that the parameter combination best suited to collapse the calculated values for the switching time resulting from the various points of operation to one curve is the ratio of (maximum) differential pressure measured across the power jet $\Delta p_{cp,max}$ (see fig 3.11 for illustration) and the dynamic pressure of the power jet q_{pj} . This correlation is plotted in figure 3.12 for the reference scale actuator. The ratio $\frac{\Delta p_{cp,max}}{q_{pj}}$ can be interpreted as a measure of the ratio of the pressure force acting in traverse direction on the power jet, deflecting it to either side, and the dynamic head of the high velocity power jet. The quantity in the denominator q_{pj} is a function of power jet mass flow rate and given geometry only. In contrast, the quantity in the numerator $\Delta p_{cp,max}$ is not determined by one individual parameter of actuator operation, but is dependent on the interaction of power jet velocity and control mass flow rate for the given geometry. The lower pressure level is determined mainly by the evacuation of the control ports by entrainment of fluid from this region into the powerjet, the magnitude of which is proportional to the power jet velocity. The high pressure level is given by the amount of control flow provided to the active control port in excess of what is entrained by the power jet. Therefore, $\Delta p_{cp,max}$ is increased by both, increasing the control mass flow rate and increasing the power jet mass flow rate. As apparent from 3.12, the dependency of switching time and pressure ratio is non-linear, exhibiting shorter switching times for increasing pressure ratios. Consequently it is attempted to provide a functional description of the observed correlation. It was found, that the experimental data is fitted best using a correlation function of the generalized form given in eqn. 3.2.

$$t_s \sim \frac{1}{\Delta p_{cp,max}/q_{pj}} \quad (3.2)$$

Introduction of the (empirical) constants C_1 , C_2 , and C_{scale} leads to the specific formulation of the correlation function shown in eqn. 3.3.

$$t_s = \frac{C_1}{\frac{\Delta p_{cp,max}}{q_{pj}} + C_2} + C_{scale} \quad (3.3)$$

Figure 3.12: Experimental data on switching time of the reference size actuator element [Bauer2014a] dependent on the ratio of pressure difference across the power jet and dynamic pressure of the power jet



Using least mean square fitting of the scattered data recorded for each actuator scale independently the constants of eqn. 3.3 were identified. It was found that C_1 and C_2 are *independent* of actuator scale within the range of the actuator specimen tested. Solely S_{scale} is dependent of the actuator scale. The dependency of C_{scale} on the actuator's scaling factor sf is described by eqn. 3.4

$$C_{scale} \sim (sf)^2 \quad (3.4)$$

The introduction of two additional scale independent constants C_3 and C_4 allows to describe C_{scale} dependent only on the scaling factor relative to the reference size from [Bauer2014a] as

$$C_{scale} = C_3 \cdot (sf)^2 + C_4 \quad (3.5)$$

and provides a means to predict the jet switching time as a function of the pressure ratio $\Delta p_{cp,max}/q_{pj}$ and the scaling factor sf . The values and dimensions of the empirical constants C_1 through C_4 are given in table 3.4.

#	value	dimension
C_1	0.19	[s]
C_2	-0.65	[-]
C_3	0.26	[s]
C_4	0.19	[s]

Table 3.4: Values of empirical constants

Fig. 3.13 shows the correlation function applied to all actuator scales tested together with the original scattered data. From that figure it is evident that the empirical model fits the data very well over the provided range of scaling factors and pressure ratios. For a given pressure ratio the switching time of the actuators increase with increasing size. This implies that for an aircraft scale

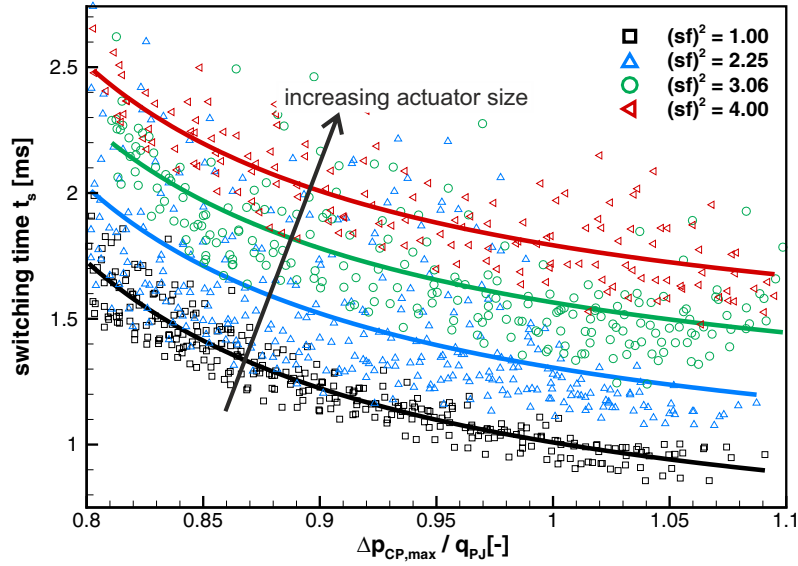


Figure 3.13: Switching time of the different sized actuator elements dependent on the ratio of pressure difference across the power jet and dynamic pressure of the power jet. The value of $(sf)^2$ is the square of the scaling factor relative to the reference size as indicated in the text.

actuator the switching time of the jet will in fact be the limiting time-scale with respect to maximum actuation frequency and cannot be neglected in the design process of such flow control systems. Therefore, these considerations based on the actuators used in [Bauer2014a] and [Bauer2015a] provide a step towards formulating scaling laws for the transfer of this actuator technology to industry application. Closing the discussion on the two-stage fluidic actuator an attempt is made to assess the advantages and disadvantages of this actuator system and to contrast it to the actuator concept described in sec. 1.3. To do so the overview table 3.5 is compiled rating all actuator types in categories relevant flow control applications based on personal experience and on information provided in the literature referenced in sec. 1.3. As apparent from the table there is no actuator that performs well in all categories. Therefore, a potential engineer will need to prioritize and weight the different aspects. For large scale and potential real scale applications actuation amplitude is of foremost importance as it determines the effectiveness of the control approach. Here, systems based on pneumatics and on combustion perform significantly better than their electrically operated counterparts. The main advantage of flow control systems that rely on electrical power is the ease of supplying them with the energy required. Routing electrical power through wires requires less installation space, produces lower losses, and introduces less system weight than the piping required for fluidic actuators and mechanical valves. Thus, electrical systems offer advantages with respect to overall infrastructure and actuator integration. Mechanical valves and combustion based actuators require two different types of supplies, which is pressurized air and electrical power and chemical fuel and electrical power respectively. While

3 Methodology and discussion of results

Category	Actuator	Synthetic Jet	Plasma	Mechanical Valve	Combustion	Fluidic (single-staged)	Fluidic (two-staged)
Amplitude range		-	--	+	++	++	++
Frequency range		--	o	o	o	+	+
Independence of amplitude and frequency		++	-	++	o	-	+
Parameter control and response time		+	+	+	-	-	o
Overall infrastructure		++	+	--	--	o	o
Actuator integration		+	+	-	-	+	+
Scaleability		-	--	-	o	++	++
Energy efficiency		-	-	o	+	+	++
Robustness		--	o	--	o	++	++

Table 3.5: Overview of Advantages and Disadvantages of different Flow Control Actuator Concepts. The rating ranges is: good performance ++ / + / o / - / -- bad performance

for mechanical valves this implies increased system weight and complexity only, the fuel supply required for combustion actuators, together with the detonation related heat development, might hinder their integration based on safety considerations. Actuator types that are controlled directly by an electrical signal, which are synthetic jets actuators, plasma actuators, and mechanical valves, are well suited for application that employ closed loop control, as their response time is sufficiently short. In contrast, fluidic actuators with the supply pressure as the only input parameter have a rather slow response time and the parameters such as duty cycle and phase relation between individual outlets cannot be controlled. However, the two-stage fluidic actuator performs better than its single-staged counterpart, as the frequency of actuation can be controlled independently from actuation amplitude as delineated above. Categories that are of specific relevance for real aircraft application are scalability, energy efficiency, and robustness. In those categories fluidic actuators are essentially without alternative, as only those can be scaled without downsides and their lack of moving parts and small structures makes them extremely robust. In terms of energy conversion efficiency, the two-stage fluidic actuator is superior to the single-stage design (as described in [Bauer2014a]), as the loss producing feedback structure is not required for each individual fluid amplifier element since one driving stage is shared by a multitude of second stage elements. In conclusion, the choice of optimal actuator system depends on the respective application. For (small scale) research applications synthetic jet actuators, plasma actuators, and mechanical valves acting as actuators are good choices as they allow excellent parameter control while their disadvantages with respect to amplitude and robustness are of lesser importance.

For real aircraft application, however, only fluidic actuators offer the amplitude and robustness required, with the two-stage approach providing some benefits over the single-staged design.

The transfer of active flow control technology to industry relevant levels, i.e. geometries and aerodynamic similarity parameters, is the fundamental contribution to the state of the art of the work performed in [Bauer2014b] and [Bauer2015a]. Although the model employed for the experiments reported in [Bauer2014b] is highly complex and resembles a civil aircraft relevant geometry, comparison with the results of [Bauer2015a] emphasizes the need to research the models at realistic flow conditions. Despite the similarity of the models employed, increasing the flow velocity from $Ma = 0.13$ in [Bauer2014b] to $Ma = 0.2$ in [Bauer2015a] changed the stall behavior significantly, which is also reflected in the difference in actuation effectiveness. While for the lower flow velocity separation progressed successively from outboard to inboard, stall was triggered by the upward flow motion induced by the slat edge vortex for the case of high incidence velocity. In both cases local intensification of actuation along the span proved to be beneficial in terms of actuation efficiency. However, for similar momentum coefficients of $c_\mu \approx 0.6\%$ and jet velocity ratios of $VR \approx 4$, stall was offset by 4° at $Ma = 0.13$ [Bauer2014b], while this offset was (lower, but still significant) 2.4° at $Ma = 0.2$ [Bauer2015a] due to the onset of separation in the region trailing the slat edge. With respect to those results a relevant point of reference from the current state of the art is the publication of Lengens [92]. In his contribution the author reports on the assessment of local active flow control applied to the leading edge in the region of the slat cutback above the pylon from an multidisciplinary industry point of view. Similar to the experiments reported in [Bauer2015a] the flow field to be controlled is dominated by strong longitudinal vortices. In addition, model

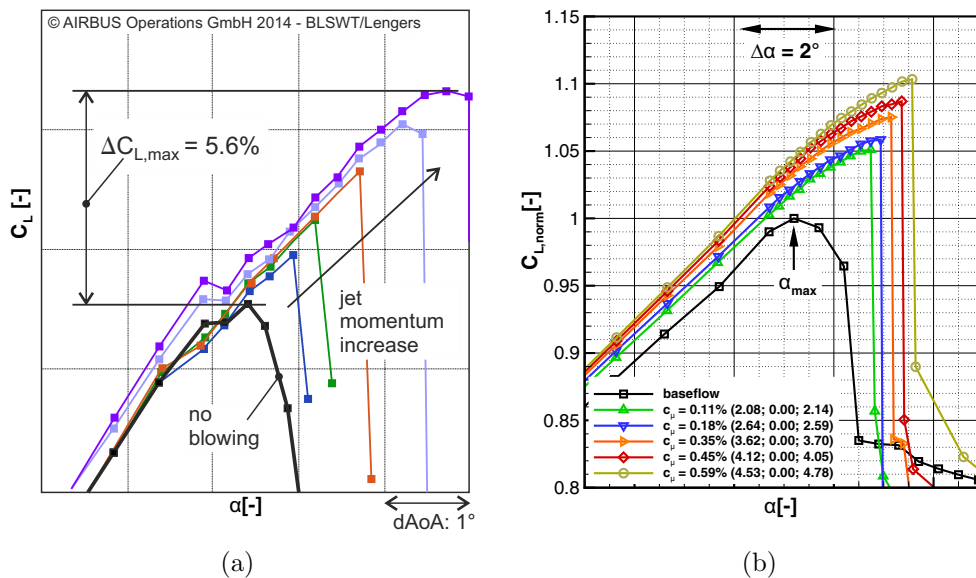


Figure 3.14: Comparison of maximum lift increase for varying momentum coefficients: a) data from Lengens [92]; b) data from [Bauer2015a]

complexity, REYNOLDS, and MACH number are in good accordance. Besides aerodynamic results Lengens considers aspects of system and structure integration, handling quality, energy provision, and noise. The author concludes that based on an overall aircraft design approach, integration of active flow control at the proposed location seems realistic from an aircraft manufacturer's point of view. Exemplary results of Lengens and [Bauer2015a], illustrating the effect of varying momentum coefficient on maximum lift, are compared in fig. 3.14. The underlying trends of the lift curves of both experiments agree very well, with increasing momentum coefficients resulting in increased maximum lift. Lengens reports an offset in stall angle by up to 2.3° , while the maximum offset observed in the experiments of [Bauer2015a] is 2.4° . The similarity in flow control effectiveness, model complexity, and aerodynamic similarity parameters allows to conclude, that the finding of Lengens concerning overall aircraft aspects also relate to the AFC approach reported in [Bauer2015a].

In conclusion, the work presented in this dissertation contributes to two relevant streams of research, namely flow control actuator development and application of flow control for separation control. It goes beyond the current state of the art by presenting a novel two-stage fluidic actuator design, which overcomes several limitations of concurrent flow control actuators and introduces a new degree of freedom with respect to control parameters, while retaining its robustness. The experiments on a relevant geometry at nominal take-off MACH number reported in this dissertation advance active flow control technology to increase the aerodynamic efficiency of an aircraft during take-off. Therefore, overall results provide a promising prospect of the application of this technology in civil aviation industry in the foreseeable future.

List of Figures

1.1	Regions prone to separation due to the lack of a leading edge device on the suction side surface of a wing according to [2, 3].	2
1.2	Influence of momentum coefficient on lift coefficient and transition from boundary layer control to circulation control according to Jones et al. [24]	6
1.3	Schematics of a) Synthetic Jet Actuator [48], b) Plasma Actuator [48], c) Mechanical Valve, d) Pulsed Combustion Actuator [49], e) Sweeping Jet Actuator [50]	12
1.4	Jet between two parallel walls according to [85]: a) initial state; b) attached state	18
1.5	Flow topology inside a generic fluid amplifier element based on a sketch from [87]. (Asymmetric depiction to increase the readability)	19
1.6	Nomenclature of fluid amplifiers: fluidic oscillator (left) and bistable switch (right); devices are cut at their symmetry planes	20
3.1	Sketch and nomenclature of a single element fluidic diverter as employed throughout the work reported	60
3.2	Comparison of the two AFC system layouts: a) valve driven; b) oscillator driven	60
3.3	Wind tunnel models: a) F15 model; b) OWM2 model	61
3.4	Wind tunnels: a) GroWiKa facility at TU Berlin; b) DNW-NWB facility at Braunschweig	64
3.5	Slat effect according to [1]: a) Influence of a point vortex on the velocity field of a trailing element; b) Comparison of pressure coefficient distribution on the main element with and without a slat installed	65
3.6	Comparison of pressure coefficient distributions (left) and re-compression rates for the controlled and the uncontrolled flow just before stall angle (right).	66

3.7	Comparison of lift gain on DRL-F15 wind tunnel model: a) data extracted from Scholz [46]; data from [Bauer2014a]	69
3.8	Correlation of switching frequency and actuator supply pressure proportional to the mass flow rate (experimental data extracted from Cerretelli et al. [77]): a) resistance dominated feedback structure; b) capacity dominated feedback structure	70
3.9	Correlation of switching frequency and mass flow rate for fixed geometry actuators. The total mass flow rate is the sum of the mass flow rates through the first (<u>d</u> riving) and the second (<u>o</u> utlet) stage. $R_{d/o}$ denotes the ratio thereof: a) data from [Bauer2014a]; b) data from [Bauer2015a]	71
3.10	Influence of mass flow rates through first and second stage on switching frequency for the two-stage actuator system employed in [Bauer2014a].	71
3.11	Definition of switching time t_s (top) and maximum differential pressure between the control ports $\Delta c_{cp,max}$ (bottom)	73
3.12	Experimental data on switching time of the reference size actuator element [Bauer2014a] dependent on the ratio of pressure difference across the power jet and dynamic pressure of the power jet	74
3.13	Switching time of the different sized actuator elements dependent on the ratio of pressure difference across the power jet and dynamic pressure of the power jet. The value of $(sf)^2$ is the square of the scaling factor relative to the reference size as indicated in the text.	75
3.14	Comparison of maximum lift increase for varying momentum coefficients: a) data from Lengers [92]; b) data from [Bauer2015a]	77

List of Tables

1.1	Overview of experimental results on active flow control applied to the leading edge. Abbreviations: ZNMF - zero net mass flux; PB - pulsed blowing; CB - continuous blowing; SS - suction side; PS - pressure side; DC - duty cycle; location - location of actuation; angle - geometric jet exit angle; width - slot width in chord-wise direction or hole diameter; subscript 'base' refers to the uncontrolled baseflow	10
3.1	Summary of experiment parameters and types of measurements	63
3.2	Technical specifications of the wind tunnel facilities.	64
3.3	Overview of power jet nozzle cross sections A_{pj} and scaling factors for the diverter elements tested	72
3.4	Values of empirical constants	74
3.5	Overview of Advantages and Disadvantages of different Flow Control Actuator Concepts. The rating ranges is: good performance ++ / + / o / - / - - bad performance	76

Bibliography

- [1] Smith, A. M. O., “High-Lift Aerodynamics,” *Journal of Aircraft*, Vol. 12, No. 6, June 1975, pp. 501–530.
- [2] Haines, A., “Scale Effects on Aircraft and Weapon Aerodynamics,” Tech. Rep. AGARDOgraph 323, AGARD, 1994.
- [3] Ciobaca, V. and Wild, J., “Active Flow Control for an Outer Wing Model of a Take-off Transport Aircraft Configuration - A Numerical Study,” *32nd AIAA Applied Aerodynamics Conference, Atlanta, Georgia*, No. AIAA 2014-2403, 2014.
- [4] Prandtl, L. and Durand, W., *The Mechanics of Viscous Fluids*, Vol. 3 of *Aerodynamic Theory*, Springer Verlag, Berlin, 1924.
- [5] Stratford, B. S., “The prediction of separation of the turbulent boundary layer,” *Journal of Fluid Mechanics*, Vol. 5, 1959, pp. 1–16.
- [6] Seifert, A., Greenblatt, D., and Wygnanski, I., “Active separation control: an overview of Reynolds and Mach numbers effects,” *Aerospace Science and Technology*, Vol. 8, No. 7, 2004, pp. 569 – 582.
- [7] Prandtl, L., “Über Flüssigkeitsbewegung bei sehr kleiner Reibung,” *Proceedings of the Third International Congress, Heidelberg, Germany*, 1904, pp. 484–491.
- [8] Gad-el Hak, M., *Flow Control - Passive, Active, and Reactive Flow Management*, Cambridge University Press, 2000.
- [9] Schlichting, H. and Gersten, K., *Grenzschicht-Theorie*, chap. Grenzschichtbeeinflussung (Absaugen/Ausblasen), Springer, 9th ed., 2006, pp. 315–346.
- [10] Jones, G., Yao, C.-S., and Allan, B., “Experimental Investigation of a 2D Supercritical Circulation-Control Airfoil Using Particle Image Velocimetry,” *3rd AIAA Flow Control Conference, San Francisco, CA*, No. AIAA 2006-3009, 2006.
- [11] Kweder, J., Panther, C., and Smith, J., “Applications of circulation control, yesterday and today,” *International Journal of Engineering*, Vol. 4, No. 5, 2010, pp. 411.

- [12] Kweder, J., Zeune, C., Geiger, J., Lowery, A., and Smith, J., “Experimental Evaluation of an Internally Passively Pressurized Circulation Control Propeller,” *Journal of Aerodynamics*, Vol. 2014, 2014.
- [13] Sellers, W., Jones, G., and Moore, M., “Flow Control Research at NASA Langley in Support of High-Lift Augmentation,” *2002 Biennial International Powered Lift Conference and Exhibit, Williamsburg, Virginia*, No. AIAA 2002-6006, 2002.
- [14] Zander, V., *Aktive Beeinflussung von Sekundärströmungen an einer Verdichterkaskade mit Synthetik-Jet-Aktuatoren*, mensch und buch verlag, 2013.
- [15] Seifert, A., Bachar, T., Koss, D., Shepshelovich, M., and Wygnanski, I., “Oscillatory Blowing: A Tool to Delay Boundary-Layer Separation,” *AIAA Journal*, Vol. 31, No. 11, 1993, pp. 2052–2060.
- [16] Wygnanski, I., “Some New Observations Affecting the Control of Separation by Periodic Excitation,” *FLUIDS 2000 Conference and Exhibit, Denver, Colorado*, No. AIAA 2000-2314, 2000.
- [17] Hecklau, M., Wiederhold, O., Zander, V., King, R., Nitsche, W., Huppertz, A., and Swoboda, M., “Active Separation Control with Pulsed Jets in a Critically Loaded Compressor Cascade,” *AIAA Journal*, Vol. 49, No. 8, Aug. 2011, pp. 1729–1739.
- [18] Meunier, M. and Brunet, V., “High-Lift Devices Performance Enhancement Using Mechanical and Air-Jet Vortex Generators,” *Journal of Aircraft*, Vol. 45, No. 6, Nov. 2008, pp. 2049–2061.
- [19] Haucke, F. and Nitsche, W., “Active Flow Control on the Flap of a 2D High-Lift Wing Section at $Re=10^6$,” *29th AIAA Applied Aerodynamics Conference, Honolulu, Hawaii*, No. AIAA 2011-3359, 2011.
- [20] Haucke, F. and Nitsche, W., “Active Separation Control on a 2D High-Lift Wing Section Towards High Reynolds Number Application,” *31st AIAA Applied Aerodynamics Conference, San Diego, CA*, No. AIAA 2013-2514, 2013.
- [21] Nagib, H., Kiedaisch, J., Reinhard, P., and Demanett, B., “Control Techniques for Flows with Large Separated Regions: A New Look at Scaling Parameters,” *3rd AIAA Flow Control Conference, San Francisco, CA*, No. AIAA 2006-2857, 2006.
- [22] Greenblatt, D. and Wygnanski, I. J., “The control of flow separation by periodic excitation,” *Progress in Aerospace Sciences*, Vol. 36, No. 7, 2000, pp. 487 – 545.

-
- [23] Thomas, F., “Untersuchungen über die Erhöhung des Auftriebes von Tragflügeln mittels Grenzschichtbeeinflussung durch Ausblasen,” *Zeitschrift für Flugwissenschaften*, Vol. 10, No. 2, Februar 1962, pp. 46–65.
- [24] Jones, G. and Englar, R., “Advances in pneumatic-controlled high-lift systems through pulsed blowing,” *21st Applied Aerodynamics Conference, Orlando, Florida*, No. AIAA 2003-3411, 2003.
- [25] Poisson-Quinton, P. and Lepage, L., *Survey of French research on the control of boundary layer and circulation*, Vol. 1, New York: Pergamon Press, 1961, pp. 21–73.
- [26] Stalnov, O. and Seifert, A., “On Amplitude Scaling of Active Separation Control,” *Active Flow Control II*, edited by R. King, Vol. 108 of *Notes on Numerical Fluid Mechanics and Multidisciplinary Design*, Springer Berlin Heidelberg, 2010, pp. 63–80.
- [27] Bauer, M., Peltzer, I., Nitsche, W., and Gölling, B., “Active Flow Control on an Industry-Relevant Civil Aircraft Half Model,” *Active Flow Control II*, edited by R. King, Vol. 108 of *Notes on Numerical Fluid Mechanics and Multidisciplinary Design*, Springer Berlin Heidelberg, 2010, pp. 95–107.
- [28] Mueller-Vahl, H., Strangfeld, C., Nayeri, C., Paschereit, C., and Greenblatt, D., “Thick Airfoil Deep Dynamic Stall and its Control,” *51st AIAA Aerospace Science Meeting, Grapevine, Texas*, No. AIAA 2013-0854, 2013.
- [29] Zaman, K., Bar-Server, A., and Mangalam, S., “Effect of acoustic excitation on the flow over a low-Re airfoil,” *Journal of Fluid Mechanics*, Vol. 182, 1987, pp. 127 – 148.
- [30] Collins, F. G. and Zelenevitz, J., “Influence of sound upon separated flow over wings,” *AIAA Journal*, Vol. 13, No. 3, 1975, pp. 408–410.
- [31] Darabi, A. and Wygnanski, I., “Active management of naturally separated flow over a solid surface. Part 1. The forced reattachment process,” *Journal of Fluid Mechanics*, Vol. 510, 7 2004, pp. 105–129.
- [32] Nishri, B. and Wygnanski, I., “Effects of Periodic Excitation on Turbulent Flow Separation from a Flap,” *AIAA Journal*, Vol. 36, No. 4, April 1998, pp. 547–556.
- [33] Hecklau, M., Salazar, D., and Nitsche, W., “Influence of the Actuator Jet Angle on the Reattachment Process with Pulsed Excitation,” *New Results in Numerical and Experimental Fluid Mechanics VIII*, edited by A. Dillmann, G. Heller, H.-P. Kreplin, W. Nitsche, and I. Peltzer, Vol. 121 of *Notes on Numerical Fluid Mechanics and Multidisciplinary Design*, Springer Berlin Heidelberg, 2013, pp. 143–150.

- [34] Seifert, A. and Pack, L., “Oscillatory Excitation of Unsteady Compressible Flows over Airfoils at Flight Reynolds Numbers,” *37th AIAA Aerospace Sciences Meeting and Exhibit, Reno, NV*, No. AIAA 99-0925, 1999.
- [35] Casper, M., Scholz, P., Radespiel, R., Wild, J., and Ciobaca, V., “Separation Control on a High-Lift Airfoil using Vortex Generator Jets at High Reynolds numbers,” *41st AIAA Fluid Dynamics Conference and Exhibit, Honolulu, Hawaii*, No. AIAA 2011-3442, 2011.
- [36] Wild, J., “Mach-, Reynolds- and Sweep Effects on Active Flow Separation Control Effectivity on a 2-Element Airfoil Wing,” *Active Flow and Combustion Control 2014*, edited by R. King, Vol. 127 of *Notes on Numerical Fluid Mechanics and Multidisciplinary Design*, Springer International Publishing, 2015, pp. 87–100.
- [37] Naveh, T., Seifert, A., Tumin, A., and Wygnanski, I., “Sweep effect on parameters governing control of separation by periodic excitation,” *Journal of Aircraft*, Vol. 35, No. 3, 1998, pp. 510–512.
- [38] Seifert, A. and Pack, L., “Effects of sweep on active separation control at high Reynolds numbers,” *Journal of Aircraft*, Vol. 40, No. 1, 2003, pp. 120–126.
- [39] Chang, R., Hsiao, F.-B., and Shyu, R.-N., “Forcing level effects of internal acoustic excitation on the improvement of airfoil performance,” *Journal of Aircraft*, Vol. 29, No. 5, 1992, pp. 823–829.
- [40] Seifert, A., Darabi, A., and Wygnanski, I., “Delay of airfoil stall by periodic excitation,” *Journal of Aircraft*, Vol. 33, No. 4, 1996, pp. 691–698.
- [41] Brunet, V., Dandois, J., and Verbeke, C., “Recent Onera Flow Control Research on High-Lift Configurations,” *AerospaceLab Journal*, Vol. 6, No. AL06-05, June 2013.
- [42] Pack, L., Schaeffler, N., and Yao, C.S. and Seifert, A., “Active Control of Separation from the Slat Shoulder of a Supercritical Airfoil,” *1st Flow Control Conference, St. Louis, Missouri*, No. AIAA 2002-3156, 2002.
- [43] Scholz, P., Kaehler, C., Radespiel, R., Wild, J., and Wichmann, G., “Active Control of Leading-Edge Separation within the German Flow Control Network,” *47th AIAA Aerospace Sciences Meeting, Orlando, Florida*, No. AIAA 2009-0529, 2009.
- [44] Greenblatt, D. and Wygnanski, I., “Effect of leading-edge curvature on airfoil separation control,” *Journal of Aircraft*, Vol. 40, No. 3, 2003, pp. 473–481.
- [45] Khodadoust, A. and Washburn, A., “Active control of flow separation on a high-lift system with slotted flap at high Reynolds number,” *25th AIAA Applied Aerodynamics Conference, Miami, FL*, No. AIAA 2007-4424, 2007.

-
- [46] Scholz, P., *Aktive Kontrolle der Vorderkantenablösung von Hochauftriebsprofilen mit pneumatischen Wirbelgeneratoren*, Luft- und Raumfahrttechnik, Shaker Verlag, 2009, ISBN 978-3-8322-8316-2.
- [47] Narramore, J., “Retractable vortex generator,” Feb. 1 2011, US Patent 7,878,457.
- [48] Cattafesta, L. and Sheplack, M., “Actuators for Active Flow Control,” *Annu. Rev. Fluid Mech.*, Vol. 43, 2011, pp. 247–272.
- [49] Cutler, A., Beck, B., Wilkes, J., Drummond, J., Alderfer, D., and Danehy, P., “Development of a pulsed combustion actuator for high-speed flow control,” *43rd AIAA Aerospace Sciences Meeting and Exhibit, Reno, Nevada*, No. AIAA 2005-1084, 2005.
- [50] Woszidlo, R., Nawroth, H., Raghu, S., and Wygnanski, I., “Parametric Study of Sweeping Jet Actuators for Separation Control,” *5th AIAA Flow Control Conference, Chicago, Illinois*, No. AIAA 2010-4247, 2010.
- [51] Crowther, W. and Gomes, L., “An evaluation of the mass and power scaling of synthetic jet actuator flow control technology for civil transport aircraft applications,” *Proceedings of the Institution of Mechanical Engineers, Part I: Journal of Systems and Control Engineering*, Vol. 222, No. 5, 2008, pp. 357–372.
- [52] Kim, Y.-H. and Garry, K. P., “Optimization of a Rectangular Orifice Synthetic Jet Generator,” *3rd AIAA Flow Control Conference, San Francisco, California*, No. AIAA 2006-2862, 2006.
- [53] Gomes, L., Crowther, W., and Wood, N., “Towards a practical piezoceramic diaphragm based synthetic jet actuator for high subsonic applications - effect of chamber and orifice depth on actuator peak velocity,” *3rd AIAA Flow Control Conference, San Francisco, California*, No. AIAA 2006-2859, 2006.
- [54] Ternoy, F., Dandois, J., David, F., and Pruvost, M., “Overview of Onera Actuators for Active Flow Control,” *AerospaceLab Journal*, Vol. 6, No. AL06-03, June 2013.
- [55] Qayoum, A., Gupta, V., Panigrahi, P., and Muralidhar, K., “Influence of amplitude and frequency modulation on flow created by a synthetic jet actuator,” *Sensors and Actuators A: Physical*, Vol. 162, No. 1, 2010, pp. 36–50.
- [56] Glezer, A. and Amitay, M., “Synthetic Jets,” *Annual Review of Fluid Mechanics*, Vol. 34, No. 1, 2002, pp. 503–529.
- [57] Moreau, E., “Airflow control by non-thermal plasma actuators,” *Journal of Physics D: Applied Physics*, Vol. 40, No. 3, 2007, pp. 605.
- [58] Jolibois, J. and Moreau, E., “Enhancement of the electromechanical performances of a single dielectric barrier discharge actuator,” *IEEE Transactions on Dielectrics and Electrical Insulation*, Vol. 16, No. 3, 2009, pp. 758–767.

- [59] Forte, M., Jolibois, J., Pons, J., Moreau, E., Touchard, G., and Cazalens, M., "Optimization of a dielectric barrier discharge actuator by stationary and non-stationary measurements of the induced flow velocity: application to airflow control," *Experiments in Fluids*, Vol. 43, No. 6, 2007, pp. 917–928.
- [60] Zito, J., Arnold, D., Houba, T., Soni, J., Durscher, R., and Roy, S., "Microscale Dielectric Barrier Discharge Plasma Actuators: Performance Characterization and Numerical Comparison," *43rd AIAA Plasmadynamics and Lasers Conference, New Orleans, Louisiana*, No. AIAA 2012-3091, 2012.
- [61] Petz, R. and Nitsche, W., "Active Separation Control on the Flap of a Two-Dimensional Generic High-Lift Configuration," *Journal of Aircraft*, Vol. 44, No. 3, 2007, pp. 865–874.
- [62] McManus, K. and Magill, J., "Separation control in incompressible and compressible flows using pulsed jets," *27th AIAA Fluid Dynamics Conference, New Orleans, Louisiana*, No. AIAA 1996-1948, 1996.
- [63] Williams, D., Cornelius, D., and Rowley, C., "Supersonic cavity response to open-loop forcing," *Active Flow Control*, Springer, 2007, pp. 230–243.
- [64] Ibrahim, M., Kunimura, R., and Nakamura, Y., "Mixing enhancement of compressible jets by using unsteady microjets as actuators," *AIAA journal*, Vol. 40, No. 4, April 2002, pp. 681–688.
- [65] Choi, J., Annaswamy, A., Lou, H., and Alvi, F., "Active control of supersonic impingement tones using steady and pulsed microjets," *Experiments in fluids*, Vol. 41, No. 6, 2006, pp. 841–855.
- [66] Crittenden, T., Glezer, A., Funk, R., and Parekh, D., "Combustion-driven jet actuators for flow control," *31st AIAA Fluid Dynamics Conference and Exhibit, Anaheim, CA*, No. AIAA 2001-2768, 2001.
- [67] Cutler, A. and Drummond, J., "Toward a high-frequency pulsed-detonation actuator," *44th AIAA Aerospace Sciences Meeting and Exhibit, Reno, Nevada*, No. AIAA 2006-555, 2006.
- [68] Cutler, A., "High-frequency pulsed combustion actuator experiments," *AIAA Journal*, Vol. 49, No. 9, September 2011, pp. 1943–1950.
- [69] Horton, B., "Fluid-operated system," Feb. 25 1964, US Patent 3,122,165.
- [70] Culley, D., "Variable Frequency Diverter Actuation for Flow Control," *3rd AIAA Flow Control Conference, San Francisco, California*, No. AIAA 2006-3034, 2006.
- [71] Koklu, M., Melton, L., and Pack, G., "Sweeping Jet Actuator in a Quiescent Environment," *43rd Fluid Dynamics Conference, San Diego, California*, No. AIAA 2013-2477, 2013.

-
- [72] Gregory, J., Ruotolo, J., Byerley, A., and McLaughlin, T., "Switching behavior of a plasma-fluidic actuator," *45th AIAA Aerospace Sciences Meeting and Exhibit, Reno, Nevada*, No. AIAA 2007-785, 2007.
- [73] Gregory, J., Gnanamanickam, E., Sullivan, J., and Raghu, S., "Variable-Frequency Fluidic Oscillator Driven by a Piezoelectric Bender," *AIAA Journal*, Vol. 47, No. 11, Nov. 2009, pp. 2717–2725.
- [74] Tesar, V., Zhong, S., and Rasheed, F., "New Fluidic-Oscillator Concept for Flow-Separation Control," *AIAA Journal*, Vol. 51, No. 2, Nov. 2012, pp. 397–405.
- [75] Spyropoulos, C., "A sonic oscillator (Operational principles and characteristics of sonic oscillator- pneumatic clock pulse generator)," *Proceedings of the Fluid Amplification Symposium*, Vol. 3, May 1964, pp. 27–52.
- [76] Gaylord, W. and Carter, V., "Fluerics 27: Flueric Temperature-sensing Oscillator Design," DTIC Document HDL-TR-1428, Harry Diamond Laboratories, Washington D.C., April 1969.
- [77] Cerretelli, C. and Gharaibah, E., "An Experimental and Numerical Investigation on Fluidic Oscillators For Flow Control," *37th AIAA Fluid Dynamics Conference and Exhibit, Miami, Florida*, No. AIAA 2007-3854, 2007.
- [78] Graff, E., Seele, R., Lin, J., and Wygnanski, I., "Sweeping Jet Actuators - A New Design Tool for High Lift Generation," Tech. Rep. NF1676L-16485, NASA, 2013.
- [79] Seele, R., Graff, E., Gharib, M., Taubert, L., Lin, J., and Wygnanski, I., "Improving Rudder Effectiveness with Sweeping Jet Actuators," *6th AIAA Flow Control Conference, New Orleans, Louisiana*, No. AIAA 2012-3244, 2012.
- [80] Seele, R., Graff, E., Lin, J., and Wygnanski, I., "Performance Enhancement of a Vertical Tail Model with Sweeping Jet Actuators," *51st AIAA Aerospace Sciences Meeting, Grapevine, Texas*, No. AIAA 2013-0411, 2013.
- [81] Seele, R., Tewes, P., Wozidlo, R., McVeigh, M., Lucas, N., and Wygnanski, I., "Discrete Sweeping Jets as Tools for Improving the Performance of the V-22," *Journal of Aircraft*, Vol. 46, No. 6, Nov. 2009, pp. 2098–2106.
- [82] Arwatz, G., Fono, I., and Seifert, A., "Suction and Oscillatory Blowing Actuator Modeling and Validation," *AIAA Journal*, Vol. 46, No. 5, May 2008, pp. 1107–1117.
- [83] Whalen, E. A., Lacy, D. S., Lin, J. C., Andino, M. Y., Washburn, A. E., Graff, E. C., and Wygnanski, I. J., "Performance Enhancement of a Full-Scale Vertical Tail Model Equipped with Active Flow Control," *53rd AIAA Aerospace Sciences Meeting, Kissimmee, Florida*, No. AIAA 2015-0784, 2015.

- [84] Andino, M. Y., Lin, J. C., Washburn, A. E., Whalen, E. A., Graff, E. C., and Wygnanski, I. J., “Flow Separation Control on a Full-Scale Vertical Tail Model using Sweeping Jet Actuators,” *53rd AIAA Aerospace Sciences Meeting, Kissimmee, Florida*, No. AIAA 2015-0785, 2015.
- [85] Warren, R., *Fluid Amplifiers*, chap. 12: Bistable Fluid Amplifiers, McGraw-Hill Book Company, 1968, pp. 187–203.
- [86] Kirshner, J. and Katz, S., *Design Theory of Fluidic Components*, Academic Press, 1975.
- [87] Goto, M., *Fluid Amplifiers*, chap. 9: Attached Jets, McGraw-Hill Book Company, 1968, pp. 125–133.
- [88] Gregory, J. and Tomac, M. N., “A Review of Fluidic Oscillator Development,” *43rd AIAA Fluid Dynamics Conference, San Diego, CA*, No. AIAA 2013-2474, 2013.
- [89] Viets, H., “Flip-Flop Jet Nozzle,” *AIAA Journal*, Vol. 13, No. 10, Oct. 1975, pp. 1375–1379.
- [90] Rathay, N., Boucher, M., Amitay, M., and Whalen, E., “Performance Enhancement of a Vertical Stabilizer using Synthetic Jet Actuators: Non-zero Sideslip,” *6th AIAA Flow Control Conference, New Orleans, Louisiana*, No. AIAA 2012-2657, 2012.
- [91] Meyer, M., Machunze, W., and Bauer, M., “Towards the Industrial Application of Active Flow Control in Civil Aircraft - An Active Highlift Flap,” *32nd AIAA Applied Aerodynamics Conference, Atlanta, Georgia*, No. AIAA 2014-2401, 2014.
- [92] Lengers, M., “Industrial Assessment of Overall Aircraft Driven Local Active Flow Control,” *ICAS Proceedings: 29th Congress of the International Council of the Aeronautical Sciences, St. Petersburg, Russia*, No. Paper 1.1.1, 2014.